UNIVERSITY OF THE
WITWATERSRAND,
JOHANNESBURG

Accessory REE mineralization of the Nokeng fluorite deposit as distal facies of the adjacent Vergenoeg pipe, Bushveld Complex, South Africa.

By

Relebohile E. Makhema

1492253

Research Report: Submitted in partial fulfilment of the requirement for the degree of Master of Science in Economic Geology from the Faculty of Science at the University of the Witwatersrand.

Supervisor: Dr. Nonkuselo Madlakana

Co-Supervisor: Dr. Marina Yudovskaya

October 2024

Declaration

I declare that this report is my own, unaided work. I have read the University Policy on Plagiarism and hereby confirm that no plagiarism exists in this report. It has not been submitted before for any degree or examination at any other University. I willingly submit to any investigation by the School of Geosciences in this regard, and I undertake to abide by the decision of any such investigation.

Date: 1/10/2024 Signature: 

Acknowledgements

Firstly, I would like to thank my supervisor, Dr. N. Madlakana, for her unyielding dedication and contribution to this research report. This task proved to be a rather challenging, but your patience and positive demeanour was encouraging. To my co-supervisor, Dr. M. Yudovskaya, your vast knowledge on the Bushveld Igneous Complex was a key factor in the successful completion of this report. I would like to thank you for your honesty, grit and unconditional assistance throughout this project.

I would also like to extend my sincerest appreciation to the staff at the Earth Lab (University of the Witwatersrand) for timelessly analysing my samples.

- Dr. N. Madlakana for assisting with the TIMA analysis.
- Mr M. Patchappa for ICP-MS and XRF.
- Mr L. Mudalahothe for making the thin sections.
- Mr S. Tshabalala for helping with the thin sections.

To my mother, 'Mamokuena Makhema, it has always been you and I vs the world; thank you for your unchanging love and support.

Most importantly, glory be to God, the all mighty who strengthens me in everything I do.

Abstract

The Nokeng Plattekop deposit forms part of the Paleoproterozoic Bushveld Complex and it is located near Rust de Winter, approximately 80 km northeast of Pretoria. This deposit belongs to the Vergenoeg Igneous Complex, which is associated with a violent gas-vapour-rich rhyolitic eruption. The complex comprises the Vergenoeg discordant breccia pipe and a pyroclastic rock suite. Within the breccia pipe and associated pyroclastic rocks, rare earth element (REE) mineralization is observed in minerals like allanite, apatite, bastnasite, monazite, and xenotime. The Plattekop fluorite deposit, which lies 1000 m south of the breccia pipe, is postulated to represent spill-over remnants of the Vergenoeg volcanic edifice. This study performed a comprehensive petrographic and geochemical analysis of ore and pyroclastic breccia of the Nokeng Plattekop deposit, utilizing various analytical techniques, including optical microscopy, XRF, ICP-MS, and SEM. The aim is to characterise the style of accessory REE mineralization at Nokeng as a provisional distal facies of the Vergenoeg volcanic field.

The findings of this study suggest that the Nokeng Plattekop deposit comprises a hematite-fluorite unit overlying an ignimbrite unit. Hematite-fluorite ores of the upper unit resemble the Vergenoeg ore, exhibiting elevated CaO concentrations and reduced SiO_2 content attributed to high fluorite and hematite proportions. Conversely, the ignimbrite unit displays reduced CaO and elevated SiO_2 concentrations, corresponding to lower fluorite content and higher rhyolitic lava fragments. The basal ignimbrite is proposed to have formed during the early stages of rhyolitic volcanism, while Nokeng and Vergenoeg ores formed during later stages dominated by Ca- and F-rich ferruginous magma. Petrographic evidence suggests hematite pseudomorphs after magnetite, indicating mineral assemblage evolution.

REE mineralization in the Plattekop fluorite deposit is represented by bastnasite, monazite and xenotime, mostly associated with quartz, goethite, aegirine, hematite and fluorite. The highest REE + Y content (~ 5 890 ppm) is associated with Plattekop hematite-fluorite ores. Comparative analysis of REE distribution patterns suggests similar styles of mineralization between Vergenoeg and Nokeng, indicating both deposits as potential sources of REEs as by-product.

Table of Contents

List of Figures

List of Tables

Chapter 1: Introduction

1.1 Background

Rare earth elements (REEs) generally consist of 15 lanthanides together with chemically similar scandium (Sc) and yttrium (Y) (Yang et al., 2019; Connelly, 2005). REEs are commonly divided into two sub-groups, which include light rare earth elements (LREEs) such as La, Ce, Pr, Nd, Pm, Sm, Eu, and conventionally added Sc, as well as heavy rare earth elements (HREEs), which comprise Gd, Tb, Dy, Ho, Er, Tm, Yb, Lu, and additional Y (Yang et al., 2019). The LREEs possess atomic numbers ranging from 57 to 64, while the HREEs have atomic numbers ranging from 65 to 71 (Eterigho-Ikelegbe et al., 2021). These REEs are essential ingredients in a plethora of current and emerging critical technologies, comprising catalysts, fuel cells, optical fibres, lasers, high-strength alloys, speciality glass, high-strength magnets, optoelectronics, and others (Chakmouradian and Wall, 2012). Critical and innovative technologies, including cordless power tools and cell phones, would not exist without rare earth elements (Chakmouradian et al., 2012; Massari et al., 2013; Gholz, 2014).

Rare earth elements are considered as critical raw materials by the European Commission. According to the European Commission (2010), a critical raw material is a mineral/commodity that is economically valuable, but, vulnerable to supply disruptions. These REEs are highly valuable as they facilitate the global energy transition, with Nd, Pr, Dy, Tb, and Sm (Figure 1) being essential components in high strength magnets that are used in the wind energy and electric vehicle technology (Hatch, 2012). Other REEs such as La, Ce, Eu (Figure 31) are also in high demand. China accounts for more than 70 % of world-wide production of REEs and processes 90 % of the worlds REEs (Srinivasan et al, 2023). China has monopolized the global REE supply and, therefore, induced a worldwide dependency on the country, which constitutes a supply risk according to the EU document (2010). This criticality of REEs, and the high demand for the elements as energy transition commodities has resulted in a spike in their prices.

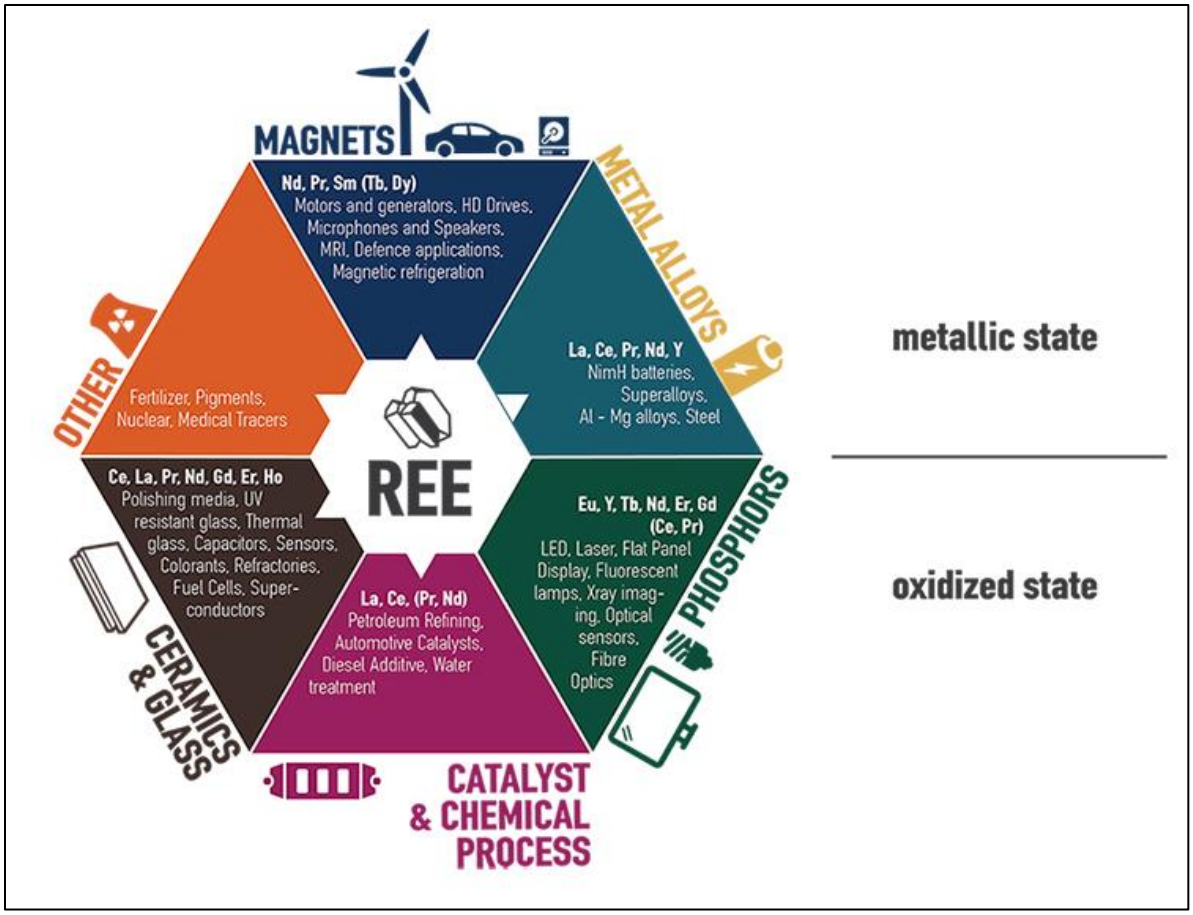

Figure 1. Diagram showing the uses of REEs in various industries, including ceramic and glass; magnets, catalyst and chemical processes; phosphors; and others (EURARE, 2022).

Among the rare earth elements, HREEs and Y are particularly scarce and highly valuable (Pingitore et al., 2018). The bulk of YHREEs are sourced from South China, hosted by ion absorption clays, while a smaller proportion of these elements occurs in four other rare earth element bearing minerals , including monazite, bastnasite, xenotime, and apatite ores (Pingitore et al., 2018). REE bearing minerals can be sourced from a number of deposit types including, but not limited to carbonatites, iron-oxide-copper-gold (IOCG), peralkaline/alkaline volcanism, skarns, unconformities, (Spandler et al., 2020) and silica saturated to oversaturated (rhyolites, granites and granitic pegmatites), placer heavy mineral sands and laterites (Weng et al., 2013). Ion absorption clays together with monazite, bastnasite, xenotime and apatite (Table 1) account for 95% of all global REE production (Gupta and Krishnamurthy, 2005; Mariano and Mariano Jr, 2012).

South Africa contributes less than 0.03 % towards global REE production, with leading countries being China (~70 %) and the United States of America (~14.33 %) (Statista, 2022). Despite the low global contribution, South Africa encompasses world-class REE deposits such as the Steenkampskraal Monazite Mine, which provides all 15 lanthanides (REEs), with resource estimates of around 605 000 tons at a grade of 14.4 % Total Rare Earth Oxides (TREO) (Steenkampskraal Holdings LTD, 2018). Mines such as Vergenoeg (fluorite mine) in the Bushveld Complex of South Africa have also been recorded to host REEs as accessory minerals, represented by carbonates (e.g., bastnasite and synchysite) and phosphates (e.g., xenotime and monazite). Previous studies (e.g., Crocker, 1985; Graupner et al., 2015) have suggested that the Nokeng Fluorite Mine may be distal facies of Vergenoeg due to similarities in geology and mineralization style. Consequently, areas surrounding Nokeng, including the Plattekop, Outwash Fan, and Wiltin deposits, may also hold potential for REE mineralization (Nokeng Fluorspar Mine, 2019).

Table 1: REE-bearing minerals recorded within the Vergenoeg suite and their compositions (Goff et al., 2004; Birtel et al., 2015; Graupner et al., 2015; Brandt et al., 2019; Mutele and Hunt, 2022; Crocker, 1985)

REE-bearing Minerals	**Composition**
Bastnasite	$(La,Ce,Y)CO_3F$
Synchysite	$Ca(Ce,La)(CO_3)_4$
Xenotime	YPO_4
Monazite	$Ce,La,Nd,Th)(PO_4SiO_4$
Allanite	$(Ce,Ca,Y)_2(Al,Fe^{2+},Fe^{3+})_3(SiO_4)_3(OH)$
Fluorite	(Ca,REE)F
Fluorapatite	$(Ca,Ce)_5(PO_4)_3F$

The increased demand, high prices and geopolitical factors associated with REEs could make it economic to extract them in the Plattekop and Vergenoeg deposits. Therefore, assessing REE concentrations and occurrences in fluorite ores of the Vergenoeg and Nokeng Plattekop

deposits could define a new ore type and help reduce reliance on China for REEs. While several researchers (Goff et al., 2004; Birtel et al., 2015; Graupner et al., 2015; Brandt et al., 2019; Mutele and Hunt, 2022) have discussed the occurrence of REEs within the Vergenoeg pipe, none have focused on the geology of Nokeng (Plattekop deposit) or potential REEs occurrences. This raises the questions about whether Nokeng is indeed distal facies of Vergenoeg and if both areas share similar REE mineralization.

1.2 Aims and objectives.

The overarching aim of this study is to establish whether the Nokeng fluorite deposit is distal facies of the Vergenoeg volcanic pipe. Investigations will be conducted to decipher whether Nokeng is endowed with accessory rare earth minerals, similarly to its proximal counterpart (Vergenoeg fluorite deposit).

Objectives

- Conduct a comparative analysis of the geological setting of Vergenoeg and that of Nokeng.
- Determine the REE abundances in bulk rocks of the Nokeng Fluorite Mine.
- Define the major REE minerals and their associations in fluorite ores and volcanic rocks.
- Estimate REE deportment and provisionally discuss economic viability of REE extraction at Vergenoeg and Nokeng.

1.3 Location

The Nokeng and Vergenoeg mine pits are located at coordinates 25°15'55.03"S, 28°34'48.58"E and 25°15'21.70"S, 28°34'54.76"E respectively, within the City of Tshwane Metropolitan Municipality, Gauteng, South Africa (Figure 2).

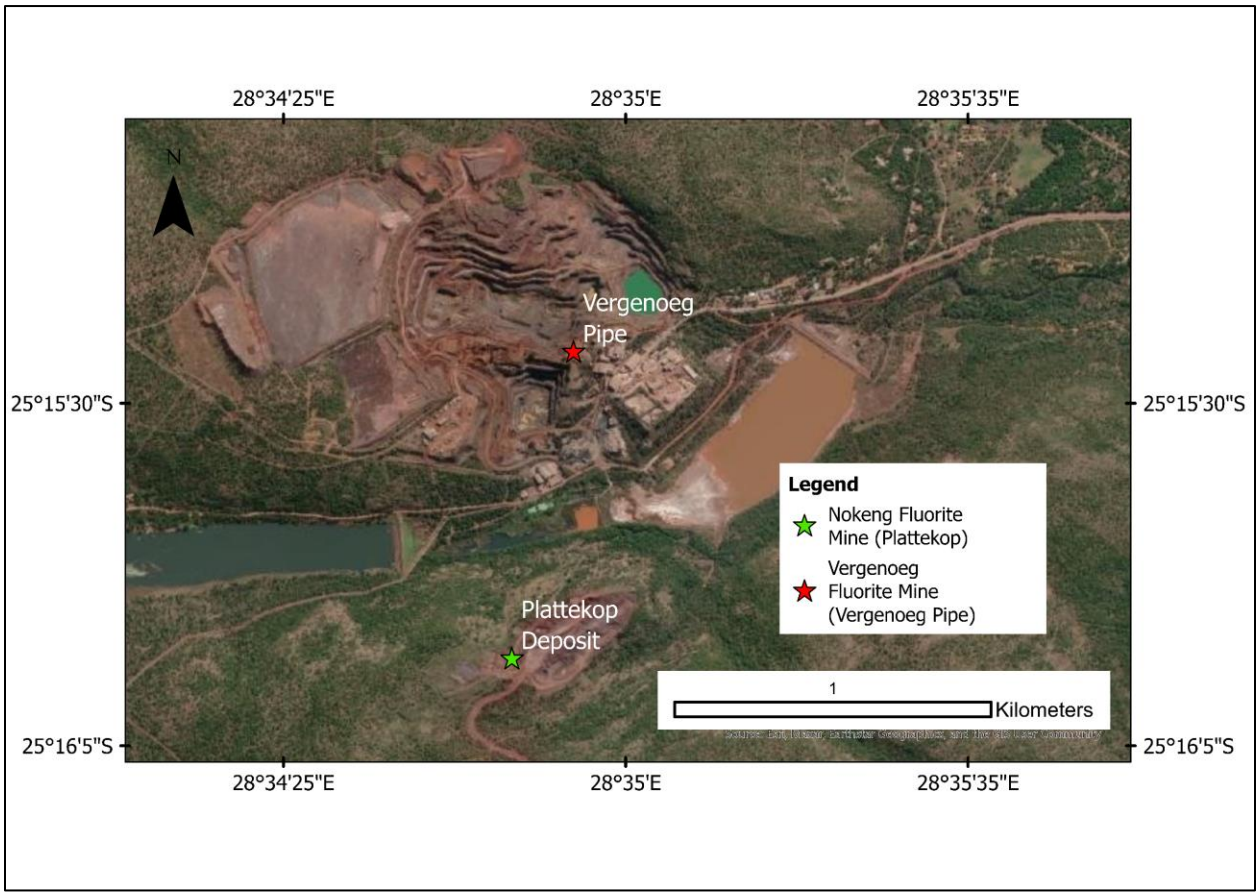

Figure 2. Map showing a google satellite image of Nokeng and Vergenoeg Mines, with the Plattekop and Vergenoeg open pits marked by a green and red star respectively. This Map was generated using ArcGIS Pro and utilizes WGS 1984 coordinate system.

Chapter 2: Geological Setting

2.1 Regional geology

2.1.1. Kaapvaal Craton

The Kaapvaal Craton of South Africa is an ancient and well-preserved fragment of the earth's crust, dating back to the Archean era (Bumby et al., 2012). It has an estimated area of 1 200 000 km^2 extending through parts of South Africa, Botswana, and Mozambique (Cheney, 1996). The Kaapvaal Craton is composed of 3.6 to 2.7 Ga greenstone and granite-gneiss terranes, which are capped/overlain by younger volcano-sedimentary rocks hosting intrusive suites of different ages (Zegers et al., 1998). The overlying Archean to Proterozoic volcano-sedimentary sequences include, from youngest to oldest, the Witwatersrand Supergroup, the Pongola Supergroup, the Ventersdorp Supergroup, and the Transvaal Supergroup (Ozturk, 2018). The craton is bordered by the Kheis Belt in the west, the Namaqua-Natal Belt in the east, and it is surrounded by the Limpopo and Mozambique belts in the north (De Wit et al., 1992).

2.1.2 Transvaal Supergroup

The 2 640 to 2 060 Ma (Zeh et al., 2020) Transvaal Supergroup is characterized by a ~15 000 m thick succession (Button, 1986) of partially metamorphosed sedimentary rocks deposited in the northern and western portions of the Kaapvaal Craton (Eriksson et al., 1995; Barton and Hallbauer, 1996; Frimmel and Minter, 2002). It overlies flood basalts of the 2.75 Ga Ventersdorp Supergroup (De Kock et al., 2012) and is overlain by volcanic rocks of the Rooiberg Group of the Bushveld Complex (Zeh et al., 2020). The Transvaal Supergroup sequences outcrop in two sedimentary basins in South Africa, namely the Griqualand West and Transvaal basins; it is also found in the Far-West Kanye basin in Botswana (Zeh et al. 2020). Sediments of the supergroup were deposited into a shallow epi-cratonic sea, which covered a major part of the Kaapvaal Craton (Els et al., 1995). The stratigraphic units of the Transvaal Supergroup in the NE of the Transvaal Basin include the Wolkberg, Chuniespoort and Pretoria groups (Figure 2).

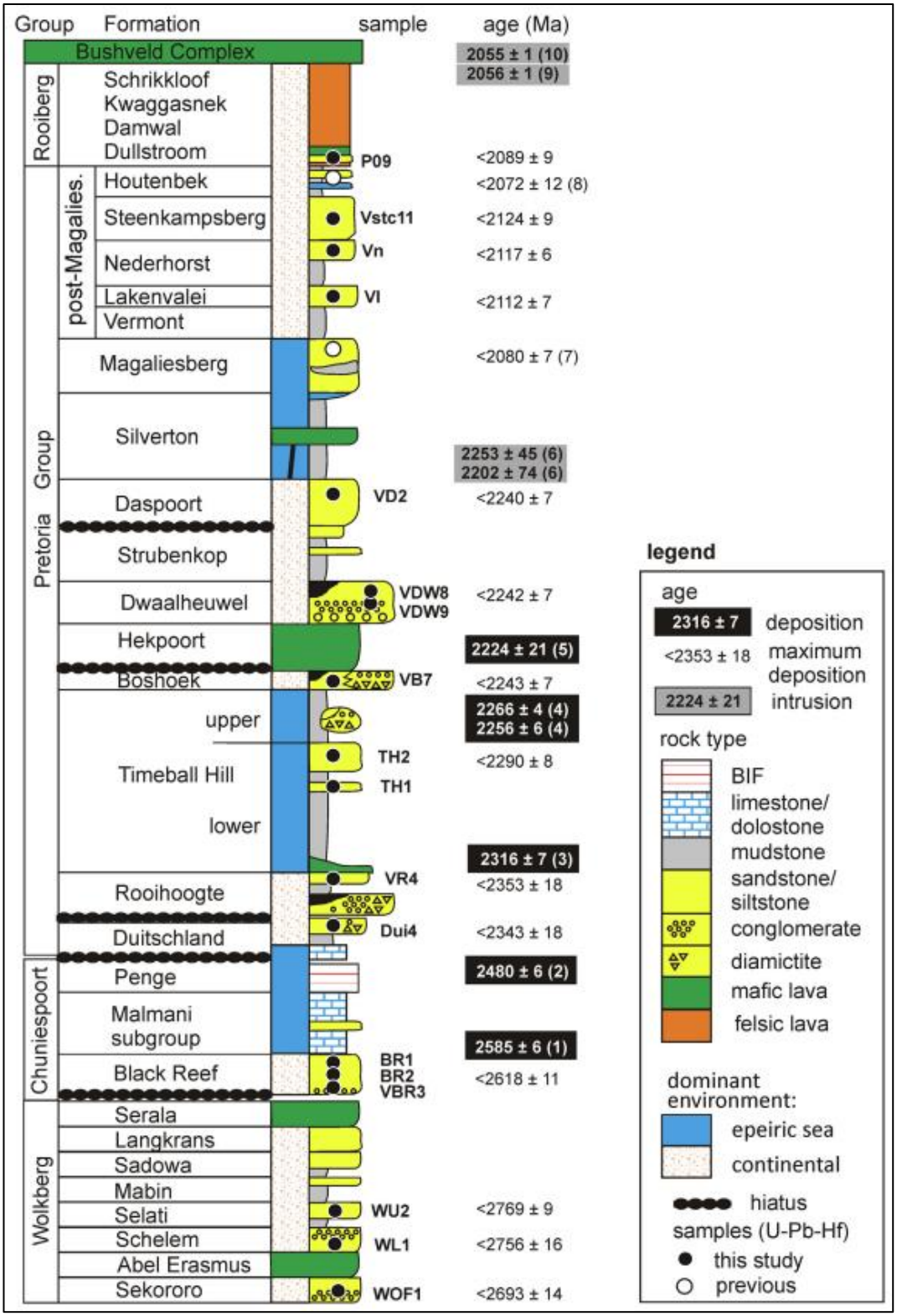

Figure 3. Stratigraphic column of the Transvaal Supergroup in the northeastern portion of the Transvaal Basin, showing all the groups and formations, with the Rooiberg and Bushveld Complex capping the succession (after Eriksson et al., 2006; Schroder et al., 2016).

2.1.3 The Bushveld Igneous Complex

The Paleoproterozoic Bushveld Igneous Complex (Figure 4) was emplaced into the Kaapvaal Craton around 2.06 billion years ago (Cawthorn, 2013; Scoates et al., 2021). It has an estimated area of c. 90 000 km^2 (Kinnaird et al., 2017) and intrudes the sedimentary and volcanic rocks of the Transvaal Supergroup as well as Archean granite-gneisses (Kinnaird et al., 2002). The Bushveld Complex comprises basaltic to felsic volcanic rocks of the Rooiberg Group dated at 2057±2.8 Ma (Harmer and Armstrong, 2000), the mafic/ultramafic Rustenburg Layered Suite, emplaced between 2055 and 2060 Ma (Scoates et al., 2021), the Rashoop Granophyre Suite, dated at 2061.8±5.5 Ma (Harmer and Armstrong, 2000), and lastly the Lebowa Granite Suite, with an age range from 2054±0.7 to 2056±0.9 Ma (Skursch et al., 2022).

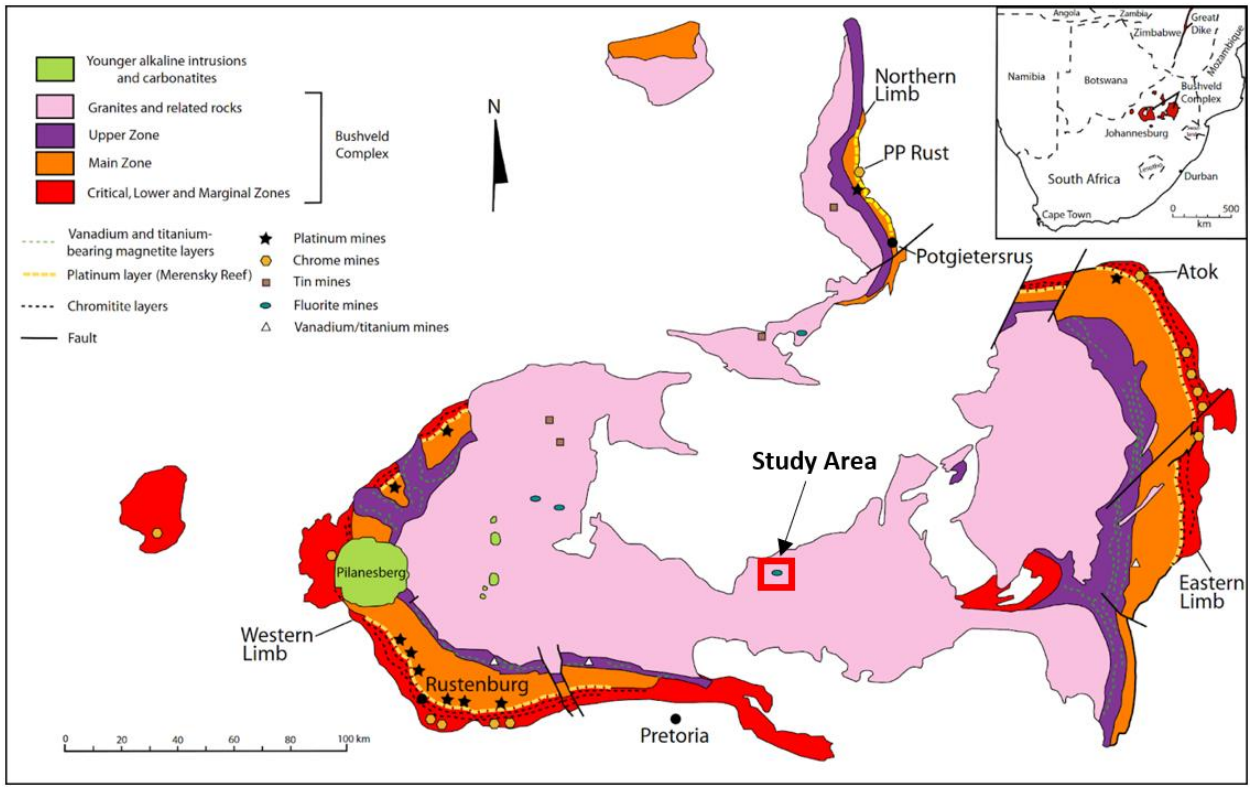

Figure 4. Geological map displaying the Bushveld Igneous Complex and the various limbs, lithologies, zones, characteristic mineral deposits, and the study area (after Viljoen and Schurmann, 1998 taken from Taylor et al., 2005).

2.1.4. Rooiberg Group

The Rooiberg Group is roughly 3 km thick and has an estimated area of 90 000 km^2; it is considered as one of the world's largest pyroclastic provinces (Yudovskaya et al., 2023). The Rooiberg Group's upper portion is dominated by rhyolites, which share a common mantle source with basal Rooiberg basalts and Bushveld mafic-ultramafic counterparts (Harmer and Sharpe, 1985; Buchanan et al., 2004). Despite having locally transitional relationships with underlying rocks of the Transvaal Supergroup sediments, it is petrogenetically associated with the Bushveld magmatic event (Buchanan et al., 2004; VanTongeren et al., 2010).

The Rooiberg Group comprises the basal Dullstroom basaltic as well as the Damwal, Kwaggesnek and Schrikkloof dacitic to rhyolitic formations (Figure 3) (Schweitzer, 1987; Schweitzer et al., 1995). The Dullstroom Formation is made up of thick basaltic and dacitic lavas with minor pyroclastic layers and intercalated sedimentary beds ((French and Twist, 1983; Harmer and Von Gruenewaldt, 1991). It can be divided into 6 types of lava, including: low-Ti basaltic andesite, basal rhyolite, high-Ti basalt, high-Mg felsites, high-Fe-Ti-P andesite and low felsites (Schweitzer et al., 1995; Jolayemi et al., 2020). In contrast, the Damwal Formation is not basaltic and comprises dacites and rhyolites interbedded with sandstones and quartzites (Schweitzer et al., 1995). The overlying Kwaggasnek Formation is dominated by rhyolites and minor shales, quartzites and agglomerates derived from low-Mg lava types (Schweitzer et al., 1995). Lastly, the upper Shrikkloof Formation is composed of low-Mg rhyolites with minor quartzite (Schweitzer et al., 1995).

Field observations and textures (porphyritic and glassy) allude to an explosive eruption and subsequent emplacement of the Schrikkloof Formation (Chiya, 2023). These textures along with geochemical data of the Schrikkloof Formation suggest that the Rooiberg Group was emplaced and deposited in a subaerial environment in an intra-cratonic setting (Chiya, 2023). The occurrence of tuffaceous material within the group is attributed to the violent volcanic eruptions (at temperatures > 1100) and rapid cooling on the surface (Chiya, 2023).

The vast bimodal volcanics of the Rooiberg Group were succeeded by the emplacement of the Rustenburg Layered Suite (RLS), which locally splits the Rooiberg volcanic sequence into an underlying basaltic floor and an overlying felsic roof (Harmer and Sharpe 1985; Lenhardt et al., 2012). The intrusions of the Rustenburg Layered Suite metamorphosed rocks of the Dullstroom to

Damwal formations (Yudovskaya et al., 2023), whereas emplacement of granites of the Lebowa Suite locally resulted in exogranitic hydrothermal mineralization of cassiterite, and the formation of tourmaline and carbonates, especially in the Rooiberg Group's northwestern portions (Buchanan, 2006).The Lebowa Granite Suite and its associated hydrothermal occurrences are dated at 1957 ± 15 Ma, and additional events occurred between 1790 ± 114 Ma and 1604 ± 70 Ma, which suggests that mineralization was periodic (Robb et al., 2000). Exogranitic ore deposits found within the Rooiberg group typically comprises polymetallic Sn-Fe-F-REE (Robb et al., 2000; Crocker et al., 2001). The mineralization styles are typically breccia pipes (e.g., Vergenoeg Fluorspar-Hematite pipe), stratabound to irregular veins (e.g., Union Tin Mine), and contact breccia porphyry (e.g., Zartkloof Fluorspar Mine). These mineralisation styles are predominantly confined to the Kwaggasnek and Schrikkloof Formations (Schweitzer et al., 1995b; Crocker et al., 2001).

2.2. Local geology of the Vergenoeg-Nokeng ore field

The Vergenoeg-Nokeng local geology is represented by an irregular vertical volcanic pipe, pyroclastics, and sedimentary rocks (Fourie, 2000). These rocks are known informally as the Vergenoeg Rock Suite, restricted to the farms Naauwpoort 208 JR and Kromdraai 207 JR (Crocker, 1985). This Vergenoeg Suite is encompassed within the Selons River Formation (Crocker, 1985), which was later renamed and subdivided into the Kwaggasnek and Schrikkloof formations of the Rooiberg Group (Groenewald and Groenewald, 2014). The suite is made up of five stratigraphic units, including a sedimentary unit; hematite fluorite and hematite unit; breccia agglomerate unit; ignimbrite unit; and lastly, the Vergenoeg volcanic pipe (Crocker,1985; Table 2).

2.2.1 The Sedimentary unit

The Vergenoeg sedimentary unit comprises stratiform ferruginous cherts (banded iron formations - BIF), associated conglomerates and Fe-poorer shales found in the farm Naauwpoort (Fourie, 2000). The unit is interpreted as a sedimentary outwash fan that formed through the erosion of pyroclastic rocks (Crocker, 1985). The alluvial unit represents the terminal phase of the Vergenoeg Suite, and it is capped by the banded iron formation (Crocker, 1985). This banded iron formation (BIF) formed in shallow water and is composed of chert and thin interbedded hematite, showing ripple marks, dewatering slump structures and minor crossbedding (Crocker, 1985). The unit also includes minor isolated pockets and layers of ferruginous sandstone and conglomerates, overlying portions of massive hematite bodies near and in the Vergenoeg pipe (Fourie, 2000).

Table 2: Illustration of all the stratigraphic units within the Vergenoeg Suite, their thickness, constituent rock types, structural and textural properties (modified after Crocker,1985).

Stratigraphic units	**Maximum thickness (metres)**	**Constituent rock type**	**Structural textural properties**	
Wilgerivier Formation		Sandstone and Conglomerate	Once covered the Vergenoeg suite	Waterberg Group
Sedimentary unit	10	Ferruginous conglomerates, grits, banded iron formation and chert.	Rounded hematite, felsitic and fluorite clasts in ferruginous matrix, cross bedding ripple marks and mud cracks in places	Vergenoeg Suite
Conformably stratified hematite fluorite and hematite units	20		Hematite and fluorite	
Breccia agglomerate unit	40	Predominantly felsic and rhyolitic pyroclasts in hematite matrix.	Fines enriched and fines depleted facies	
Ignimbrites	60	Predominantly felsic tuffs, ferruginous in places	White, black and multi coloured glassy tuffs	
Discordant volcanic pipe (Vergenoeg pipe)	Depper than 650 meter.	Hematite-fluorite, Magnetite-fluorite, Magnetite-fayalite, and fayalite zones	Horizontally zoned, including siderite, fluoritic and pyritic zones	
Schrikkloof and Kwaggasnek Formations	3000 to 5000	Felsites	Massive and flow banded	Rooiberg Group

2.2.2 The Hematite and hematite-fluorite units

The Vergenoeg hematite and the hematite-fluorite units comprise a 20-meter-thick succession underlying the 'Vergenoeg sedimentary unit' (Table 2). The hematite units consist of small, concordant, massive greyish hematitic and specularitic fragments interlayered with felsite and hematite-fluorite bodies within a stratified pyroclastic sequence. In contrast, the hematite-fluorite units are smaller, irregular, concordant hematite-fluorite sheets dispersed around the Vergenoeg pipe (Fourie, 2000). These units are believed to be spill-over remnants of lava and pyroclastics (Fourie, 2000). Among these spill-overs, the most prominent is the Plattekop deposit, located 1000 m south of the discordant Vergenoeg volcanic pipe. It covers an estimated area of 800 m^2, with a thickness of 20 m, and dips 10° southeast (Fourie, 2000).

The Plattekop hematite-fluorite unit exhibits a highly variable composition, consisting of fragments ranging from grey to reddish, massive hematite interspersed with fluorite crystals, clasts, and aggregates (Fourie, 2000). Angular crystal faces of the fluorite contribute to a fragmental or breccia texture within the rocks (Fourie, 2000). On average, the Plattekop deposit contains ~ 50 % iron oxides (predominantly hematite), 40 % fluorite, and 10 % quartz (Fourie, 2000). Bedding is observable in certain sections of the sequence, although lava and volcanic structures are sparse (Fourie, 2000). Adjacent to the volcanic pipe, boreholes reveal interlayering between the hematite-fluorite unit and felsite, while in other boreholes, the hematite-fluorite lithology alternates with massive hematite (Fourie, 2000). This conformable hematitic lense is roughly 10 meters thick near the pipe and shows a decrease in thickness to 3 meters roughly 750 meters away from the pipe (Borrok et al., 1998). However, Fourie (2000) noted thin hematite layers in boreholes close to the Vergenoeg pipe, contrasting with earlier observations.

According to Crocker (1985), the Plattekop fluorite deposit forms part of the concordant intrapyroclastic orebodies found within the hematite-fluorite unit of the Vergenoeg Suite and refers to it as the froth-flow channel lag lithology. The fluorite-rich body is underlain by the fines-depleted agglomerates shown by the open triangle in Figure 5. There is evidence of both normal and inverse-graded bedding, where coarse grains are sandwiched/constrained between finer grains at the base and top (Crocker, 1985). This is attributed to internal shear forces influencing the viscous froth-flow ore, composed of halogen-rich (CaF_2) and oxidized siderite-magnetite enriched tuff (Crocker, 1985). There is also evidence of thin (<1 m) interbedded tuff horizons located towards the base of the orebody (Crocker, 1985)

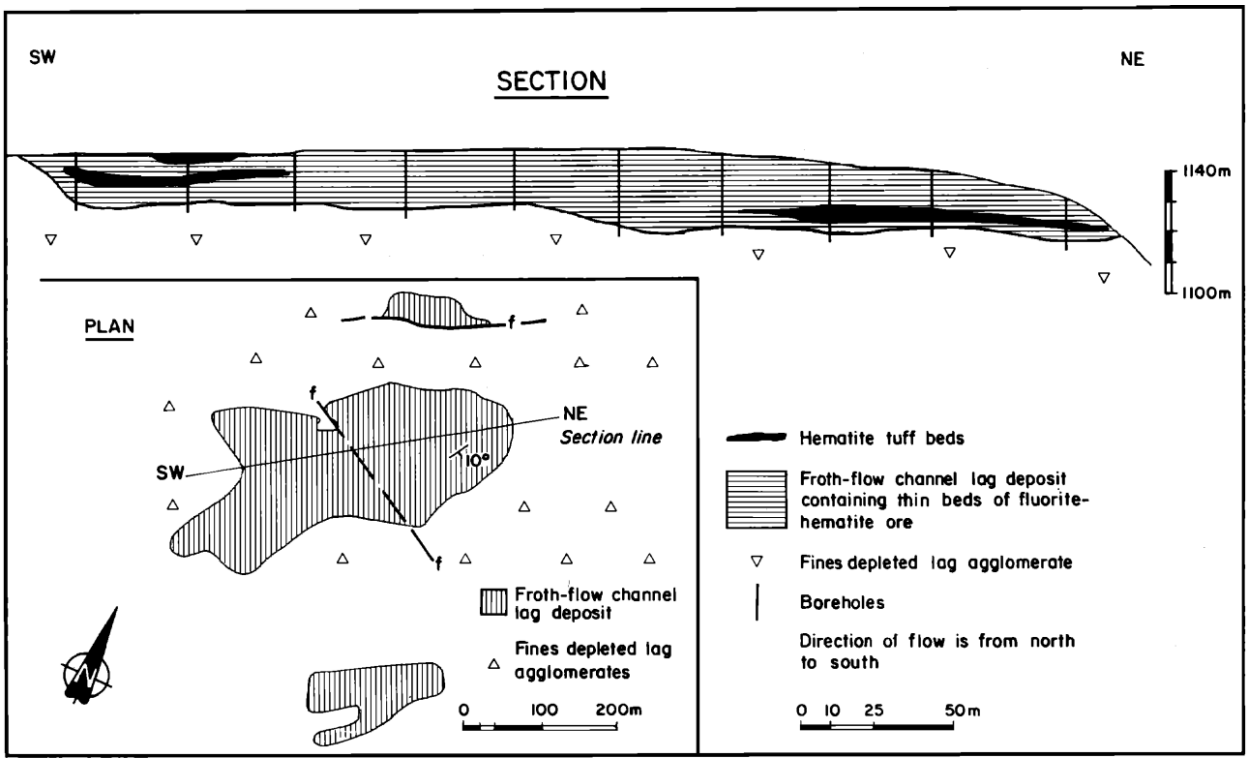

Figure 5. Geological section and plan view of the Plattekop deposit. The section displays the location of the boreholes that were drilled (After Crocker, 1985).

2.2.3 The breccia agglomerate unit

The extrusive breccia agglomerate unit is mainly found on the higher hills near the Vergenoeg pipe. It consists of layers of breccia and agglomerate mixed with tuff (Fourie, 2000). Initially, Crocker (1985) suggested that this unit forms the top of the Volcanogenic Pyroclastic Suite. However, Fourie (2000) disputed this, suggesting that it actually predates the hematite-fluorite and hematite unit. Within these breccias and agglomerates are felsic clasts, ranging from angular to well-rounded, surrounded by a fine-grained matrix of hematite and ferruginous tuff (Fourie, 2000).

2.2.4 The ignimbrite units

Crocker (1985) categorized the basal ignimbrites into several units. Firstly, there is the fines-depleted lag agglomerates, characterized by silica-rich welded lag agglomerates transitioning into ash fall tuff near the vent. It contains angular cherty quartz-rich fragments within a reddish chert-dominated matrix, with petrography revealing crystallized and welded devitrified glass and quartz after tridymite. This agglomerate forms from rapidly agglutinated hypocrystalline perlitic rich in tridymite tuff fragments, creating fused clasts in a welded tuff matrix (Crocker, 1985). Secondly, the fines-enriched ash-fall tuff, considered a distal facies equivalent of the fines-depleted lag agglomerate, consists of fines, ash-fall vitric, and lapilli tuff. It exhibits a multi-coloured appearance and is dominated by tridymite quartz shards, perlitic spheroidal, and glassy clasts, surrounded by crypto-crystalline glass to crystalline quartz. Crocker (1985) also references the froth-flow channel lag deposits and fines-enriched black grass tuff units, detailed in chapter 2.2.2 (Hematite and hematite-fluorite units).

2.2.5 Discordant Vergenoeg Pipe

The Vergenoeg ore field lies within a volcanic pipe-like body (900 m x 600 m) that is oval-shaped in plan view (Figure 6). This volcanic pipe was a conduit of a violent gas-vapour volcanic eruption and referred to as the Vergenoeg discordant volcanic pipe. The pipe intrudes the upper unit of the Rooiberg Group, primarily consisting of rhyolites from the Schrikkloof Formation (Hatton and Schweitzer, 1995). The Vergenoeg pipe is encircled by sedimentary rocks and pyroclastics, comprising agglomerates, BIF, and ignimbrites (Crocker, 1985 and Borrok et al., 1998). The Vergenoeg deposit exhibits vertical zoning, characterized by distinct mineral assemblages, which can be categorized into four units (Goff et al., 2004), including hematite–fluorite, magnetite–fluorite, magnetite–fayalite, and fayalite units, listed from the top to the base (Brandt et al., 2019). Magnetite-fayalite, magnetite-fluorite, and hematite-fluorite units collectively constitute over 90 % of the mineralized body at Vergenoeg (Fourie, 2000).

2.3. Mineralization of the Vergenoeg ore field

Data on mineralization of the Nokeng deposit is limited in literature, therefore, the typical characteristics of the Vergenoeg mineralization are given below with an aim of further comparison.

Over 40 minerals have been found within the ore field along with major fluorite and iron oxides. Accessory mineralization occurs in the form of apatite, monazite, xenotime, REE-F carbonates, and Fe-Cu sulphide minerals (Fourie, 2000). Moreover, patchy limonitic material (i.e., goethite) have also been found close to the water table (Fourie, 2000). According to Fourie (2000), fluorite with a purple colour and elevated phosphate content indicates the micro-inclusions of xenotime, monazite and fluocerite, that are accompanied by U, Th and REE anomalies. In contrast, Cu and Au concentrations within the Vergenoeg ore field are conspicuously low (Fourie, 2000).

Mineralization within the Vergenoeg deposit comprises distinct primary and secondary mineral assemblages. The primary assemblage predominantly constitutes ilmenite, fayalite and fluorite, along with accessory allanite and apatite (Borrok et al., 1998; Schutte, 2005 and Graupner et al., 2015). Hydrothermal alteration of the primary assemblages resulted in the formation of an early secondary mineral assemblage ($T>300^{o}C$), which consists of magnetite, ferroactinolite/grunerite, and subordinate quartz (Borrok et al., 1998). The alteration also formed a late secondary mineral assemblage ($T<300\ ^{o}C$), which comprises siderite, hematite, quartz, pyrite, subordinate fluorite, apatite, and REE-bearing minerals (Borrok et al., 1998). The zoned distribution of these assemblages is attributed to variable degrees of hydrothermal overprint on the indistinct to gradational boundaries between the zones (Brandt et al., 2019). According to Fourie (2000), the primary assemblage is prevalent in the lower portions of the pipe, whereas the secondary assemblage dominates the upper parts of the pipe.

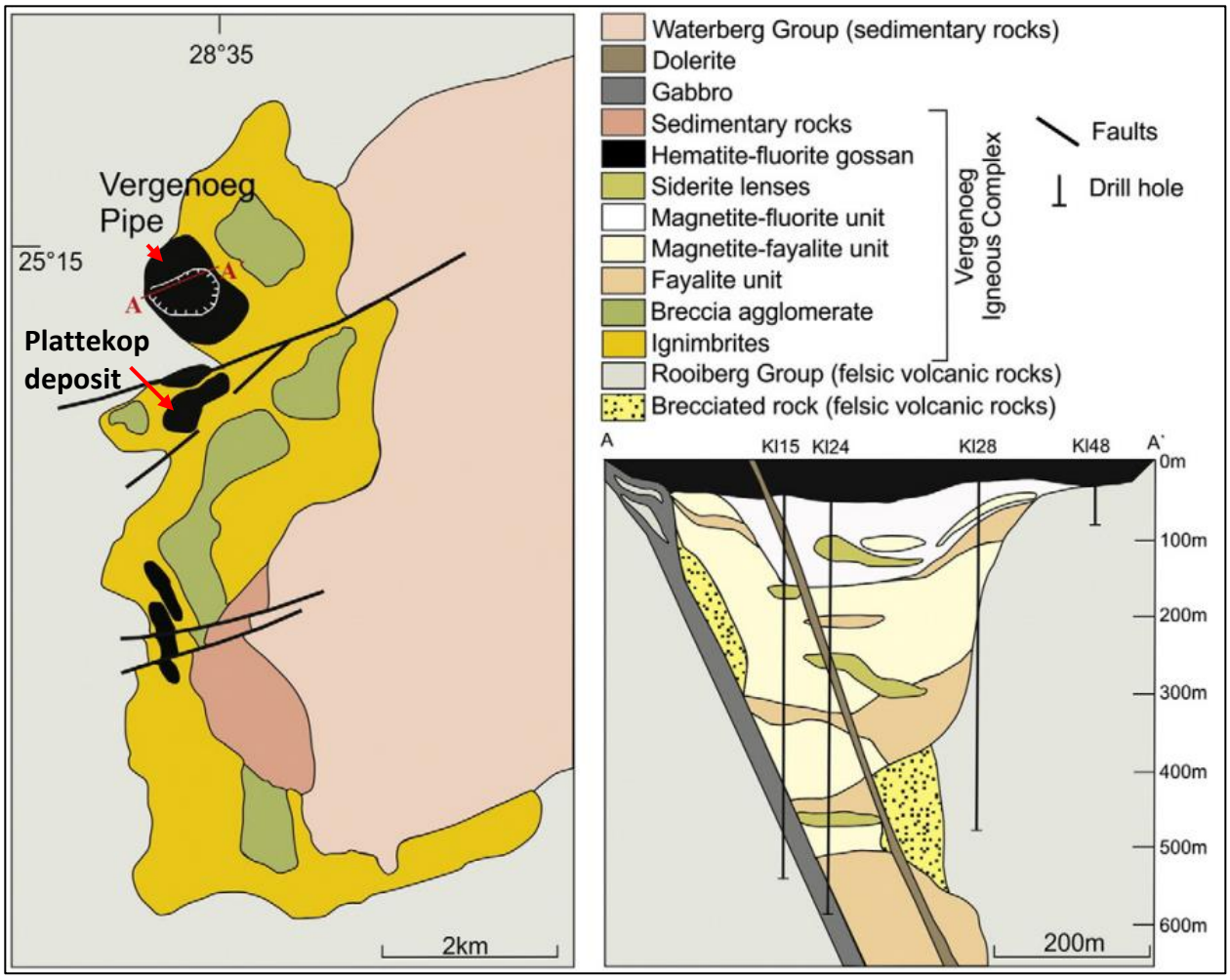

Figure 6. Diagram showing the Vergenoeg Igneous Complex, clearly illustrating the Vergenoeg pipe and the Plattekop deposit. The cross-section on the left displays the Vergenoeg pipe and associated lithological units (taken from Graupner et al., 2015 who modified it after Goff et al., 2004).

2.4 Petrogenesis of the Vergenoeg ore field

There are various models suggested for the formation of the Vergenoeg ore field. Borrok et al. (1998) proposed that the fluorite and magnetite within the ore field precipitated from hydrothermal fluids exsolved from the Lebowa granite. The aforementioned model was supported by Kinnaird et al. (2004) and later Graupner et al. (2015) who argued that a Lebowa-type granitic magma was the source of high field strength elements (HFSEs), which encompass rare earth elements, Y and Nb. Borrok et al. (1998) and Graupner et al. (2015) both postulated amagmatic

formation for the fluid and fluorspar generations, based on the identical εNd values for the Vergenoeg fluorspar and Lebowa granites, whereas the Rooiberg rhyolites show reduced εNd values. Other models include that of Crocker (1985), who suggested that Vergenoeg ore formed when an immiscible iron oxide magma was separated from a parental felsic magma. Lastly, Hou et al. (2017) supported the latter view by the experiments, which showed that the bulk compositions of the Vergenoeg rocks could be formed as a result of immiscibility between quartz-saturated rhyolitic melt and an iron-rich melt crystalizing fluorite, fayalite and primary magnetite. The Fe-rich conjugate melt dissolves up to 6 wt.% F that is yet not sufficient to explain the high fluorite content of Vergenoeg ores suggesting some input of F with hydrothermal fluid (Hou et al., 2017).

Chapter 3: Materials and Methods

3.1 Sampling

Samples were selected from both the Nokeng Fluorite Mine (NK1, NK2, NK3 and NK4) and the Vergenoeg Fluorite Mine (VG1) to investigate the hypothesis that Nokeng is the distal facies of Vergenoeg. These samples were obtained from the University of the Witwatersrand collection. Sampling was focused on mineralized units with a higher potential for hosting accessory mineralization such as monazite, xenotime, allanite, and apatite. Given the pegmatoidal and heterogeneous nature of the Nokeng and Vergenoeg mines, large samples (refer to Figure 7) were collected to adequately capture mineralogical variations within the rocks. Detailed petrographic descriptions of the samples used in this study are provided in Appendix A.

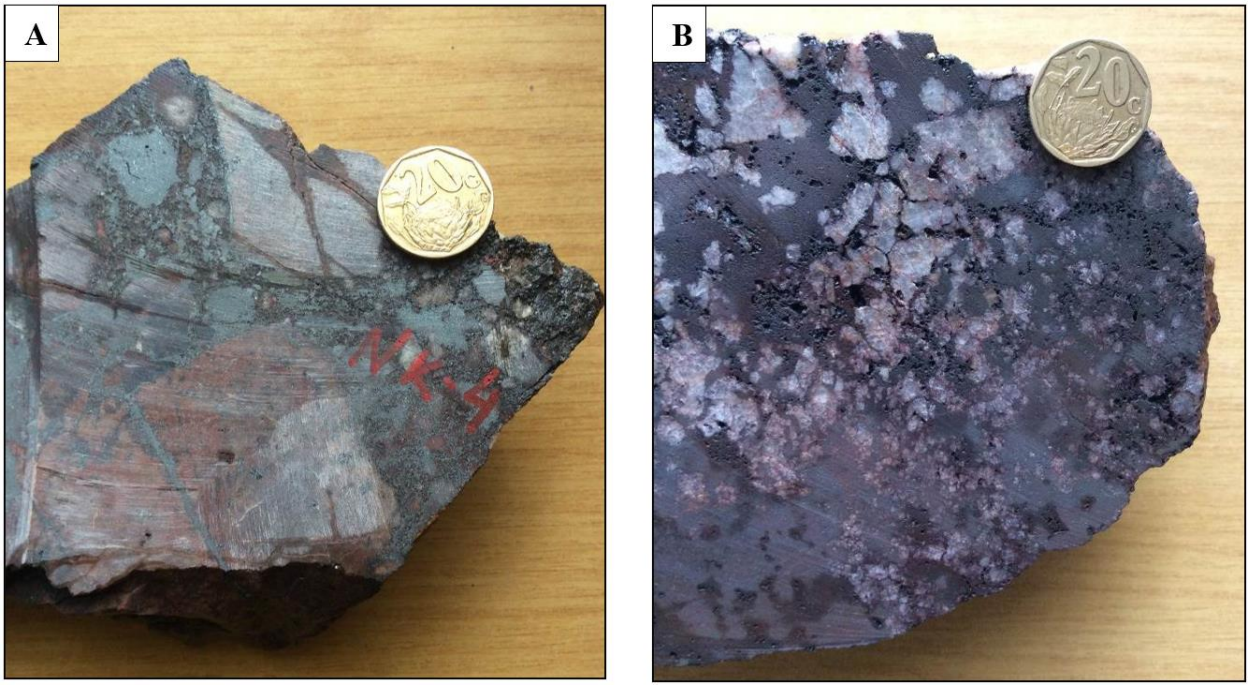

Figure 7. Typical textures of Nokeng and Vergenoeg ores. a) Rock sample NK4 from the Nokeng open pit mine, displaying a brecciated texture that comprises fragments of rhyolite in fluorspar-hematite matrix. b) Rock sample VG1 of fluorspar-hematite-magnetite breccia from the Vergenoeg open pit.

3.2 Sample preparation

Five rock samples were cut to generate 15 smaller rock samples, designated as NK1A, NK2A, NK2B, NK3A, NK3B, NK3C, NK4A, NK4B, NK4C, NK4D, VG1A, VG1B, VG1C, VG1D, VG1E (Table 3). The off-cuts produced during the preparation of thin sections were taken for milling at the University of Witwatersrand, the Earth-Lab, to produce powders for XRF and ICP-MS analysis. Each sample underwent two 1 minute milling cycle using a carbon-steel swing mill (Figure 8a) to ensure a very fine consistency (ranging between 10-50 microns), after which they were divided into 15 individual sample bags. For samples that were too large for the milling dish (as depicted in Figure 8b), a lab jaw crusher from the Earth-Lab was used to reduce their size. To uphold quality assurance and control and prevent sample contamination, the milling dish was meticulously cleaned after each cycle by milling quartz silica. Further cleaning was carried out using ethanol, an air-pressure gun, and tissue paper.

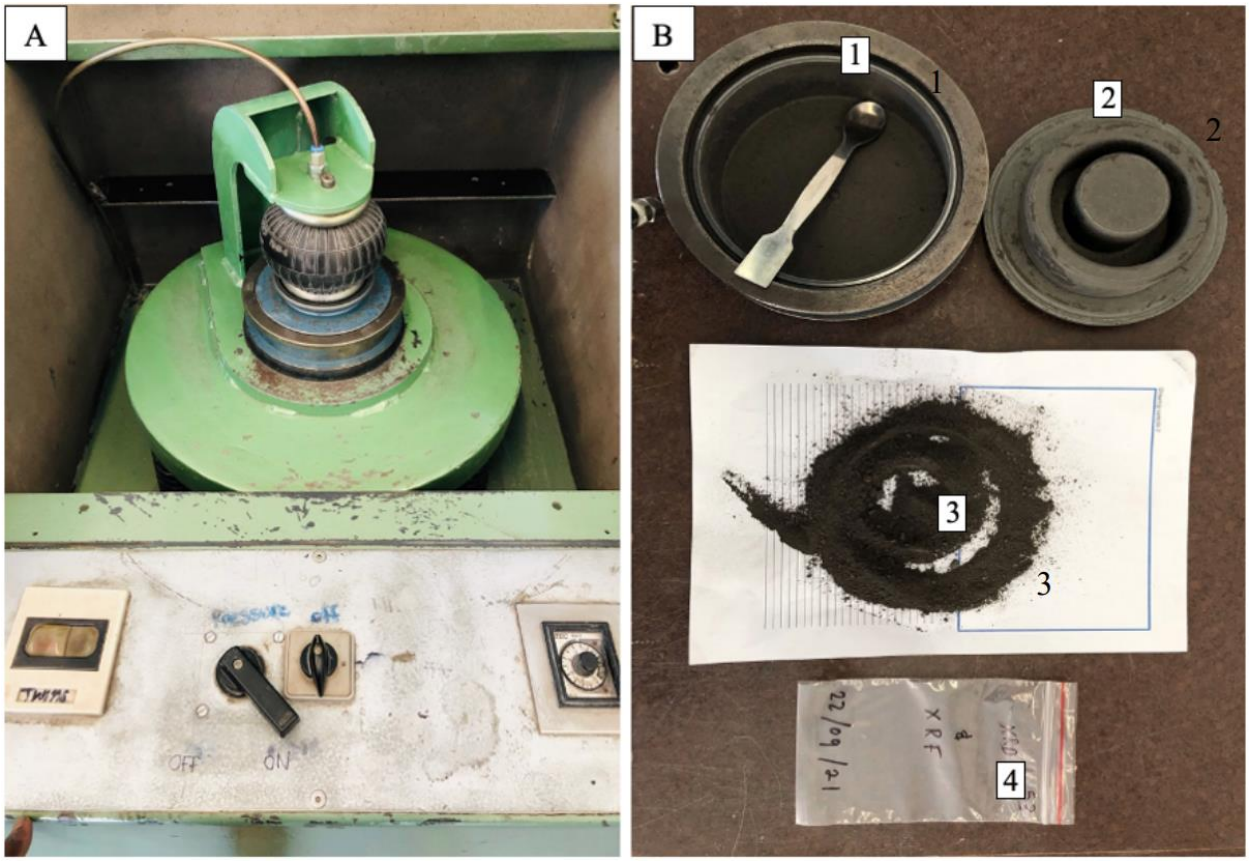

Figure 8. a) Carbon-steel swing mill used to ground the rock samples into powder for geochemical analysis. b) Photograph showing the milling dish that holds the sample material.

3.3 Optical mineralogy

3.3.1 Transmitted light microscopy.

Fifteen rock samples were mounted and cut with a water-cooled saw to produce 30-micron rock slices. These slices were then placed between two glass slides and held together with epoxy to create polished thin sections measuring 40 mm x 25 mm at the Wits Earth Lab. Subsequently, the fifteen polished thin sections were studied using transmitted and reflected light microscopy at the University of the Witwatersrand (WIM Lab). An Olympus BX41 light microscope was used to analyze these thin sections at different magnifications (x4, x10, x20 and x40). High-resolution photomicrographs of all the thin sections were captured using a camera attached to the Olympus BX41 microscope, providing visual representations of the mineralogy present in each sample. Detailed petrographic descriptions of individual samples were conducted, focusing on texture, grain sizes, zoning, and alteration. The primary objective of these descriptions was to investigate similarities and variations between the Vergenoeg and Nokeng samples and to identify any accessory rare earth element (REE) mineralization, such as xenotime, monazite, allanite, and apatite.

3.3.2 Scanning Electron Microscopy and Automated Mineralogy

In this study, the mineralogical phases of the hematite-fluorite ore, eruptive breccia and magnetite-fluorite ores were characterised using TIMA with VegaTCx64 tungsten hardware and TIMA software version 2.9.0 at the School of Geosciences, University of the Witwatersrand. The TIMA is an automated scanning electron microscope (AutoSEM) capable of rapidly analysing the mineralogical phases of samples. This system utilizes both energy dispersive X-ray spectrometry (EDS) and Backscattered electron (BSE) signals to identify and compositionally image minerals. The TIMA analysis was conducted after petrographic work, and the results from both mineral analysis methods were compared. The TIMA liberation analysis methods was employed on two polished thin sections, namely NK1A (hematite-fluorite ore) and VG1A (magnetite-fluorite ore). For each sample, an initial rough run (liberation analysis) was conducted to deduce where the REE mineralization is concentrated in the thin sections. Then, two areas in each thin section (sections A and B) which showed an enrichment in REEs were chosen for a more detailed liberation

analysis. These two sections chosen for analysis are well defined in Figures 16a and b. Phase maps, elemental maps, elemental deportment, mineral locking, and other output data were collected for each section.

Prior to data acquisition, TIMA was carefully calibrated to ensure accurate and reliable measurements and the samples were carbon coated. During quantitative analyses, the beam conditions on the VegaTCx64 were set at 25 kV for the electron beam, with a beam current of 4.2 nA, a beam intensity of 17.5W/cm^2, a spot size of 533.62 nanom, while maintaining a working distance of 15 mm. The measurement parameters on the TIMA software including the acquisition mode, analyses type and pixel spacing were defined using liberation analyses and both dot and high-resolution mapping with pixel spacing set at 1 µm and 3 µm respectively. The maximum and the minimum BSE intensities were set at 100 % and 10 % respectively, with x-ray counts at 1000 per pixel and the dot spacing was adjusted to 9 microns. BSE imaging speed was configured to 4 µ/s.

The mineralogical characteristics of samples NK2A and NK4B were also investigated using a TESCAN Vega SEM. The instrument is housed at the University of the Witwatersrand's Biology building and operates under the Microscopy and Microanalysis Unit (MMU). The TESCAN Vega SEM, utilizes a tungsten filament, which serves as a pivotal analytical tool for the examination of the samples. Prior to SEM analysis, a sample preparation procedure includes carbon coating to minimize charging effects. Subsequently, the prepared samples underwent SEM examination, operating under optimal conditions including a 10 kV accelerating voltage and a beam current of 2 µA to ensure high-resolution imaging and elemental detection capabilities. Detailed microstructural features such as grain morphology, texture, and mineral assemblages were examined and documented through high-resolution SEM images generated by the TESCAN Vega SEM. EDS analysis facilitated the elemental characterization of mineral phases present within the samples, providing semiquantitative estimates of the element concentrations.

3.4 Geochemical analysis

3.4.1 X-ray Fluorescence analysis

X-ray fluorescence (XRF) analysis was utilized to obtain the chemical composition of the Nokeng and Vergenoeg samples (Table B.1, Appendix B). The chemical analysis of these samples was conducted at the University of the Witwatersrand (Earth Lab). The first step involved measuring the loss of ignition (LOI) by heating 1g of milled sample at 1020 ^{o}C for 40 minutes and recording the weight change. Secondly, a $LiBO_4$ flux (1.75g) was added to platinum crucibles and heated for 40 minutes at 1020 ^{o}C. Lastly, ignited flux was mixed with 0.34 g of pre-ignited sample and heated to 1020 ^{o}C for 50 minutes (Figure 9b). The resultant molten material was then poured into a disk and pressed into a solid form, which was then analyzed using a PANalytical WDXRF equipped with a Rh tube. The PANanalytical WDXRF possesses a detection limit of around 0.01 wt.% for major elements with an analytical uncertainty better than 1 rel.% based on the measurements of the international standards (NIM-P, NIM-D, W2, NIM-S, GSP2, BCR2, NIM-N, NIM-G, PCC1, BHVO2, AGV2, G2, DTS1)

The major elements analysis was used for correlation analysis between the Nokeng and Vergenoeg samples. Major elements are also vital in outlining the degrees of alteration and weathering. The major element analysis data was further utilized to create discrimination plots and diagrams to deduce the rock provenance correlations between the rock suites.

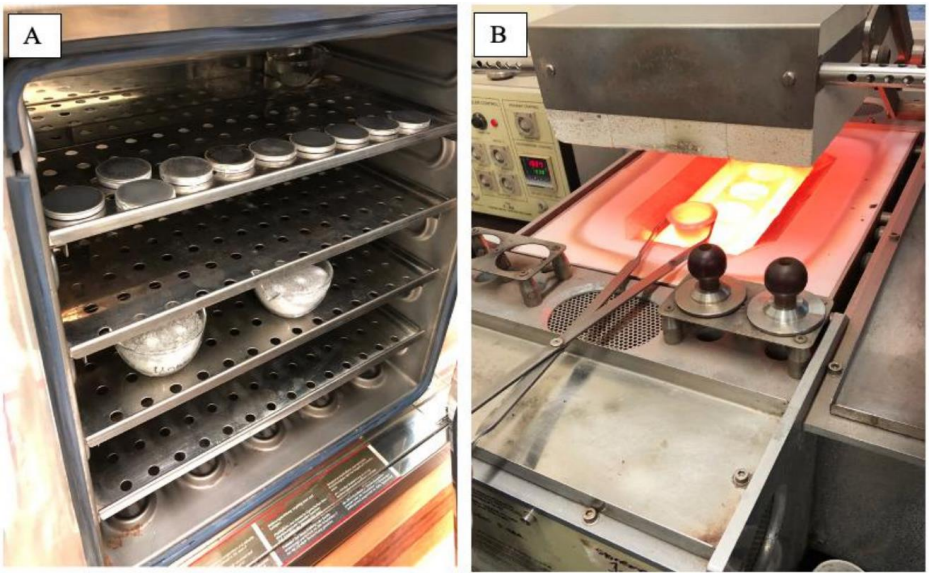

Figure 9. a) Oven used to dry the samples at various temperatures. b) Furnace used to heat XRF mixtures to 1020 ºC.

3.4.2 Inductively Coupled Plasma Mass Spectrometry

Inductively Coupled Plasma Mass Spectrometry (ICP-MS) analysis was conducted to supplement the XRF and provide a wider range of elements, most importantly REEs. Only samples Vg1A, NK1A, NK2A, NK3A, and NK4A were submitted for ICP-MS analysis at the Earth Lab, University of the Witwatersrand (Table B.2, Appendix B). A Perkin Elmer Elan DRC ICP-MS machine, with a standard crossflow nebulizer, was used to analyze the samples. This machine provides detection limits of better than 0.005-0.01 ppm. A 50 mg sample of powdered rock was first dissolved in a solution of 6.1 mL of hydrofluoric acid and nitric acid at a 2:1 ratio. The solution was then heated to 190 ºC and allowed to settle for 55 minutes. The solution was rinsed with 10% NHO_3, and a hotplate was used to dry it to 70 ºC. There were two more additions of 2 mL NHO_3, which were dried to 60 ºC over 24 hours and then to 70 ºC. The solution was removed from the hotplate, and a final addition of 300 µL NHO_3 was made. This method precisely determines concentrations of elements such as Li, Rb, Cs, Sr, Ba, Zr, Hf, Nb, Ta, Y, Sc, Th, along with all the REEs (La, Ce, Pr, Nd, Pm, Sm, Eu, Gd, Tb, Dy, Ho, Er, Tm, Yb, Lu). Certified standard reference materials (BCR-1, BHVO-2 and BIR-1) were digested and analyzed as unknowns returning <10 rel.% deviation.

Table 3: Lists all samples analysed in this study along with their corresponding lithological units and the type of analysis performed on each sample.

Samples	Lithological Unit	XRF	Microscopy	ICP-MS	TIMA	SEM
NK1A	Hematite-fluorite	X	X	X	X	
NK2A	Hematite-fluorite	X	X	X		X
NK2B	Hematite-fluorite	X	X			
NK3A	Hematite-fluorite	X	X	X		
NK3B	Hematite-fluorite	X	X			
NK3C	Hematite-fluorite	X	X			
NK4A	Breccia agglomerate	X	X	X		
NK4B	Breccia agglomerate	X	X			X
NK4C	Breccia agglomerate	X	X			
NK4D	Breccia agglomerate	X	X			
VG1A	Magnetite-fluorite	X	X	X	X	
VG1B	Magnetite-fluorite	X	X			
VG1C	Magnetite-fluorite	X	X			
VG1D	Magnetite-fluorite	X	X			
VG1E	Magnetite-fluorite	X	X			

Chapter 4: Petrography

Macroscopic and microscopic examinations of hand specimens and thin sections were conducted to analyse the mineralogical , mineral association, grain sizes, textural attributes, and other key features of Nokeng and Vergenoeg rock samples. These examinations aid in deducing the origin of the rocks, and depositional environments. Furthermore, the petrographic analysis helps in investigating the geological processes that influenced the rocks after their formation, such as hydrothermal alteration, metamorphism, and weathering.

Several samples from the hematite-fluorite unit were selected for petrographic analysis, including two hand specimens (NK1A and NK2A) and four thin sections (NK1A, NK2A, NK3A, and NK3C). Four representative samples from the rhyolitic breccia were also chosen, including 2 hand specimens (NK4A and NK4C) and 2 thin sections, which are NK4A and NK4B. Lastly, Vergenoeg fluorite ores were analysed, represented by two hand specimens (VG1A and VG1B) and three thin sections (VG1A, VG1E and VG1C). The petrographic results of rock samples (e.g., NK2B, NK4C, and etc) not included in this section are found in Appendix A

4.1 Rock and petrographic descriptions

4.1.1 Hematite-fluorite unit

The macroscopic analysis conducted on NK1A from this unit reveals that it is composed predominantly of hematite and fluorite; along with rhyolitic clastic material partially replaced by disperse hematite (Figure 10a). Hematite displays a reddish colour, leaving a red mark on a streak plate. Blackish specularitic hematite is unevenly distributed throughout the whole sample enriching some fragments (Figure 10a). Hematite evidently forms a matrix that supports fluorite grains. These fluorite grains are coarse grained, ranging in size from 2 mm to 4 mm, resulting in a slightly inequigranular texture. The fluorite possesses a whitish to grey colour, and the overall texture in Figure 10a resembles a porphyritic or clastic texture in the breccia-like rock. Figure 10b also represents the hematite-fluorite unit; however, it differs from Figure 10a in that it displays a phaneritic texture with interstitial fluorite grains that attain sizes between 1 mm and 2 mm.

The microscopic analysis of the hematite-fluorite samples was conducted at the lowest magnification (4x) owing to the generally large grain sizes observed in the unit. Figure 10c depicts

interstitial quartz grains positioned between fluorite and hematite. These quartz grains exhibit a low birefringence and have sizes ranging from 66 µm to 166 µm. The fluorite grains in Figure 10c vary in size, ranging from ~33 µm to ~1000 µm. The smaller fluorite grains in Figure 10c, together with hematite, form a matrix surrounding the larger fluorite grains and interstitial quartz. Figure 10d shows a massive magnetite grain (~2000 µm) that has been replaced by reddish hematite, with minor black traces indicating resorption. This hematite pseudomorph after magnetite is enclosed by a coarse-grained brownish fluorite aggregates with some fluorite grains containing hematite inclusions.

Replacement and resorption phenomena are also evident in Figure 10e, where hematite replaces silicates located within cavities in fluorite. The fluorite crystal itself is coarse-grained and exhibits subhedral to euhedral shapes with perfect octahedral cleavage planes that intersect at roughly ±120 degrees. Lastly, Figure 10f demonstrates interstitial hematite filling the space between fluorite grains. The fluorite grains display anhedral shapes and variable sizes, ranging from 33 µm to 1500 µm. Widespread hematite replacement of rock fragments, former magnetite clasts and fine-grained clastic tuffaceous matrix resulted in a breccia-like texture of the ore.

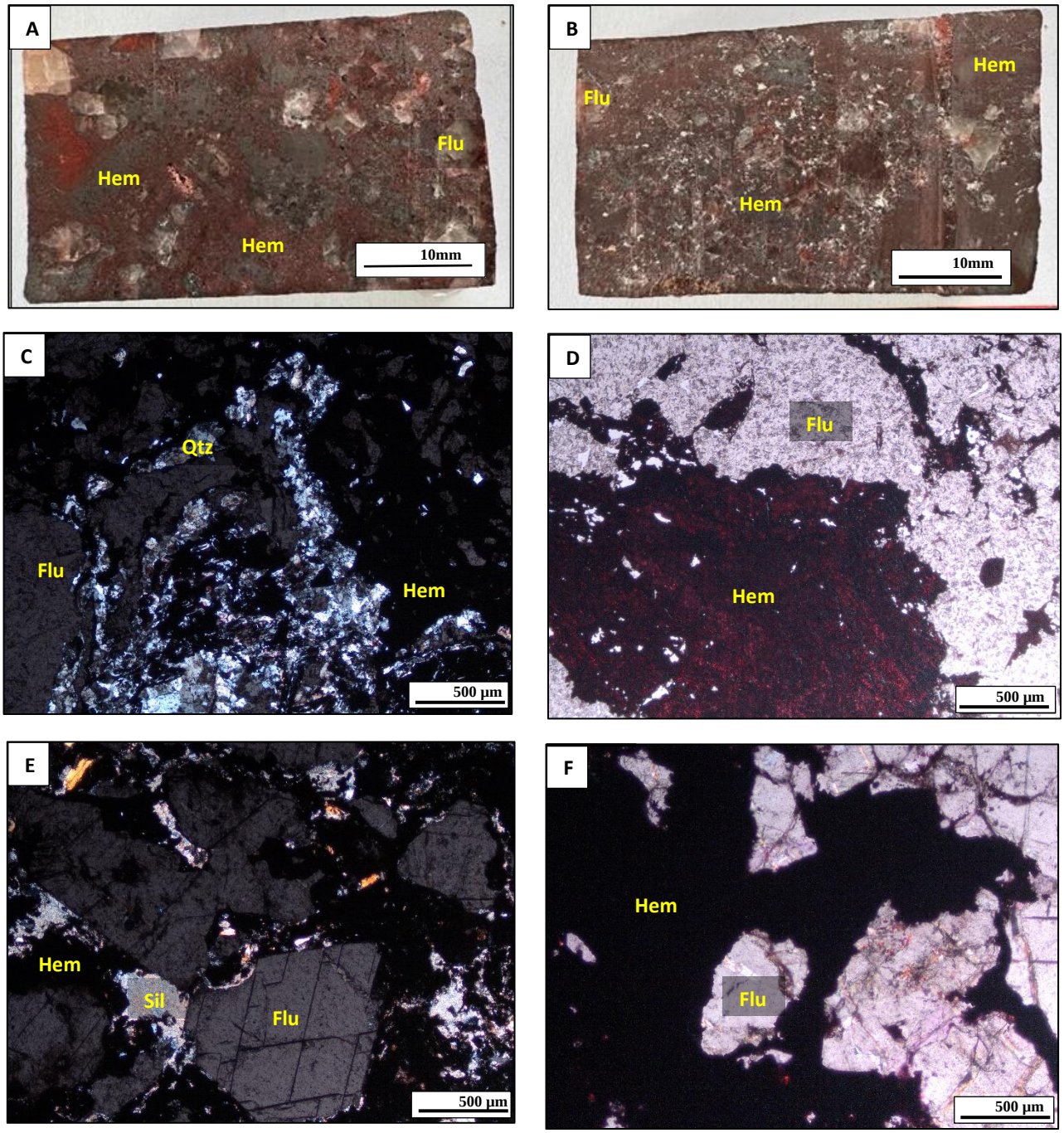

Figure 10. Photographs of hand samples and thin-section micrographs of hematite-fluorite breccia-like ore. a) Hand sample of NK1A. b) Hand sample of NK2A. c) PPL image of NK1A. d) PPL image of NK3A. e) PPL image of NK2A. f) PPL image of NK3C. Abbr.: flu-fluorite; hem-hematite; sil-silicates; qtz-quartz.

4.1.2 Nokeng rhyolitic breccia

The Nokeng Mine's rhyolitic eruptive breccia, represented by the NK4 sample, was also analysed using both macroscopic and microscopic analytical methods. Figure 11a shows a part of a large rhyolite clast, which is roughly 60 mm in size. The rhyolite clast has a brownish red colour, and it is cut by a pervasive specularitic hematite vein (as seen on the top left-hand side in the Fig. 10a) with a thickness of roughly 2 mm. The internal part of the rhyolitic clast contains interstitial specularitic hematite. This rhyolite fragment is supported by a matrix composed of fluorite and specularitic hematite. The specularitic hematite surrounds the inequigranular fluorite grains of variable sizes, from grains that are 1 mm to those that are ~4 mm in size. The fluorite displays a pinkish and greyish colour. The overall texture in Figure 11a is breccia-like with porphyritic habit of fluorite grains. A clear cut/sharp boundary (marked in red in the Fig. 11) separates the fluorite aggregate and the specularitic hematite-fluorite matrix. Figure 11b shows similar mineralogy and texture to those in the Figure 11a, with the fluorite-hematite matrix being more defined. This type of breccia can be defined as lithic lag breccia, which forms synchronously with ignimbrite but represents facies proximal to the centre of the eruption.

The microscopic examination of the breccia reveals great variations in mineral assemblages and textures due to compositionally contrasting clasts. Figure 11c exhibits a quartz grain with a massive central core surrounded by fibrous spherulitic rim indicating recrystallisation of volcanic glass around either quartz shard or phenocryst. The quartz aggregates commonly have interstitial hematite filling in the spaces between the grains. Notably, Figure 11d illustrate the acicular quartz texture. Interstitial hematite and subhedral fluorite separate pseudomorphs from recrystalized fine-grained quartz devoid of needle-like features. Figure 11e showcases a massive fluorite grain with subhedral hematite inclusions, which, in turn, are harbouring silicate minerals. Figure 11f exhibits distinct quartz after tridymite with acicular textures on their peripheries.

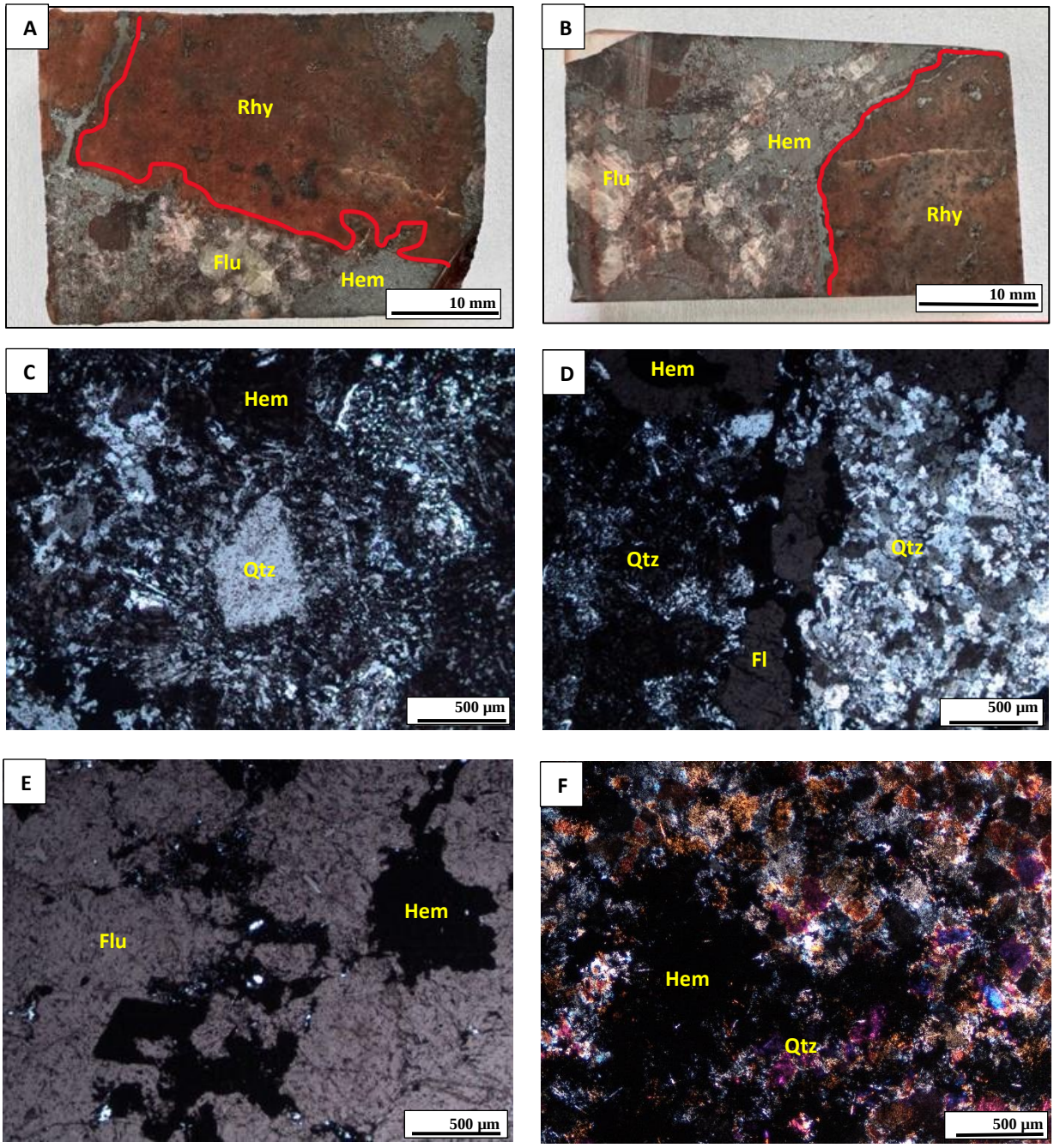

Figure 11. Photographs of hand samples and thin-section micrographs of eruptive breccia. a) Hand sample NK4A with rhyolite clasts in hematite-rich matrix with minor fluorite b) Hand sample NK4C with rhyolite clasts in fluorite-hematite matrix. c) PPL image of NK4A d) PPL image of NK4A. e) PPL image of NK4A. f) PPL image of NK4B. Abbr.: flu-fluorite; hem-hematite; rhy-rhyolite; qtz-quartz.

4.1.3 Magnetite-fluorite unit

This unit is represented by the rock samples collected from the Vergenoeg open-pit fluorite mine, namely VG1. The hand sample in Figure 12a displays massive, vuggy magnetite, with a greyish-black colour. The magnetite grains are roughly 20 mm in size, whereas the cavities/holes range between ~1 mm and 4 mm in size. Minor hematite replaces magnetite that is distinguished by a reddish oxidation colour. The magnetite grains share a clearly defined/sharp contact with coarse grained euhedral fluorite crystals that are highly fractured (Figure 12a). These fluorite grains have a milky to greyish colour and vary in size from approximately 9 to 13 mm. Figure 12b shows a fragment of the VG1 sample that is composed predominantly of magnetite. Magnetite in Figure 12b is similar to the magnetite in Figure 12a as it is also massive, greyish black in colour and has a vuggy texture. The space between massive aggregates of magnetite is filled by medium grained fluorite grains with a size ranging between ~1 mm to 4 mm (Figure 12b). The fluorite in this sample has a pinkish colour due to disperse iron oxide admixture and possess a phaneritic texture.

Microscopic analysis of the VG1 fluorite samples reveals several key features. All samples (VG1A to E) exhibit massive fluorite grains, typically subhedral to euhedral and displaying a dull pinkish grey color. These fluorite grains may be brecciated with crosscutting veinlets of hematite and magnetite. Figure 12a shows pervasive maroon hematite veinlets and disseminated subhedral magnetite veinlets traversing the fluorite aggregates. Similar magnetite vein-like aggregates are observed in the fluorite in Figure 12d, where fluorite is surrounded by massive magnetite. Notably, Figure 12e displays collomorphic hematite rims surrounding and replacing magnetite, with both minerals engulfing fluorite grains. Figure 12e exhibits hematite lamellae inside fluorite grains that was not observed in the other samples. Massive magnetite surrounding the fluorite with hematite lamellae is itself entrapped by larger fluorite grains.

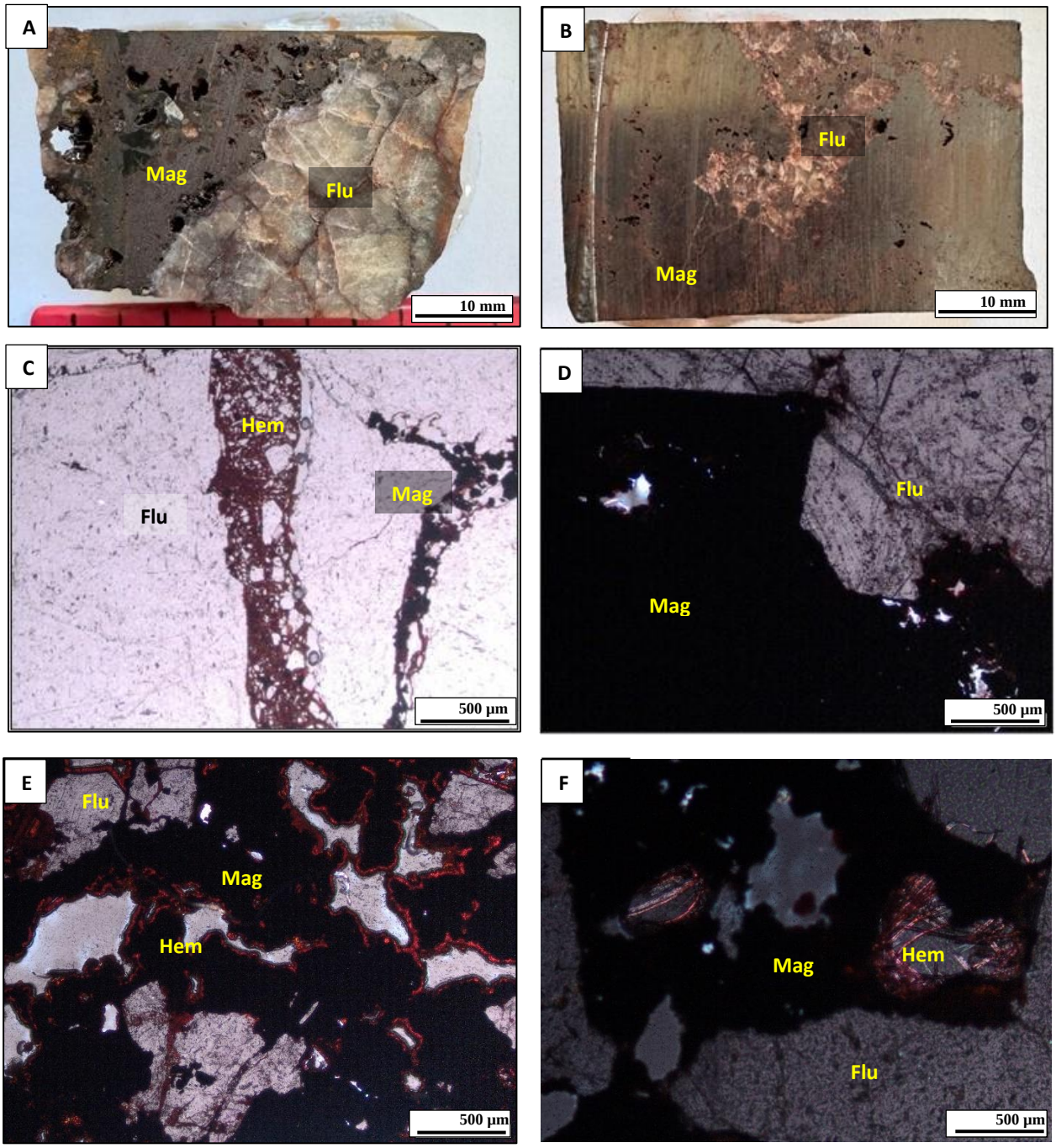

Figure 12. Photographs of hand samples and thin-section micrographs of the magnetite-fluorite unit. a) Hand sample of VG1A. b) Hand sample of VG1B. c) PPL image of VG1A. d) PPL image of VG1A. e) PPL image of VG1E. f) PPL image of VG1C. Abbr.: mag-magnetite; flu-fluorite; hem-hematite.

The observations show that (i) quartz is mostly associated with clasts of rhyolites and is subordinate to accessory in hematite-fluorite ore; (ii) the spherulitic texture is common in rhyolite clasts and was not observed in the matrix of all studied rocks; (iii) the stratified texture of the Nokeng NK2 sample indicates flowage control of clast distribution whereas all other samples demonstrate irregular arrangement of clasts; (iv) relics of primary magnetite are absent in the Nokeng hematite-fluorite ore whereas they are obvious in the Vergenoeg magnetite-fluorite ore; (v) the variable textures of fluorite indicate its primary origin although clastic provenance of some fluorite grains in the Nokeng rocks cannot be excluded.

Chapter 5: Whole Rock Geochemistry

The geochemical analysis of major and trace elements in the hematite-fluorite ores, eruptive breccia, and magnetite-fluorite ores provides insight into the compositional similarities and variations between these three lithologies. The major element analysis provides essential information for classifying rocks into different types based on their chemical composition. The major oxides are the constituents of minerals that make up rocks and ores, therefore, their proportions control the proportions of minerals. For the purpose of this study, the trace elements have been grouped into large ion lithophile elements (LILE), high field strength elements (HFSEs) and lastly REEs.

The category of "large-ion lithophile elements" encompasses K, Rb, Sr, Cs, Ba, Pb, and Eu^{2+} (Gast, 1972; Saunders et al., 1980; Rudnick, 1998), which are characterized by their large ionic radii and relatively low charge (Saunders et al., 1980). Elements such as Rb, Sr and Ba were discussed in this chapter, because the character of these elements allows for elucidation of fundamental geochemical processes.

The high-field strength elements constitute a cluster of incompatible elements, each characterized by relatively small ionic radii and/or high charge (such as Th, U, Ce, $Pb^{4+,}$ Zr, Hf, Ti, Nb, Ta). These elements serve as valuable indicators for discerning the tectonic environments in which rocks originate (Pearce et al., 1984). Typically, they are deemed incompatible as they tend to remain within the melt and do not readily enter into primary rock-forming minerals (White, 2001). Several discriminant plots will also be created using these HFSEs.

Lastly, the REEs, which include La, Ce, Pr, Nd, Pm, Sm, Eu, Gd, Tb, Dy, Ho, Er, Yb, Tm, and, Lu, were analysed, together with the chemically similar Y and Sc. These elements are imperative to this study and their analysis aligns with key objectives of the research. However, only REEs with distinguished or elevated concentrations compared to the other REEs within the deposit were analysed in detail. This includes, Ce, La, Y and Nd, which revealed high concentration following the ICP-MS analysis. REE chondrite normalized plots and other plots are created to better decipher the geochemical character of the REEs +Y.

5.1 Major element geochemistry

The geochemical analyses conducted on the Nokeng hematite-fluorite, Nokeng rhyolitic breccia and magnetite-fluorite units reveal significant variability in silica content (Figure 13a-d). The Nokeng hematite fluorite unit has a range in SiO_2 content from 0.32 wt % to 32 wt%; this unit possesses a relatively low silica content overall. Silica content within the Nokeng breccia is relatively higher with its content ranging from 26.1 wt.% to 57 wt.%. The hematite-fluorite unit displays a smaller variation in SiO_2 content between individual samples (1.24 wt.% to 1.91wt.%), compared to Nokeng hematite-fluorite and the Nokeng breccia. The magnetite fluorite ores possess the lowest average SiO_2 content, whereas the Nokeng breccia has the highest average SiO_2 content. The Nokeng breccia displays low CaO content compared to the other units, whereas the Nokeng hematite-fluorite and Vergenoeg magnetite-fluorite ores possess moderate to high concentrations of CaO (Figure 13a). There is also a wide variation in CaO content of individual samples within the same units (e.g., VG1C has a CaO content of 45.2 wt.% whereas VG1B has a value at 27.4 wt.%). Figure 13a shows a relative decrease in CaO with increasing SiO_2 content.

The iron content is relatively balanced between the different units (Figure 13b), however, there is a notable disparity in the FeO^t content between samples of the same unit (e.g., NK4B has a concentration of 44.9 wt.% FeO^t whereas NK4A register a lower value at 28.6 wt.% FeO^t). The hematite fluorite unit has the highest average concentration of P_2O_5 followed by the Vergeneog magnetite fluorite unit, and lastly the Nokeng breccia (Figure 13c). The TiO_2 content is variable across all units, with Figure 13d displaying a positive correlation between SiO_2 and TiO_2. Notably, the hematite-fluorite sample NK2 displays the highest TiO_2 content, whereas NK3 shows the lowest concentration of TiO_2 (Figure 13d). The Nokeng hematite-fluorite unit, Nokeng rhyolitic breccia and magnetite-fluorite unit possess relatively low Al_2O_3 and MnO, MgO content compared to average crustal abundances. The units also show lower concentrations of K_2O and Na_2O.

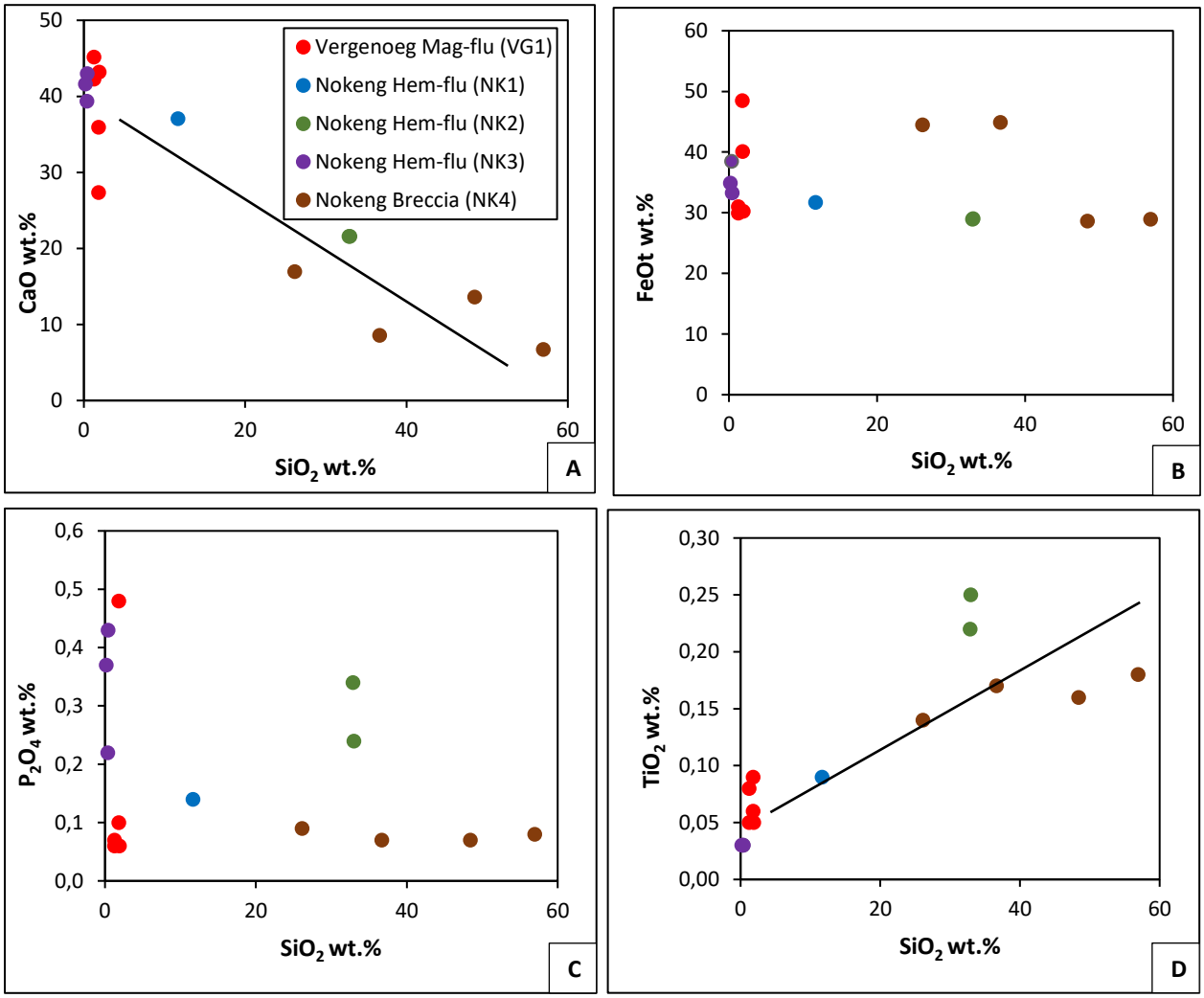

Figure 13. Harker plots showing the relationship between silicon dioxide and major element oxides for the different rock types in the Nokeng and Vergenoeg Mine. The black lines show the trend of the data.

5.2 Trace element geochemistry.

5.2.1 Large-Ion Lithophile Elements

The hematite-fluorite ore displays distinct variations in Rb, Sr, and Ba concentrations across the samples. NK1A reveals lower concentrations (2.48 ppm Rb, 54.9 ppm Sr, 30.5 ppm Ba) compared to NK2A, which shows significant enrichment (77.3 ppm Rb, 61 ppm Sr, 129.6 ppm Ba). NK3A bridges the gap with intermediate values (2.83 ppm Rb, 31.6 ppm Sr, 38.5 ppm Ba). Notably, Cs content of 1.96 ppm in NK3A surpasses that of NK2A despite generally lower LILE concentrations. Moreover, Sr content in NK3A is lower than in NK1A. The eruptive breccia sample (NK4A) shows moderate enrichments in Rb (3.55 ppm), Cs (0.87 ppm), and Sr (23.8 ppm) compared to ores of the hematite-fluorite unit. Notably, the Ba concentration (40 ppm) is significantly higher than that of NK1A and NK3A. In contrast, ores of the magnetite-fluorite unit (VG1A) have significantly lower Rb (1.30 ppm), Cs (0.08 ppm), and Sr (24.8 ppm) contents, but, like NK4A, are distinguished by higher Ba (37.1 ppm) compared to NK1A and NK3A.

Three binary plots (Rb vs Sr, Rb vs Ba and Ba vs Sr) were created to deduce geochemical trends within the studied Nokeng-Vergenoeg samples. It is evident from Figure 14a-c that NK2A hematite-fluorite ore possesses the highest Sr, Ba and Rb content compared to all the samples that were analysed. NK1A is also distinguished by elevated Sr content with respect to the other samples (Figures 14a and c). Notably, in the Rb vs Ba plot (Figure 14b), all the samples except for NK2A, show a similar geochemical composition. Moreover, VG1A, NK3A, and NK4A show relatively similar trends in all the plots (Figures 14a-c).

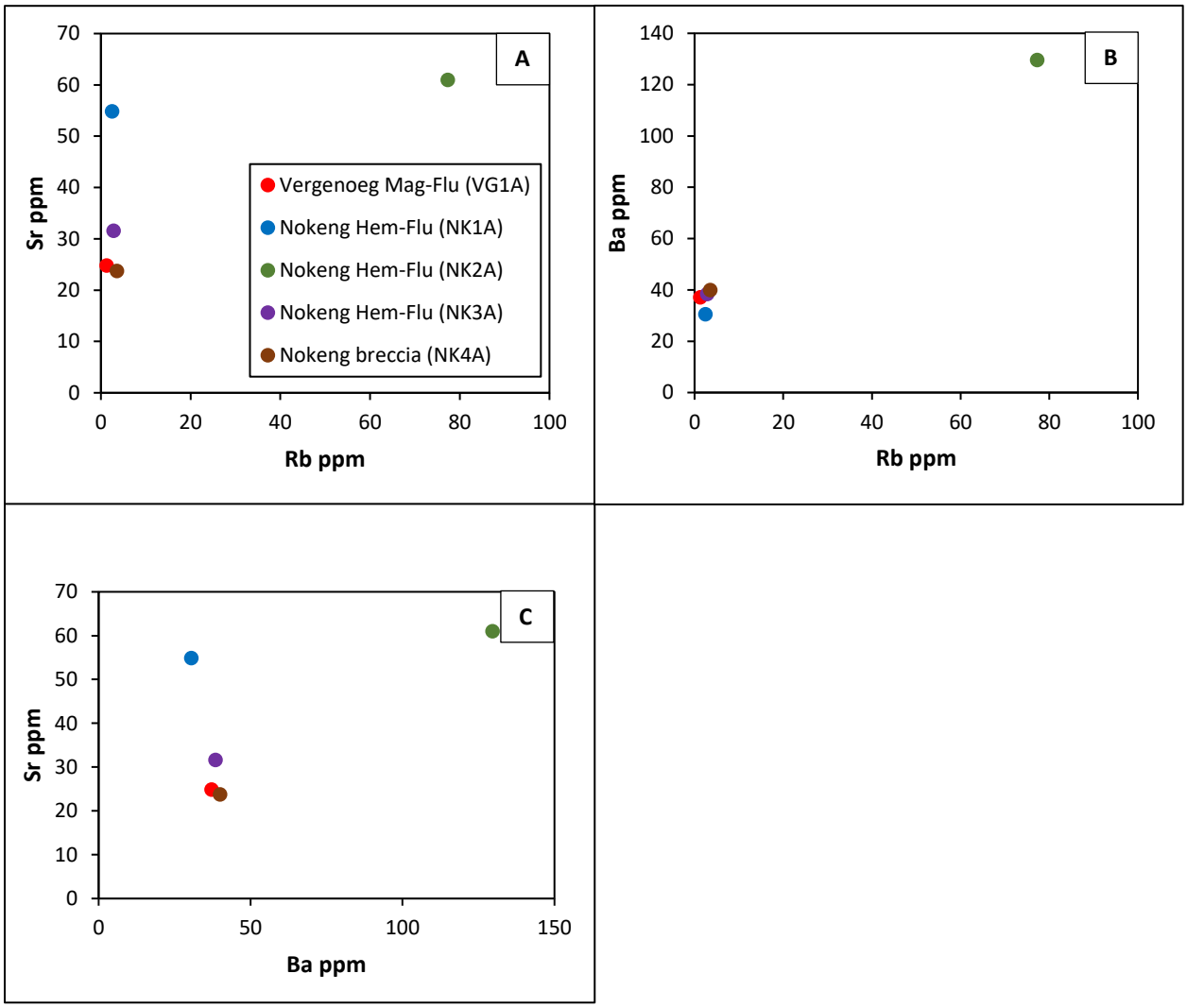

Figure 14. Binary plots of large ion lithophile elements (LILE) found in rocks from Nokeng and Vergenoeg mines. a) Binary plot of Rb vs Sr. b) Binary plot of Rb vs Ba. c) Binary plot of Ba vs Sr.

5.2.2 High Field Strength Elements

The analysis of key trace elements (Ta, Zr, Nb, Ti, Hf) revealed distinct geochemical signatures across the three units. Within the hematite-fluorite unit, NK1A exhibits the lowest concentrations, with 0.95 ppm Ta, 13. 9 ppm Zr, 311 ppm Nb, 1110 ppm Ti and 0.44 ppm Hf. Notably, NK2A shows a contrasting pattern, with higher concentrations of Zr (92.7 ppm), Ti (2172 ppm) and Hf (1.81 ppm), while Ta (0.47 ppm) and Nb (143 ppm) content remains moderate. Interestingly, NK3A presents an intermediate signature, with values of 7.41 ppm Zr and 534 ppm Nb falling between those for NK1A and NK2A. The highest Ta (1.55 ppm) and subsequently the lowest Ti (370 ppm) and Hf (0.34 ppm) among all hematite-fluorite ore samples are found in NK3A. The eruptive rhyolitic breccia (NK4A) displays low Ta (0.33 ppm) and Nb (32.6 ppm) but significantly elevated Zr (243 ppm), Ti (1256 ppm and Hf (4.67 ppm) compared to other rocks in the Nokeng-Vergenoeg area. Lastly, the Vergenoeg magnetite-fluorite ore (VG1A) exhibits moderate concentrations of all incompatible elements, with 2.88 ppm Ta, 7.68 ppm Zr, 314 ppm Nb, 514 ppm Ti and 0.32 ppm Hf falling within the moderate ranges compared to the other samples.

5.2.3 Rare Earth Elements

5.2.3.1 Hematite-fluorite unit

A considerable enrichment in REEs compared to the Primitive Mantle values (Hoffman, 1988) is apparent in rocks and ores of the Nokeng hematite-fluorite unit (Figure 15). The LREEs within the unit are more enriched compared to the HREEs (Figure 15) and the LREE/HREE fractionation increases with the increasing total REE abundances. NK1A is the most LREE-enriched sample within the hematite-fluorite unit with 1191 ppm La, 1842 ppm Ce at over 5300 ppm total REE. NK2A also displays high LREE enrichment at 3221 ppm total REE content whereas NK3A is the least LREE-enriched sample with the total REE content of 2800 ppm. HREE show relatively flatten unfractionated Primitive Mantle normalised patterns with a slightly negative slope for NK2A and NK3A and a positive slope for NK1A (Figure 15). Notably, NK3A shows the highest enrichment in HREE with 62.9 ppm Dy and 54.9 ppm Yb. NK3 has the second highest HREE content, with, NK2 being the least enriched in HREEs. All the Nokeng samples that

were collected (NK1A, NK2A, NK3A) and analysed for REEs show an impressive negative Eu anomaly (Figure 15). The average slopes of the PM-normalised patterns are within 4.5-15.5 $[La/Gd]_N$ for the LREEs and 0.8-1.2 $[Tb/Lu]_N$ for the HREEs. The significantly enriched LREEs in Nokeng ores produce an asymmetric "seagull" PM-normalised pattern (Figure 15). Furthermore, Y concentration in the samples is high with 1805 ppm Y in NK1A, 1517 ppm Y in NK3A and with 641 ppm Y in NK2A.

5.2.3.2 Nokeng rhyolitic breccia

The eruptive breccia, represented by NK4A is relatively depleted in REEs compared to the Nokeng hematite-fluorite ore. The breccia reveals a relative enrichment in LREEs compared to HREEs, with Ce showing the highest concentration at 432 ppm, followed by La at 347 ppm. The HREE content is within a range from 0.9 ppm Lu to 10.3 ppm Dy. The PM-normalised pattern shows a high degree of LREE fractionation, with unfractionated flattened HREE distribution (Figure 15). The slopes of the REE PM-normalised pattern correspond to 29 $[La/Gd]_N$ for the LREEs and 1.1 $[Tb/Lu]_N$ for the HREEs. The sample displays an unremarkable negative Eu anomaly in (Figure 15). The sample also possesses a relatively low Y content at 163 ppm Y.

5.2.3.3 Magnetite fluorite unit

The Vergenoeg magnetite fluorite ore in Figure 15 is distinguished by lower REE content with respect to the Nokeng ore samples. Conversely, the Vergenoeg ore is high in Y, recording a value of 1729 ppm Y, which is higher than some of the Nokeng samples. The sample is also more enriched in LREEs compared to HREEs similar to what is seen in the Nokeng ores. The Vergenoeg magnetite fluorite ore contains 115 ppm La, 239 ppm Ce and 50 ppm Gd. A slope of the LREE PM-normalised pattern is slightly negative with $[La/Gd]_N$ of 2.3. The unit has a low HREE content with 51.7 ppm Dy and 50.0 ppm Yb. The lowest HREE value of 6.8 ppm is recorded for Tm. The PM-normalised plot for the magnetite fluorite (VG1A) ore displays a symmetrical seagull pattern with the mid-section defined by a negative Eu anomaly (Figure 15).

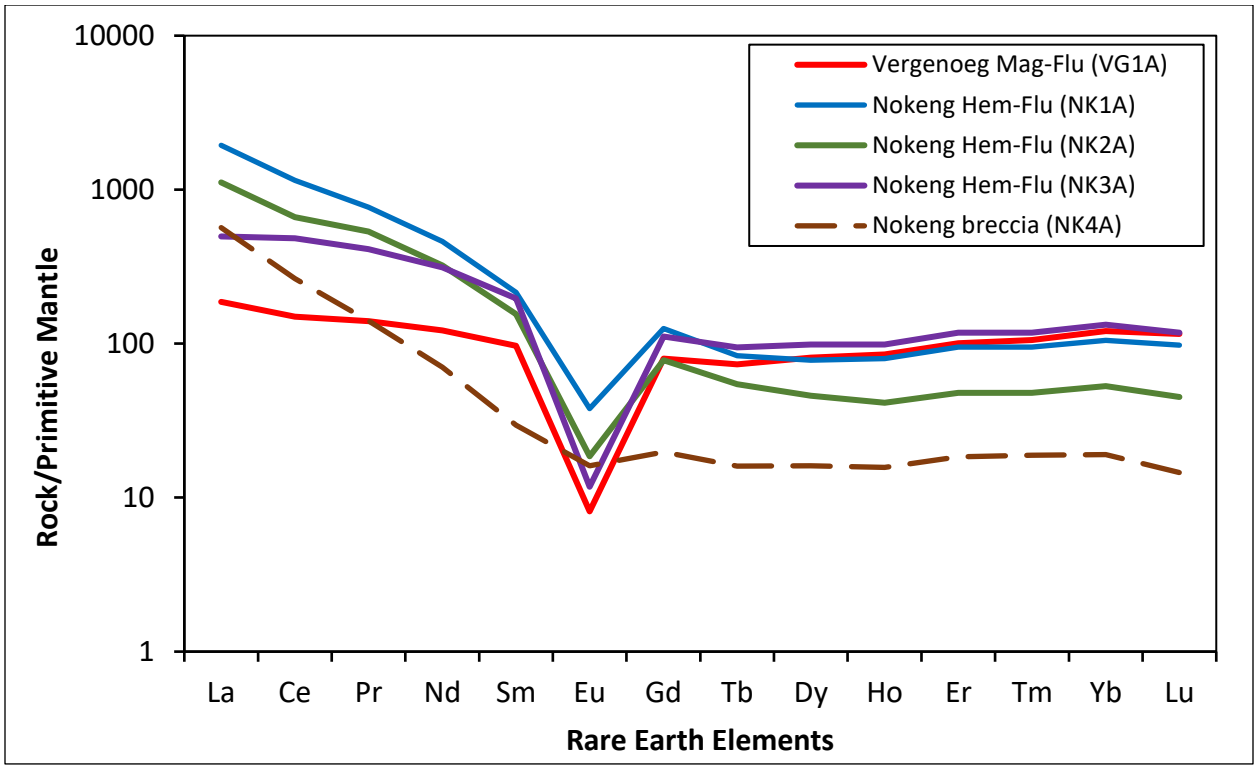

Figure 15. Primitive Mantle normalised REE plot for the Nokeng and Vergenoeg rock samples. The normalization values are from Hoffman (1988).

5.2.3.4 Total REE + Y content of the Nokeng and Vergenoeg rocks

It is evident from Table 4 that NK1A, which represents the Nokeng hematite-fluorite unit, possesses the highest REE + Y content of 5890 ppm. The second highest REE + Y content is recorded for the hematite-fluorite unit sample NK3A, which is followed by NK2A, with REE+Y concentrations of 3408 ppm and 3089 ppm respectively. The magnetite fluorite unit (VG1A) also has a significant concentration of REE+Y, with a value of 2519 ppm. Lastly, the breccia-agglomerate unit, represented by NK4A, shows the lowest concentration of REE + Y, recorded at a value of 1107 ppm.

Table 4: Summary of the total REE+Y content in rocks from various units including the hematite-fluorite unit, the breccia unit, and the magnetite-fluorite unit according to the ICP-MS data in the Table B.2, Appendix B.

Sample	REE + Y (ppm)
NK1A (hematite-fluorite unit)	5890
NK2A (hematite-fluorite unit)	3089
NK3A (hematite-fluorite unit)	3408
NK4A (breccia-agglomerate unit)	1107
VG1A (magnetite-fluorite unit)	2519

Chapter 6: Automated Mineralogy

A TESCAN integrated mineral analyser (TIMA) and a TESCAN Vega SEM were used to search for accessory minerals and semi-quantitively evaluate the mineralogical composition of the Nokeng hematite-fluorite, breccia and Vergenoeg magnetite-fluorite units. The SEM and TIMA have advanced capabilities for mineral identification, elemental analysis, chemical and mineral mapping and providing high resolution imaging. The TIMA liberation analysis was conducted for the hematite-fluorite unit and the Vergenoeg magnetite-fluorite unit, which possess elevated concentrations of target REEs (Figure 16). The TIMA Liberation analysis is an analysis type within the TIMA with acquisition modes that allow for production of high-resolution phase maps and provides information on the modal mineralogy of samples. The liberation analysis also aids in identifying the host of specific elements through elemental deportment. Lastly, the Vega SEM analysis was utilized to study the mineralogical composition and take BSE images of textural relationships in rocks of the hematite fluorite and rhyolitic breccia.

6.1 TESCAN Integrated Mineral Analyser

6.1.1 Mineral proportions in the Nokeng hematite-fluorite ore

Maps displaying the mineral phases found in the Nokeng hematite-fluorite rocks and their respective proportions are shown in Figure 17a and b. It is evident that the Nokeng hematite-fluorite rocks are largely composed of fluorite, quartz, iron oxides, and aegirine (Figures 18a and b). Additionally, REE bearing minerals are present in small proportions in Figure 17a including 0.72% bastnasite, 0.05% monazite, and 0.02% xenotime, along with 0.05% unclassified minerals. Lastly, Figure 17b reveals REE bearing mineral concentrations of 0.26 % bastnasite, 0.18 % monazite, 0.03 % xenotime, and 0.07 % unidentified phases.

It is important to note that the TIMA software is unable to differentiate between hematite and magnetite as they share similar atomic numbers and characteristic X-ray spectra (Pires et al., 2019). As a result, in this study, it was decided to characterise phases containing hematite and magnetite, along with goethite (iron hydroxide) as iron oxides. Similarly, points that did not present a spectrum similar to any of the reference spectra in the database were categorized as unidentified mineral phases, which accounted for <3% across all analysed sample.

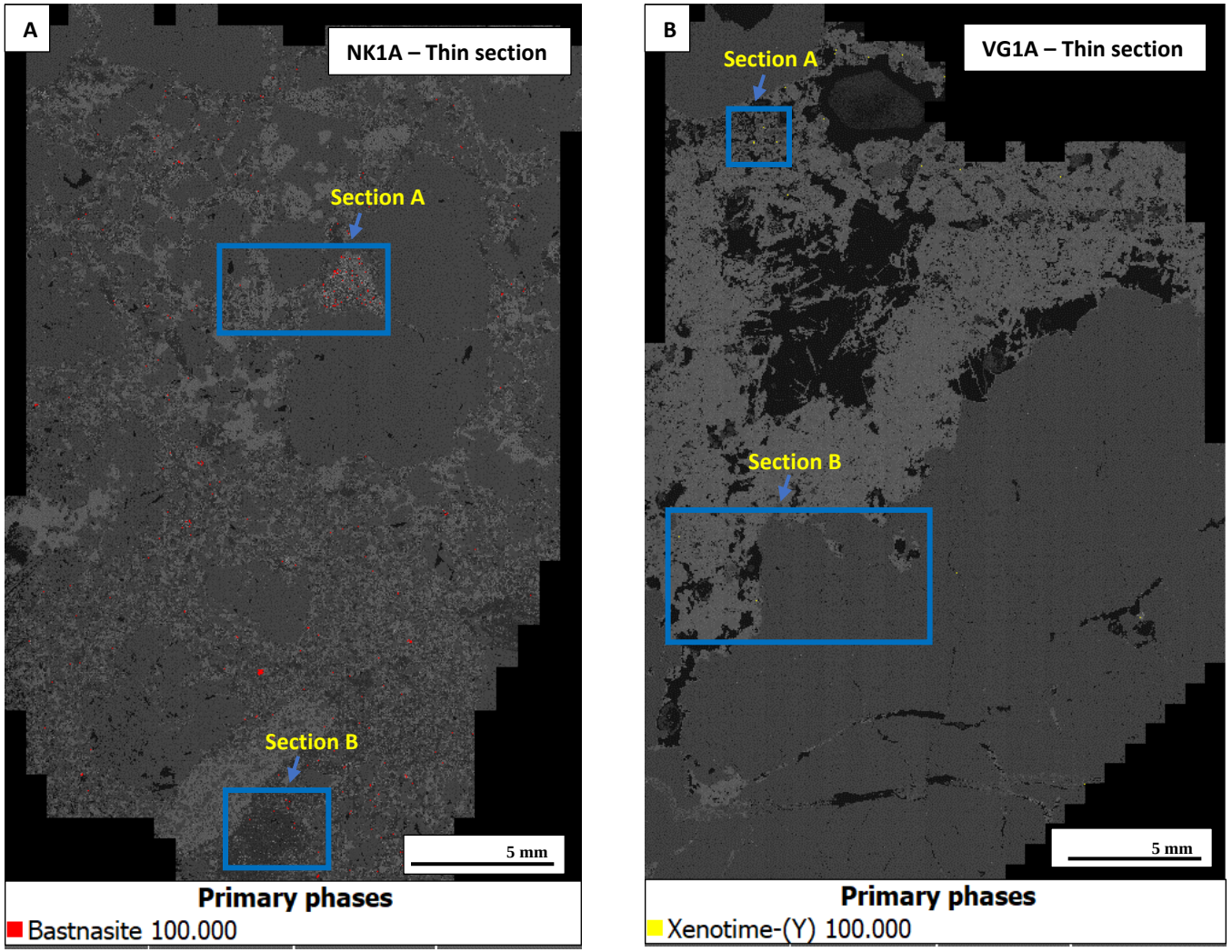

Figure 16. BSE images with REE phases of bastnasite and xenotime highlighted. These images also, show sections/areas on the thin-sections that were chosen for the analysis, represented by the blue boxes. a) This shows bastnasite mineralization in sample NK1A b) This shows xenotime mineralization in sample VG1A.

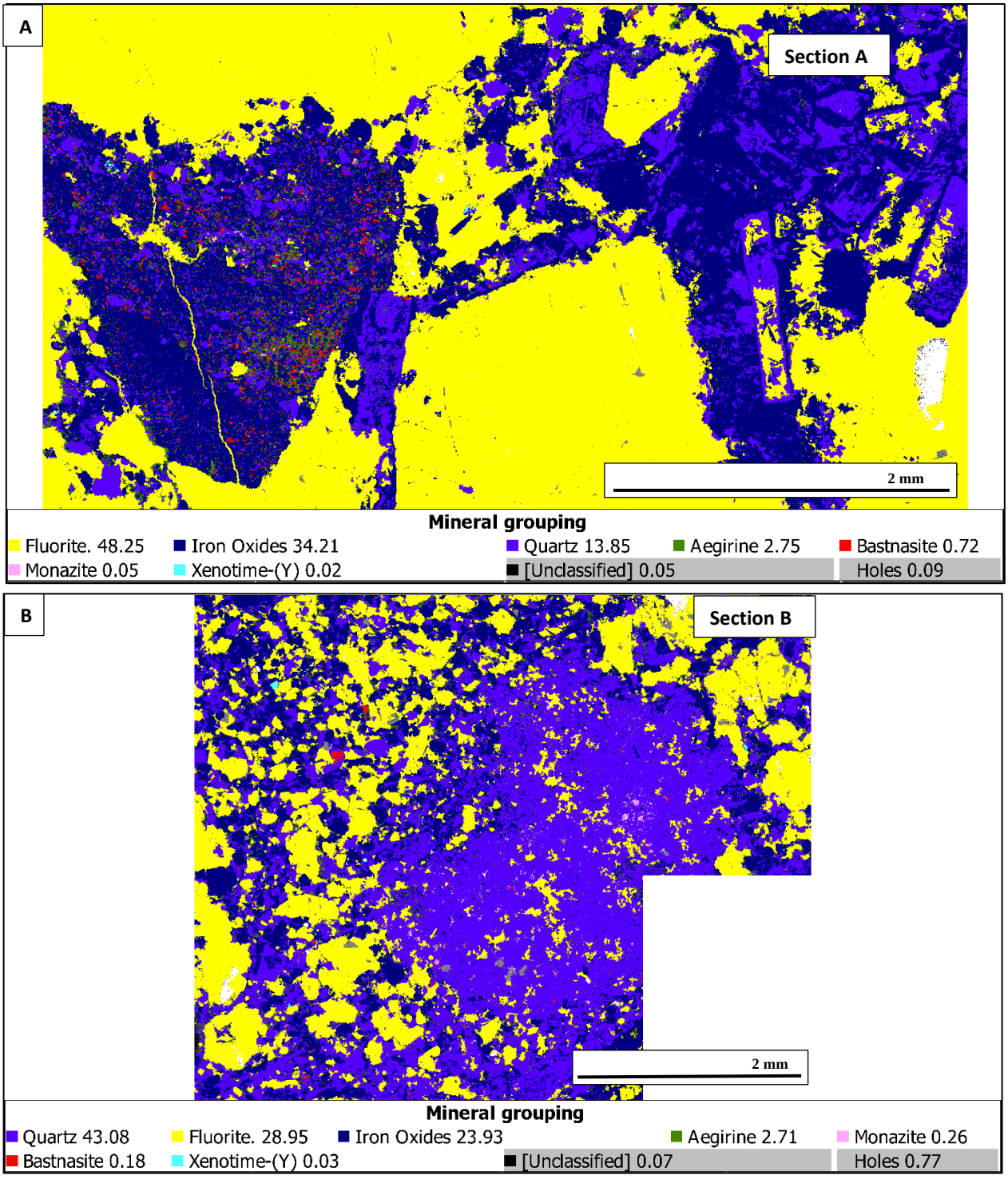

Figure 17. Mineral maps generated using TIMA, showing distribution of various minerals and their proportions (phase %) including quartz, fluorite, iron oxides, aegirine, bastnasite, monazite and xenotime. a) Section A in NK1A as depicted in figure 16a. b)Section B in NK1A as depicted in figure 16a.

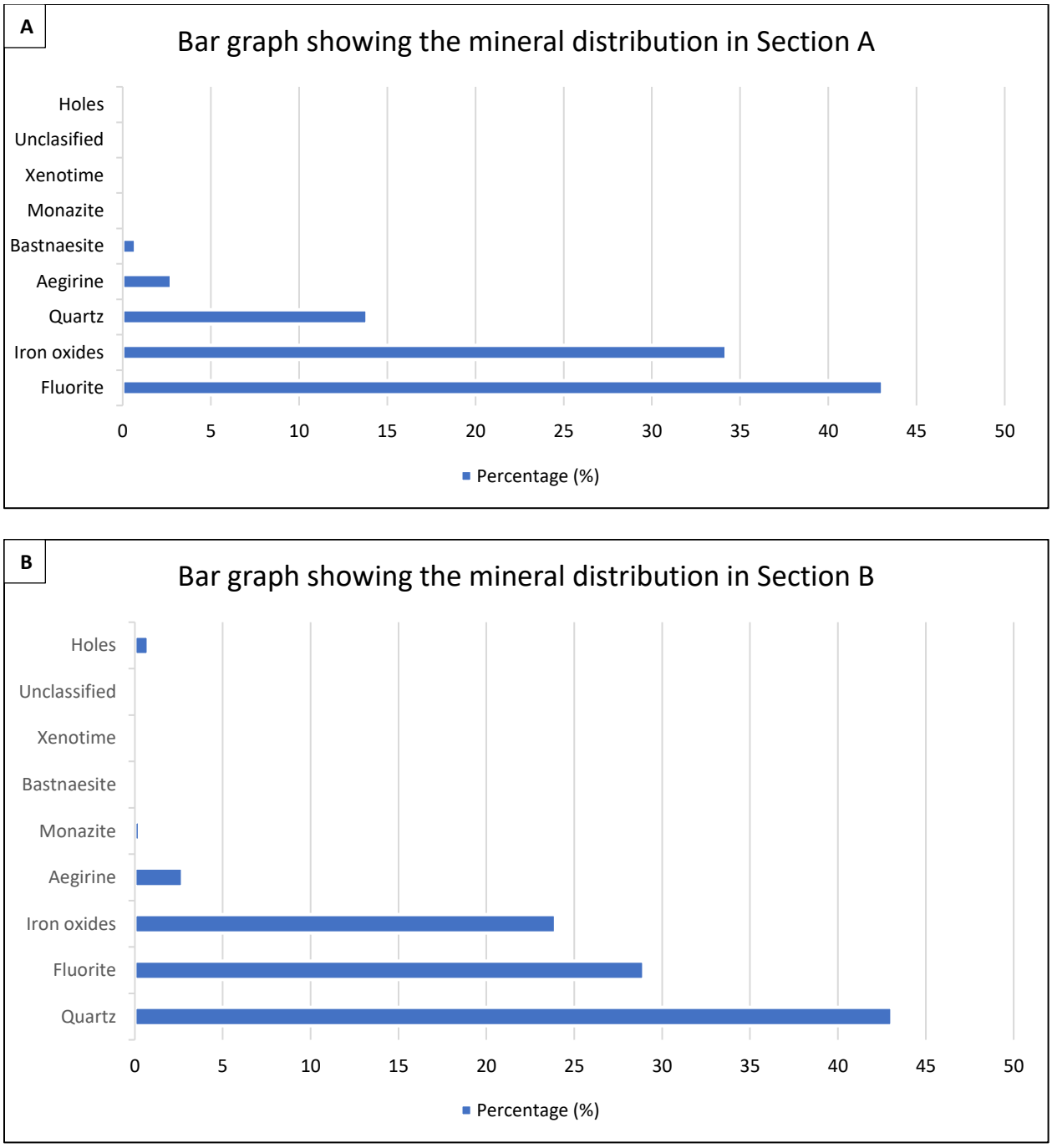

Figure 18. Bar graphs showing the mineral proportions (phase %) within the Nokeng hematite fluorite unit's NK1A sample. This data was sourced from the TIMA analysis. a)Section A of NK1A . b) Section B of NK1A.

6.1.2. REE minerals in Nokeng hematite-fluorite ore

Bastnasite

Mineral maps showing the distribution of bastnasite in NK1A are depicted in Figures 22a and b. Figure 22a displays an enrichment in bastnasite, which is concentrated in a 2 mm wide quartz-hematite fragment between the fluorite grains. Bastnasite is largely disseminated in both mineral maps, with varying grain sizes not exceeding 30 µm. The grains are subhedral to anhedral in shape, and are locked within various minerals including aegirine, goethite, hematite, quartz, fluorite, although some are not locked. Majority of the bastnasite is locked within goethite, fluorite and hematite (Tabel C.1, Appendix C). Figures 19a and b, also show that bastnasite is largely associated with quartz, goethite, aegirine and hematite.

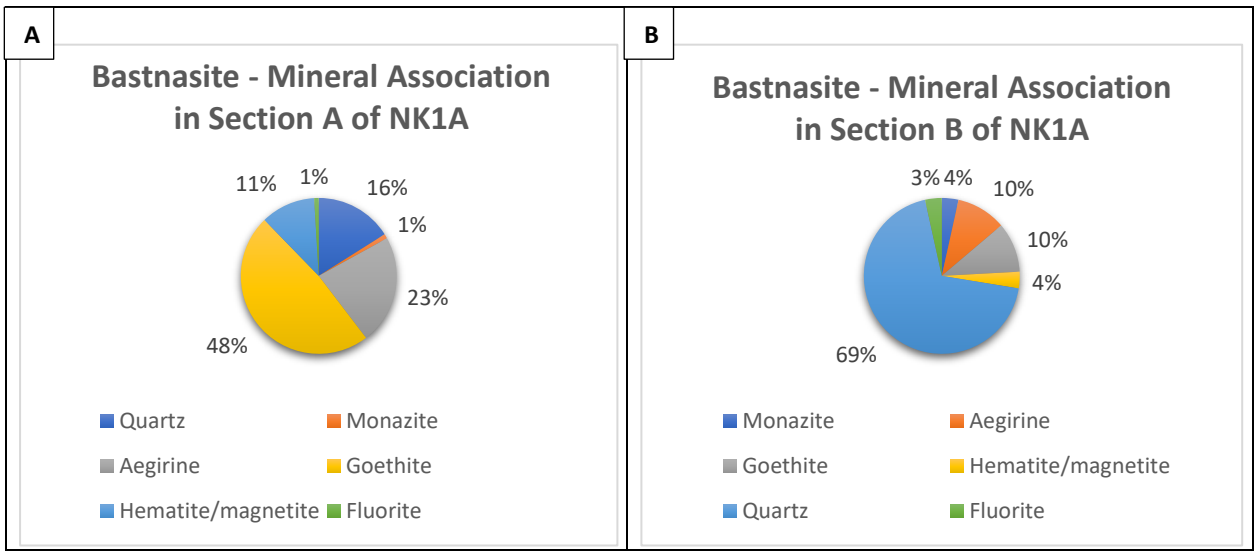

Figure 19. Pie charts showing the mineral association of bastnasite within the Nokeng hematite fluorite unit's NK1A sample. This data was sourced from the TIMA analysis. a) Section A of NK1A. b) Section B of NK1A.

Monazite

There is moderate concentrations of monazite in the hematite-fluorite unit (Figures 17, 22c and 20d). The monazite grains are disseminated and evidently concentrated in the quartz-rich parts of NK1A, especially in Figure 22d. The monazite grains generally possess subhedral to anhedral shapes (Figure 22c and d), and are locked within various minerals such as goethite, hematite, quartz, fluorite (Table C.2, Appendix C). Mineral association data for the Nokeng hematite fluorite ore shows that majority of monazite is associated with quartz, aegirine, goethite, hematite/magnetite and bastnasite (Figure 20a and b).

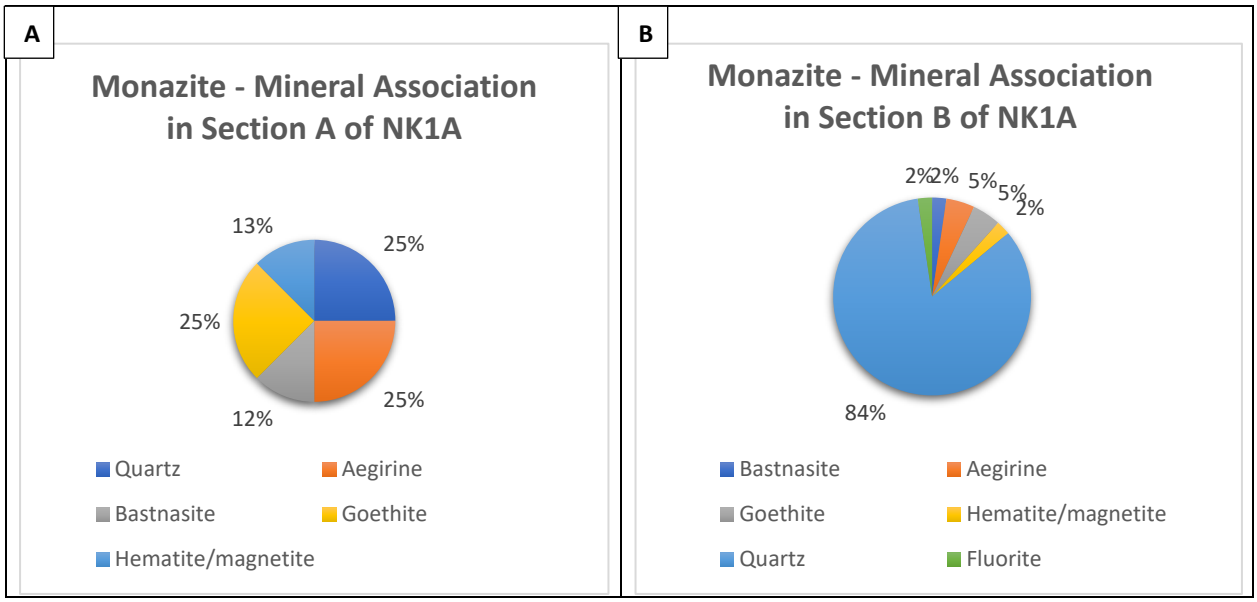

Figure 20. Pie charts showing the mineral association of monazite within the Nokeng hematite fluorite unit's NK1A sample. This data was sourced from the TIMA analysis. a) Section A in NK1A. b) Section B in NK1A.

Xenotime

Figures 22e and f display a relatively low abundance of xenotime within the hematite fluorite unit. Xenotime grains are disseminated and spread across the sample. The xenotime grains show subhedral to anhedral shapes. The TIMA mineral locking analysis shows that xenotime is variably locked within goethite and quartz, hematite, and fluorite (Table C.3, Appendix C). The mineral association data shows that xenotime is predominantly associated with quartz, goethite, hematite and aegirine (Figure 21a and b).

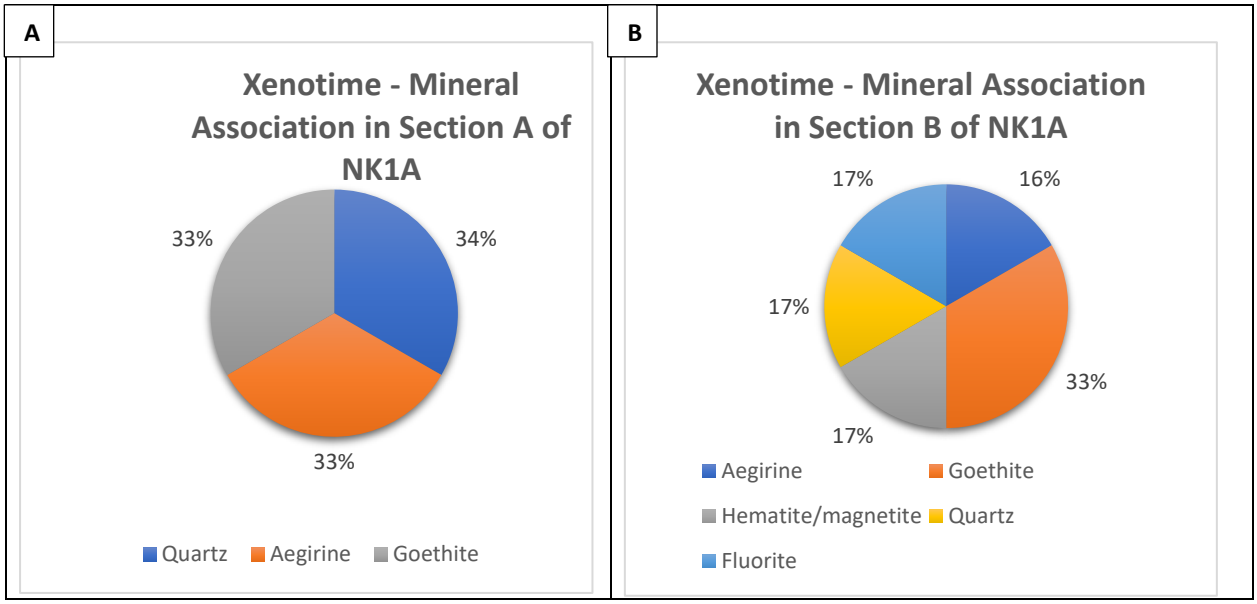

Figure 21. Pie charts showing the mineral association of xenotime within the Nokeng hematite fluorite unit's NK1A sample. This data was sourced from the TIMA analysis. a) Section A. b) Section B.

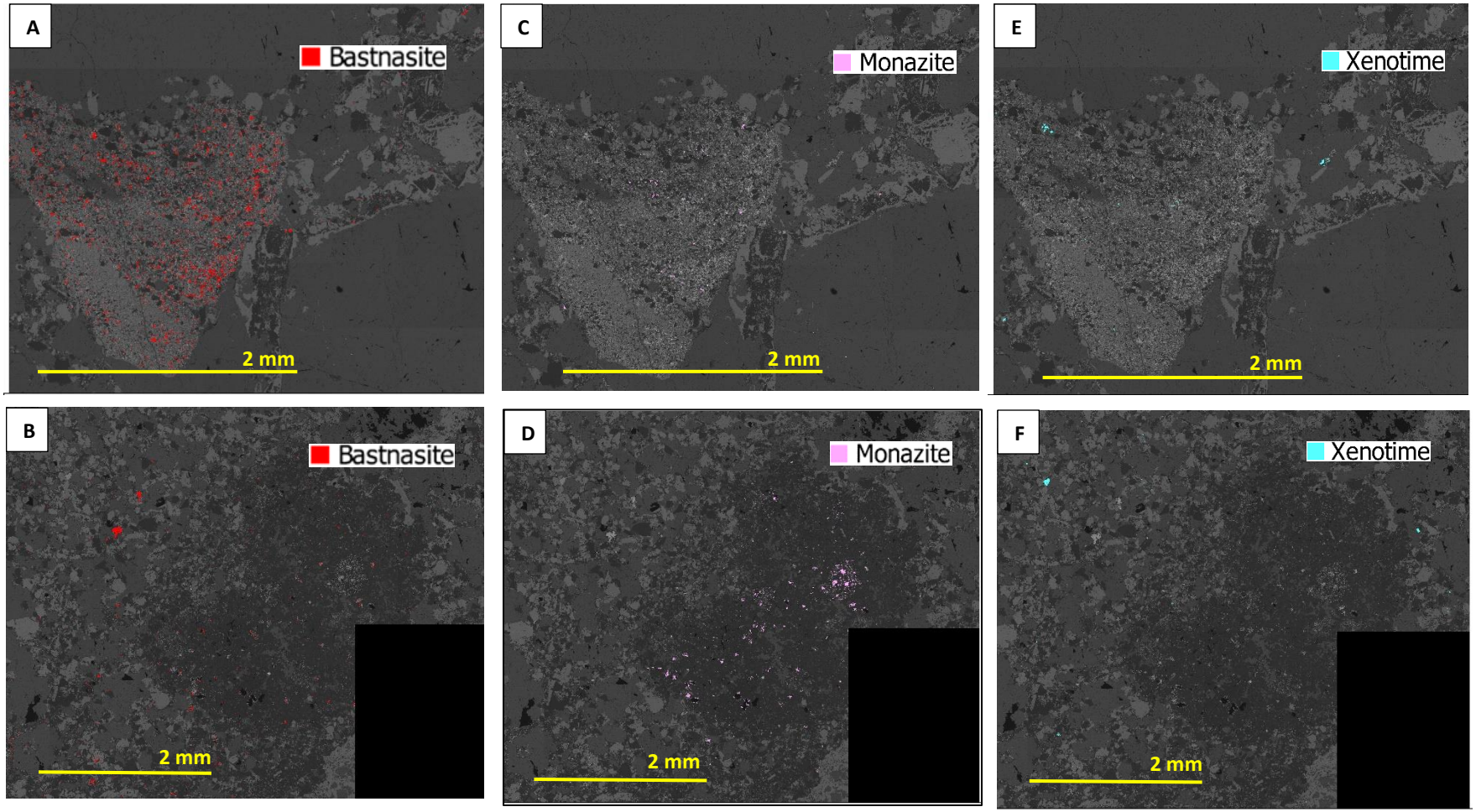

Figure 22. Mineral maps generated using the TIMA machine, showing the distribution of various REE minerals such as bastnasite (bst), monazite (mon) and xenotime (xen). a) Section A, distribution map of bst. b) Section B, distribution map of bst. c) Section A, distribution map of mon. d) Section B, distribution map of mon. e) Section A, distribution map of xen f) Section B, phase map of xen.

6.1.3. Element distribution maps for NK1A hematite-fluorite ore

Following the identification of REE bearing minerals within the hematite-fluorite unit, element maps were created to investigate where specific key trace elements contained within those mineral phases plot on the maps. Results reveal that the REE bearing mineral phases are variably enriched in REE elements. Bastnasite $(Ce,La,Y)CO_3F$ is mainly enriched in lanthanum, cerium, and yttrium. Monazite $(Ce,La,Nd,Th)(PO_4,SiO_4)$, which is an REE rich phosphate is particularly enriched in cerium, lanthanum, neodymium, and thorium. Lastly, xenotime (YPO_4), which is also a phosphate is particularly rich in yttrium.

This section of the study only focusses on the distribution of the major REEs associated with the REE bearing minerals. Firstly, the Y element map in Figure 23a shows a series of "hot-spots", which indicate a high concentration of the element in disseminated REE bearing minerals in Section A of NK1A. Yttrium tends to concentrate in the xenotime-rich portions of the map. An elemental deportment analysis shows that 100% of yttrium is contained within xenotime (Figure 23b). Tiny spots of the high Ce concentrations are also recorded within the same area (Figure 23c) on the left side of the map (Section A). Deportment results reveal that 94 mass % of Ce is contained within bastnasite, whereas 6 % is found in monazite (Figure 23d).

Other REE elements of interest include La and Nd. Figure 24a shows high La enrichments in the triangular hematite-quartz fragment on the left-hand side of the map (Section A), which is rich in bastnasite (Figures 17a and 22a). An elemental deportment analysis shows that 97 mass% of the element is contained within bastnasite, whereas 3 % is found in monazite (Figure 24b). Elevated amounts of Nd are also confined to the same fragment on the left-hand side of the element map (Figure 24c) although some rare hot-spots of La and Nd are also visible in the hematite-richer matrix on the right. Fluorite grains are essentially free of REE hot spots. The elemental deportment pie chart in Figure 24d shows that 100 % of Nd found in Section A is associated with monazite.

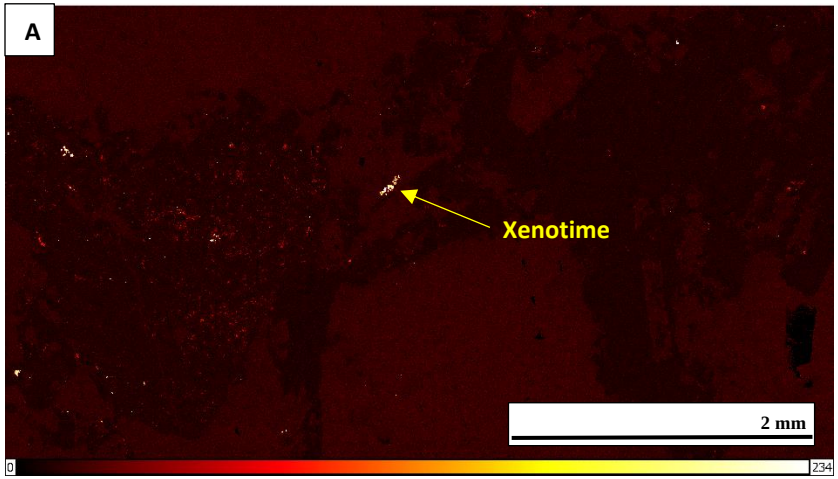

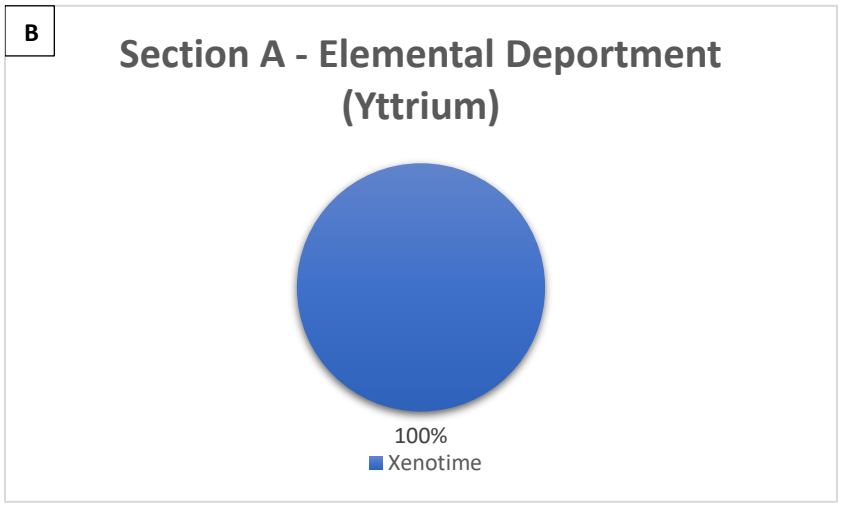

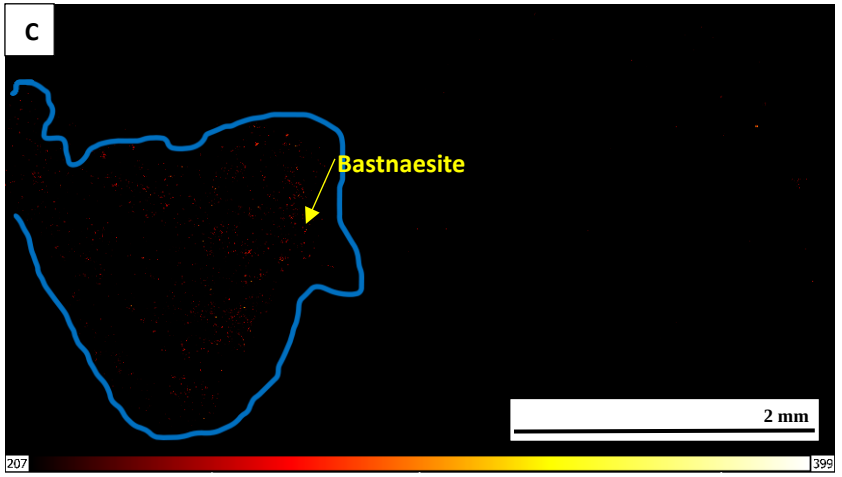

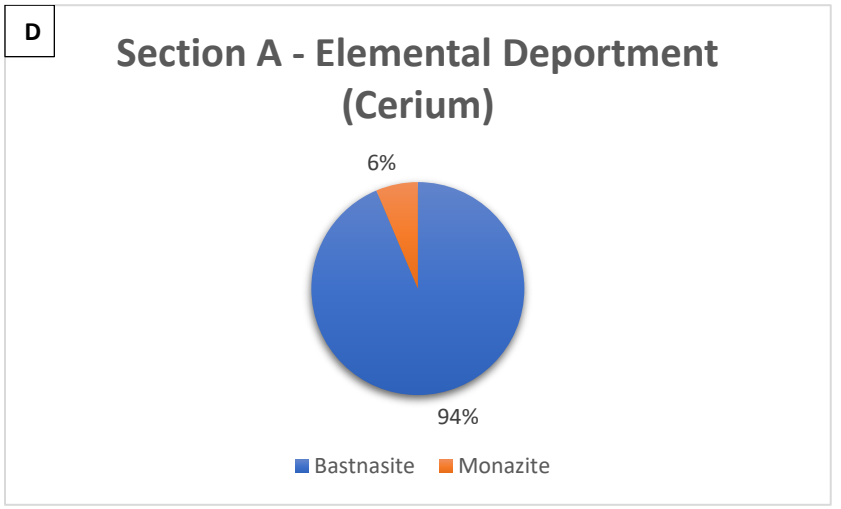

Figure 23. Element maps generated using a TIMA, showing the distribution of various elements including yttrium and cerium. The figure also displays an elemental deportment analysis for each element. a) This is an element map of yttrium for Section A. b) Elemental deportment analysis for yttrium in Section A. c) This is an element map of cerium for Section A. d) Elemental deportment analysis for yttrium in Section A.

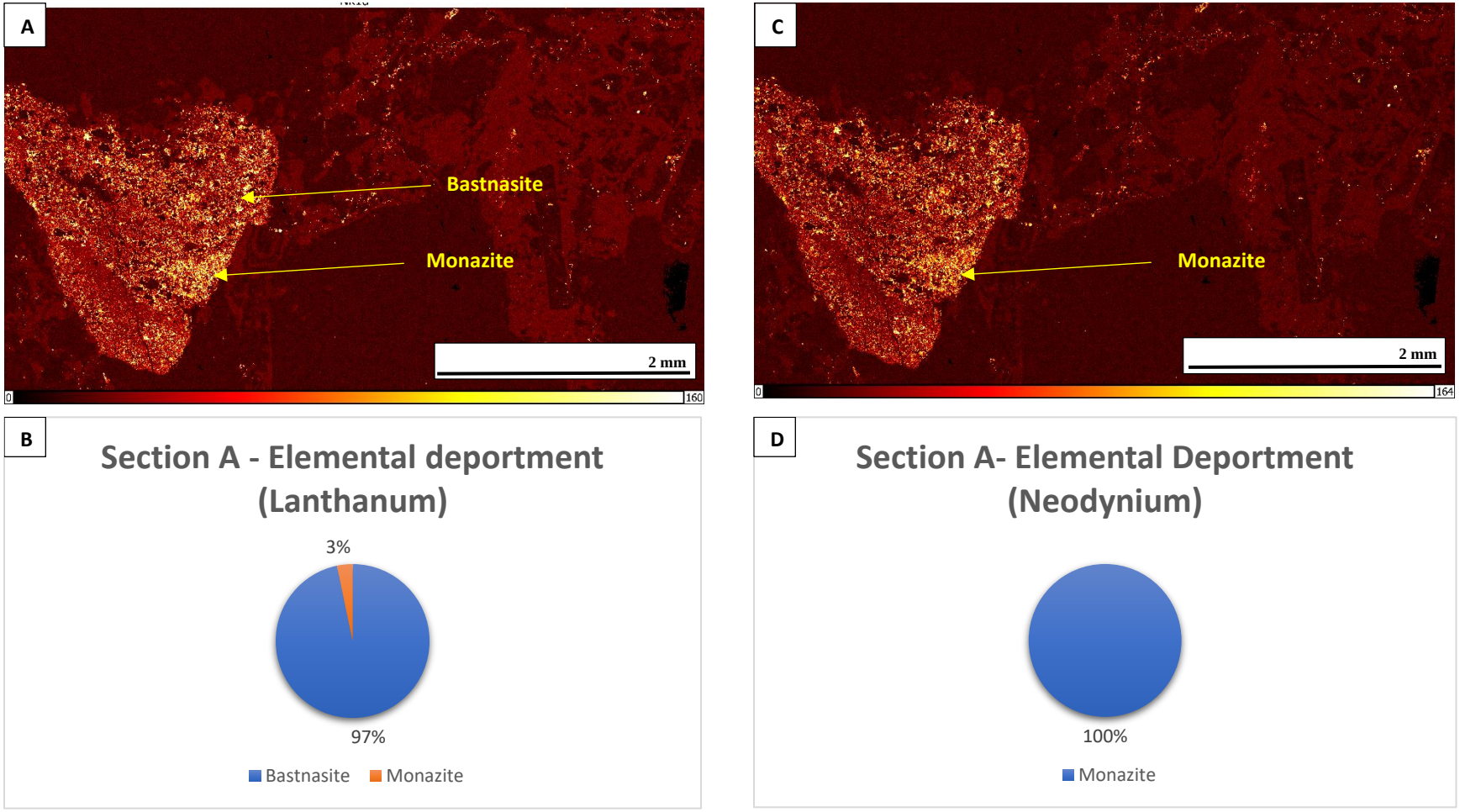

Figure 24. Element maps generated by TIMA, showing the distribution of La and Nd. The figure also shows an elemental deportment analysis for each element. a) Lanthanum distribution map for Section A. b) Elemental deportment analysis for La in Section A. c) Neodymium distribution map for Section A. d) Elemental deportment analysis for Nd in Section A.

6.1.4. Mineral proportions in Vergenoeg magnetite-fluorite ore

The TIMA analysis revealed the presence of several minerals, including fluorite, iron oxides and hydroxides (magnetite, hematite and goethite), quartz, aegirine and xenotime in sample VG1A (Figures 25a and b). It is evident that iron oxides and fluorite account for the largest mass % in the sample (Figures 26a and b).

Xenotime is sparsely distributed in the phase maps, with a higher abundance being recorded in section A at 0.09 %. Conversely, Section B displays lower abundance of xenotime accounting for 0.02 % of the total phase % in the area. There are about 2.99% and 0.08% of unclassified minerals in Sections A and B, respectively.

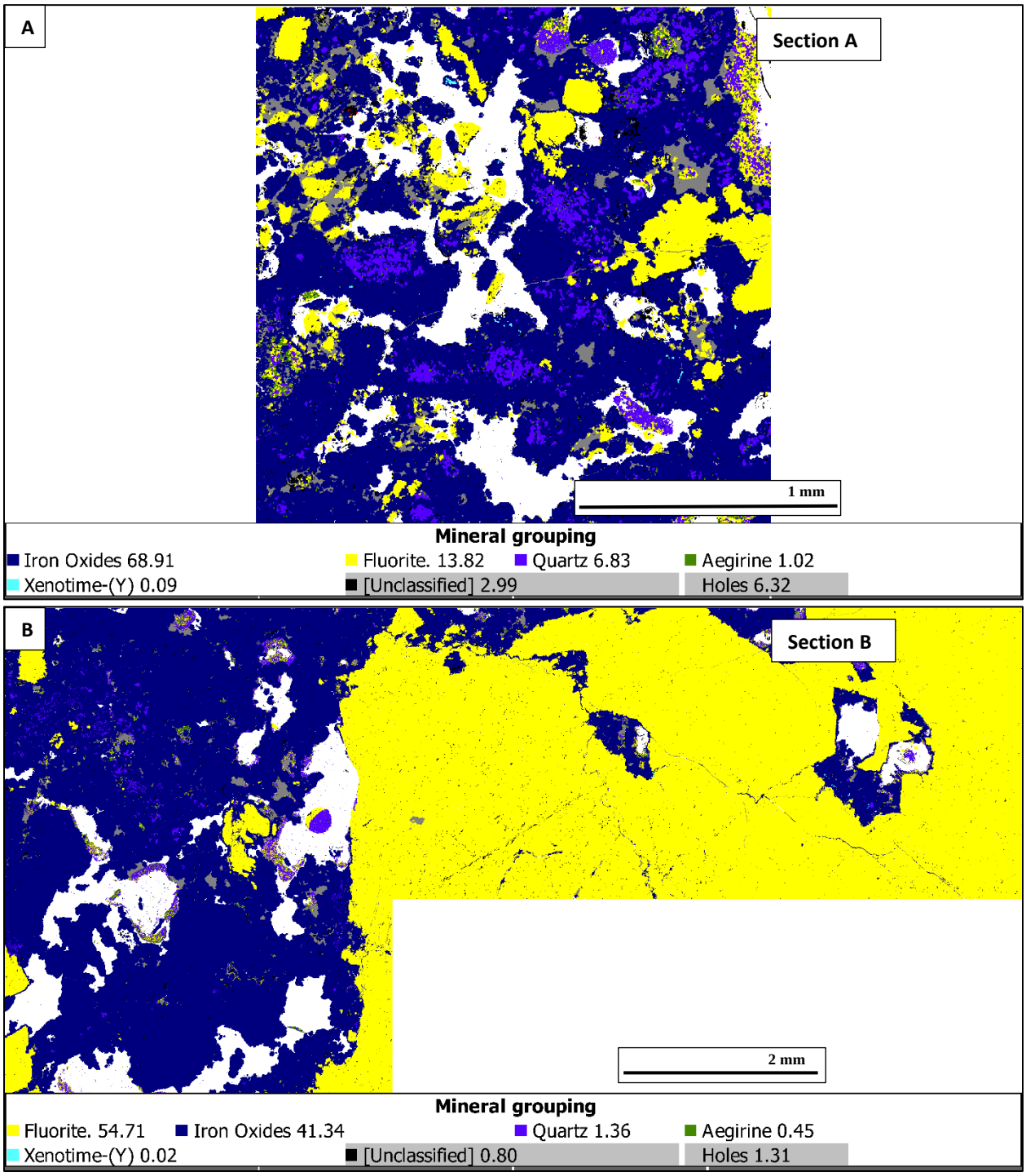

Figure 25. Mineral maps generated using TIMA, showing distribution of quartz, fluorite, iron oxides, aegirine and xenotime. A) Section A of VG1A as depicted in Figure 16b. b) Section A of VG1A as depicted in Figure 16b.

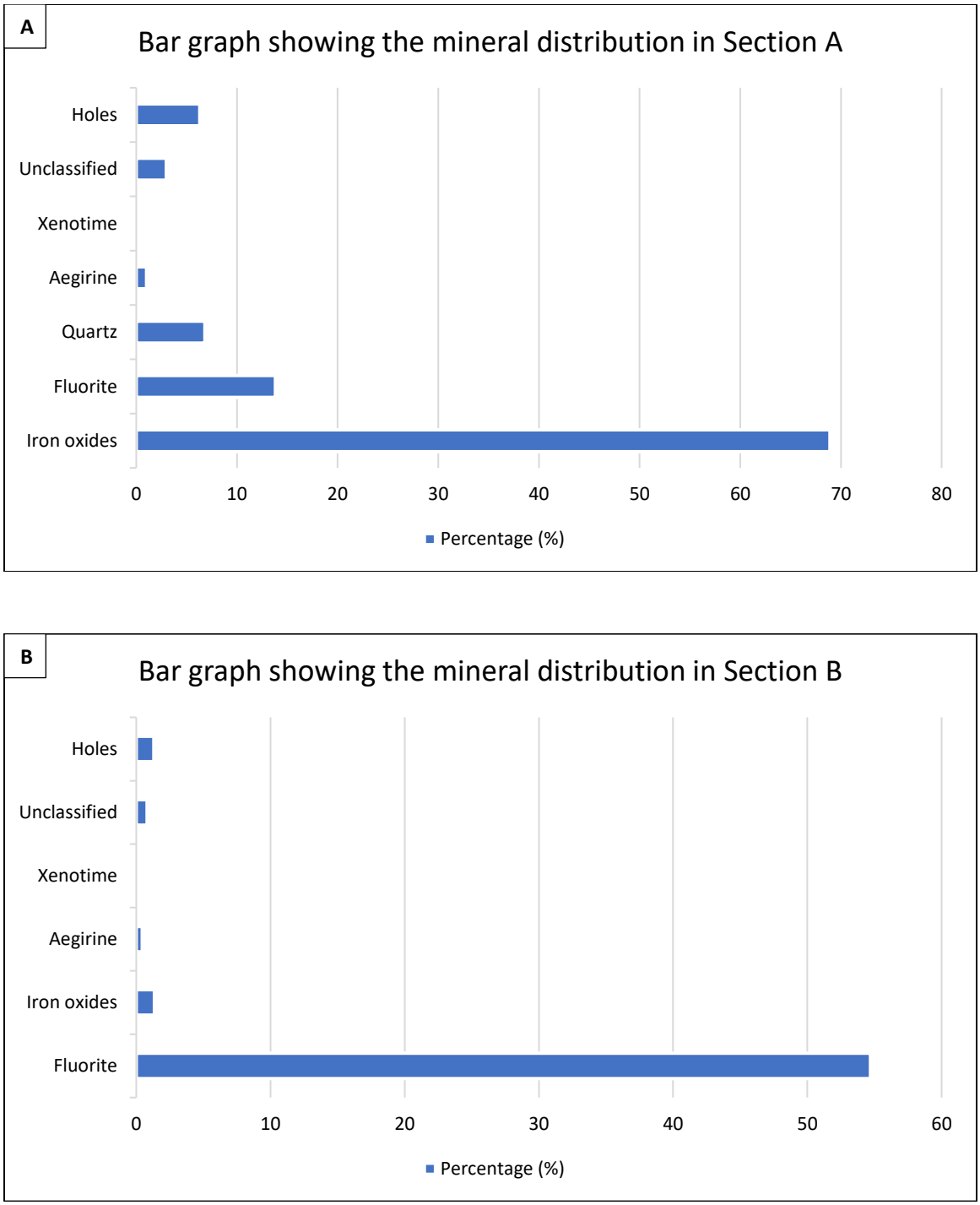

Figure 26. Bar graphs showing the mineral proportions (phase %) within the Vergenoeg magnetite fluorite unit's VG1A sample. This data was sourced from the TIMA analysis. a) Section A of sample VG1A. b) Section B of sample VG1A.

6.1.5. REE minerals in Vergenoeg magnetite-fluorite ore

Bastnasite

The REE mineral maps display small grains of bastnasite not exceeding 10 microns in size (Figure 29a and b). Four small bastnasite grains are evident in Figure 29a and one small grain can be seen in Figure 29a. The locations of the bastnasite grains in the two mineral maps are marked with a blue circle.

Monazite

The monazite content in Sections A and B is negligible. Only two micron-sized monazite grains were found in the mineral maps, and these grains are marked with blue circles in Figure 29c and D. This mineral is 100 % associated with hematite/magnetite (Figure 27).

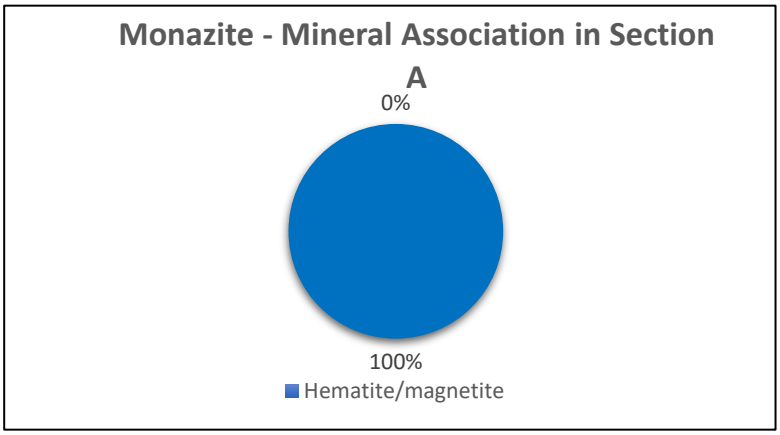

Figure 27. Pie charts showing the mineral association of monazite within the Vergenoeg magnetite fluorite unit's VG1A sample. This data represents section A of VG1A.

Xenotime

Xenotime reaches a maximum of 0.09 phase% in VG1A and it is represented by disseminated grains ≤ 20 µm in size (Figure 29e). The xenotime grains have generally subhedral to anhedral shapes. The highest content of xenotime is found in section A, locked within hematite/magnetite, goethite, and fluorite, with xenotime mass percentages of 50 %, 30 %, 10 %

locked within these minerals respectively (Table C.3, Appendix C). Xenotime in Section B is equally locked within hematite/magnetite and fluorite with a mass percentage of 33.3% locked in each mineral. The balance (33.3 mass %) is attributed to other minerals, which were unidentified by the TIMA analysis. Figure 28a and b show that xenotime is associated with goethite and hematite/magnetite.

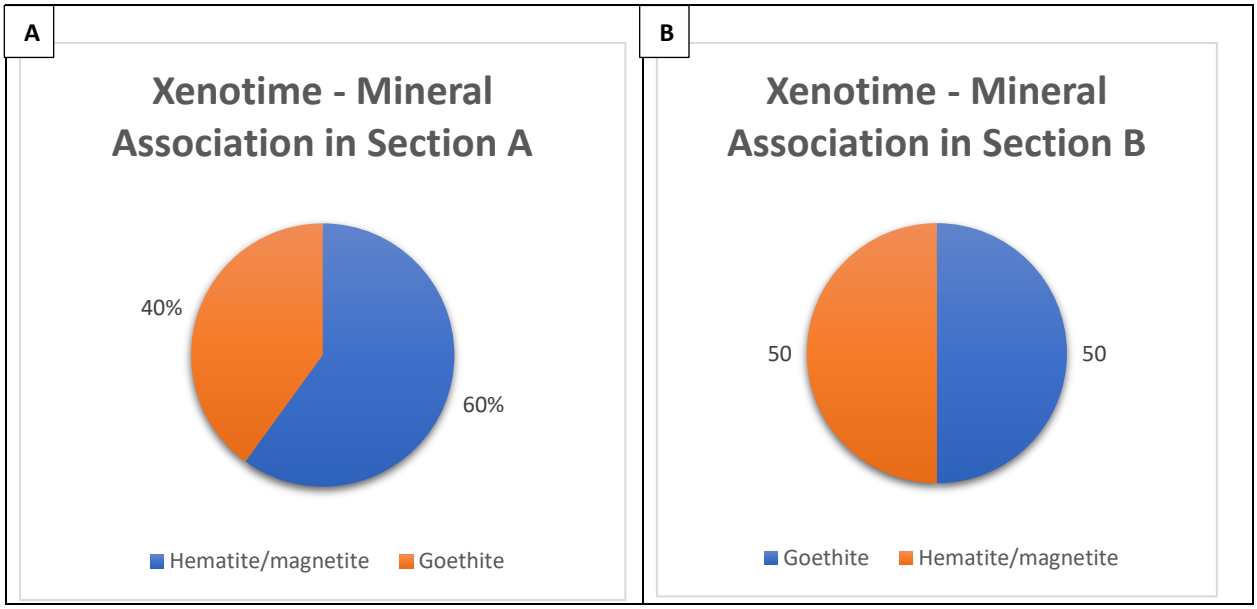

Figure 28. Pie charts showing the mineral association of xenotime within the Vergenoeg magnetite fluorite unit's NK1A sample. This data was sourced from the TIMA analysis. a) Section A of VG1A. b) Section B of VG1A.

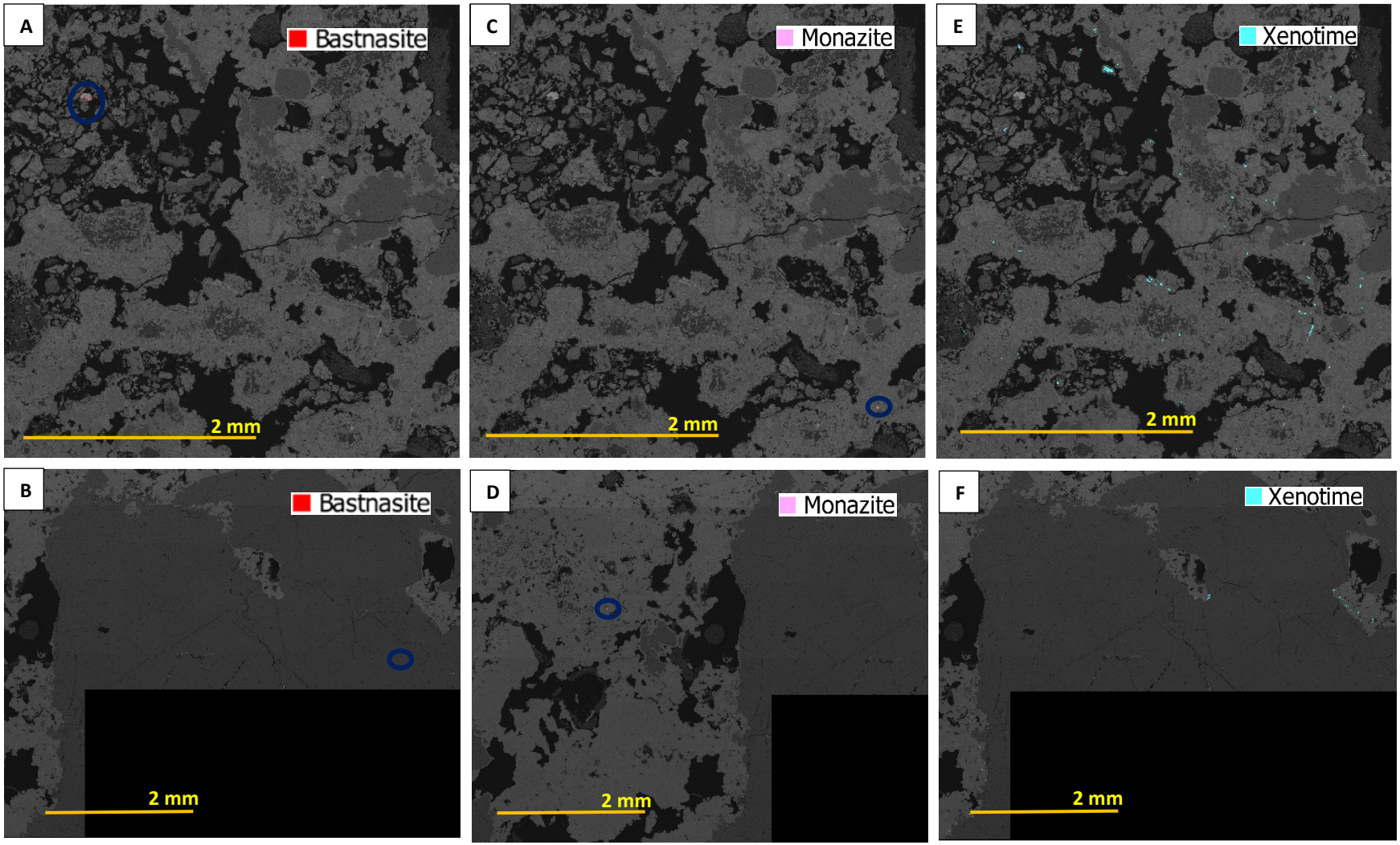

Figure 29. Mineral maps generated using the TIMA machine, showing the distribution of various REE rich minerals such as bastnasite (bst), monazite (mon) and xenotime (xen). a) Section A, distribution map of bst b) Section B, distribution of bst. C) Section A, distribution map of mon. D) Section B, distribution map of mon. E) Section A, distribution map of xen F) Section B, distribution map of xen.

6.1.6. Element distribution maps for the Vergenoeg magnetite-fluorite ore

Element maps were also created to elucidate the distribution of key REEs in the magnetite-fluorite ore. The element maps show relatively low abundances of Ce, La and Nd associated with the occurrences of bastnasite and monazite. Conversely, the element map in Figure 30a displays high Y peaks, which are associated with xenotime (YPO_4). The Y element is defined by a reddish to yellowish colour; and its hot-spots are disseminated and unevenly distributed throughout the element map. An elemental deportment analysis suggests that 100 mass% of the element is locked within xenotime (Figure 30b). An element map of cerium (Figure 30c) was also created to deduce how much of the element is contained in Section A. Results indicate significantly low concentrations of Ce with a single hot-spot highlighted by the blue circle in Figure 30c. An elemental deportment analysis reveals that 51 mass% of Ce is contained within monazite, whereas 49 mass% is found in bastnasite.

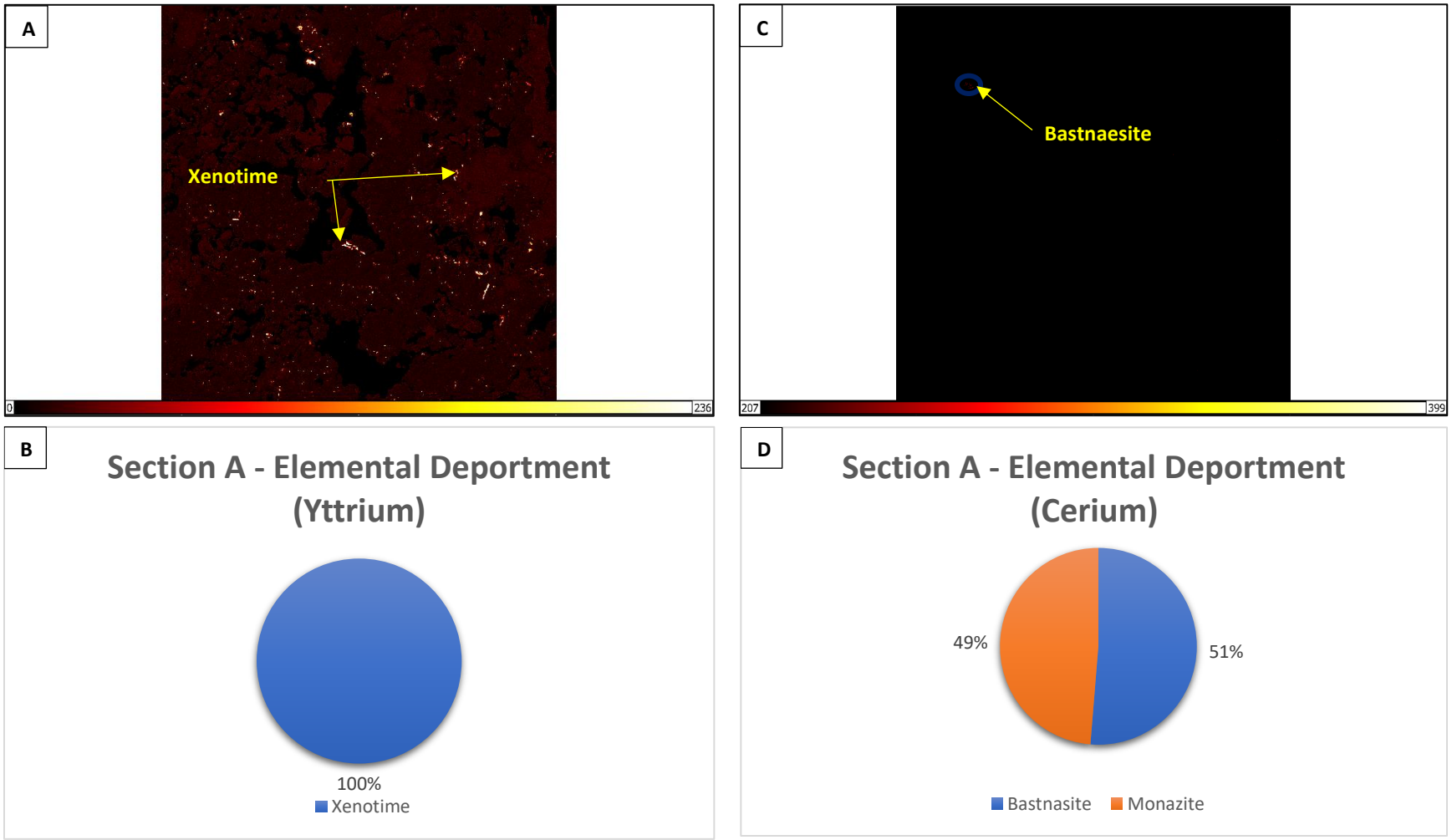

Figure 30. Element maps generated using a TIMA showing the distribution of Y and Ce. The figure also presents results of an elemental deportment analysis for each element. a) Element map of lanthanum for Section A. b) Elemental deportment results for lanthanum in Section A. c) Element map of neodymium for Section A. d) Elemental deportment results for neodymium in Section A.

6.2. Scanning electron microscope (SEM)

6.2.1. Hematite-fluorite unit

The TESCAN Vega SEM was used to analyse a polished section (NK2A) of Nokeng hematite-fluorite ore through backscattered electron imaging and energy-dispersive analysis. This machine was utilized for identifying accessory REE mineralization in the sample. Results reveal the presence of several accessory minerals including monazite and cassiterite. Figure 31a displays veinlets of BSE-bright monazite among coarse-grained fluorite. The fluorite grains are massive and possess a subhedral shape. Hematite and quartz occur as interstitial minerals filling the gaps between the larger fluorite grains and as veinlets along fractures in fluorite. Figure 31b displays cassiterite inclusions < 10 microns in size within anhedral hematite grain. The cassiterite is also anhedral and can be distinguished by the brightest BSE contrast. The hematite grain is surrounded by a matrix of quartz with uneven corroded boundaries. At the contact between quartz and hematite, anhedral to amorphous or colloform monazite occurs as dispersed grains that are a few microns in size.

A zoned zircon grain slightly bigger than 20 µm in size with a distinct and roughly euhedral shape is shown in Figure 31c. The zircon is distinguished from other minerals by its crystal morphology and BSE-bright-whitish colour. It is surrounded by BSE-darker hematite and quartz, which occur as interstitial minerals, between large fluorite grains with an intermediate BSE colour. Fluorite and quartz display subhedral to anhedral shapes and occur in variable sizes whereas hematite forms thin specularitic needles and coarser platelets. Figure 31c also includes an anhedral grain of monazite around 20 µm in size. The BSE-brightest porous monazite is locked between quartz grains and hematite. Lastly, Figure 31d depicts inclusions of monazite surrounded by sericite. The monazite grains around 10 µm in size are characterised by a BSE bright colour and a subhedral to anhedral morphology. Sericite is BSE-dark and fills interstitial space between fluorite and hematite. The hematite and fluorite form larger BSE-grey and BSE-light-grey crystals over 150 µm.

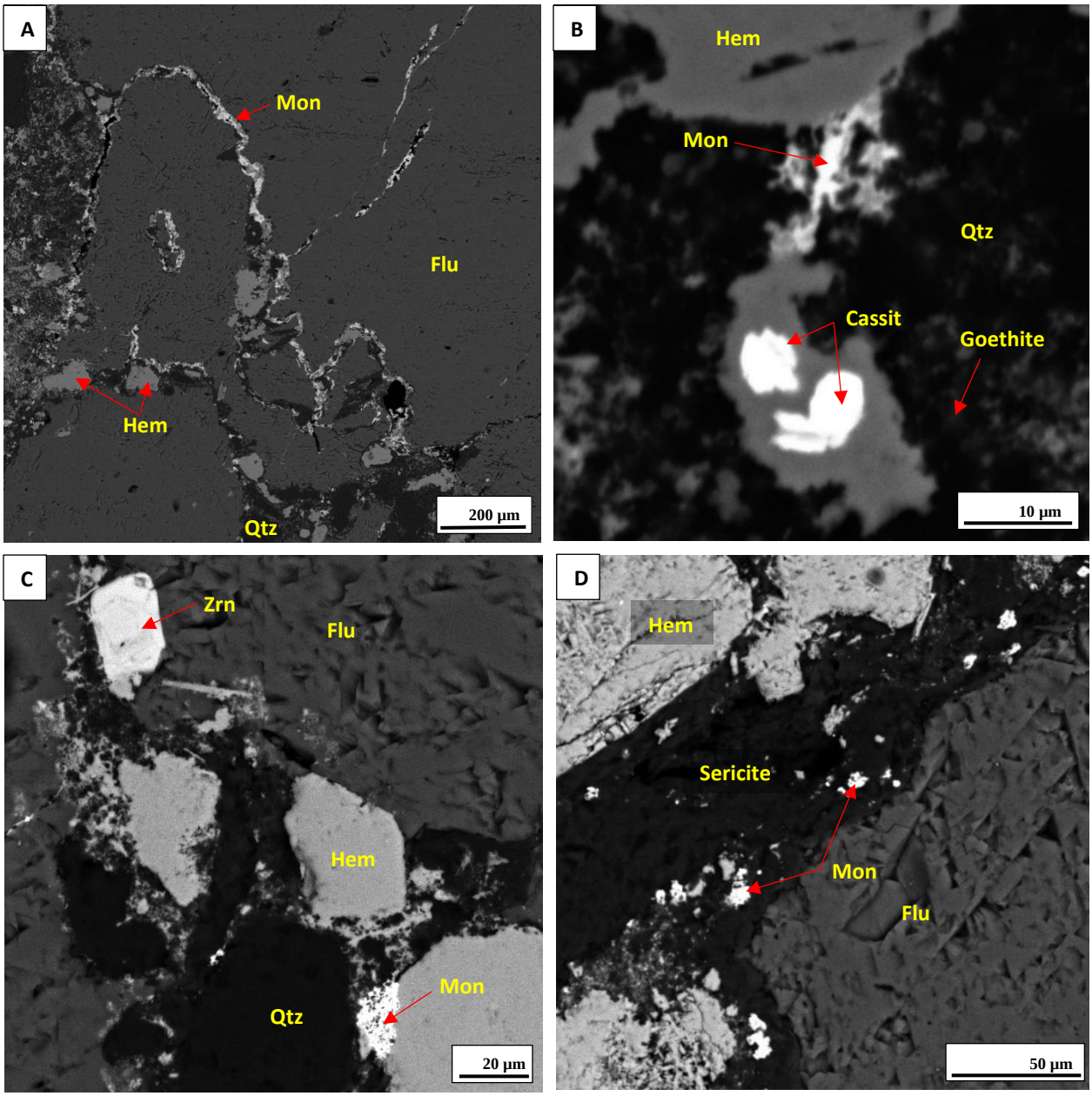

Figure 31. BSE images of hematite fluorite ore (NK2A). a) Mon in veins amongst flu, hem and qtz. b) Mon and Cassit within qtz, goethite and hem. c) Zrn and mon amongst qtz, hem and flu. d) Mon in sericite between flu and hem. Abbr.: flu-fluorite; hem-hematite; mon-monazite; qtz-quartz; cassit-cassiterite; zrn-zircon.

6.2.2. Nokeng rhyolitic breccia

The SEM was also used to better understand the mineralogical composition of the breccia unit. A polished thin section of sample NK4B was selected as a representative sample of the rhyolitic breccia. Figure 32a displays several monazite crystals distinguished from the other minerals by their BSE-bright colour. The size of the crystals ranges from 10 to 30 µm. Monazite mostly occurs in spaces between the fluorite and hematite grains, however there are some grains that occur intermittently as inclusion in fluorite and hematite. Monazite grains are also observed surrounded completely by quartz, which is generally pervasive and surrounds all the grains in the area (Figure 32a). Larger porous monazite grains can be observed in Figure 32b, where they are overgrown by hematite grains surrounded by massive quartz grains. The monazite again possesses a BSE-bright colour, with grain sizes ranging between 10 µm and 40 µm.

The volcanic nature of the fragments in the breccia unit is well depicted in Figures 32c and 32d. Quartz needles up to 500-600 µm long occur as discrete crystal and their aggregates (Figure 32c) Interstitial hematite fills the spaces between the quartz needles, likely replacing the matrix of devitrified glass. Quartz is characterised by a BSE-black colour whereas hematite shows a BSE-grey colour. Figure 32d also displays chlorite pseudomorphs after feldspar phenocrysts, which had a morphology of elongated laths up to 400 µm long. The chlorite grains display a BSE-greyish colour, and they are surrounded by BSE-whitish-grey hematite, which likely replaced volcanic glass.

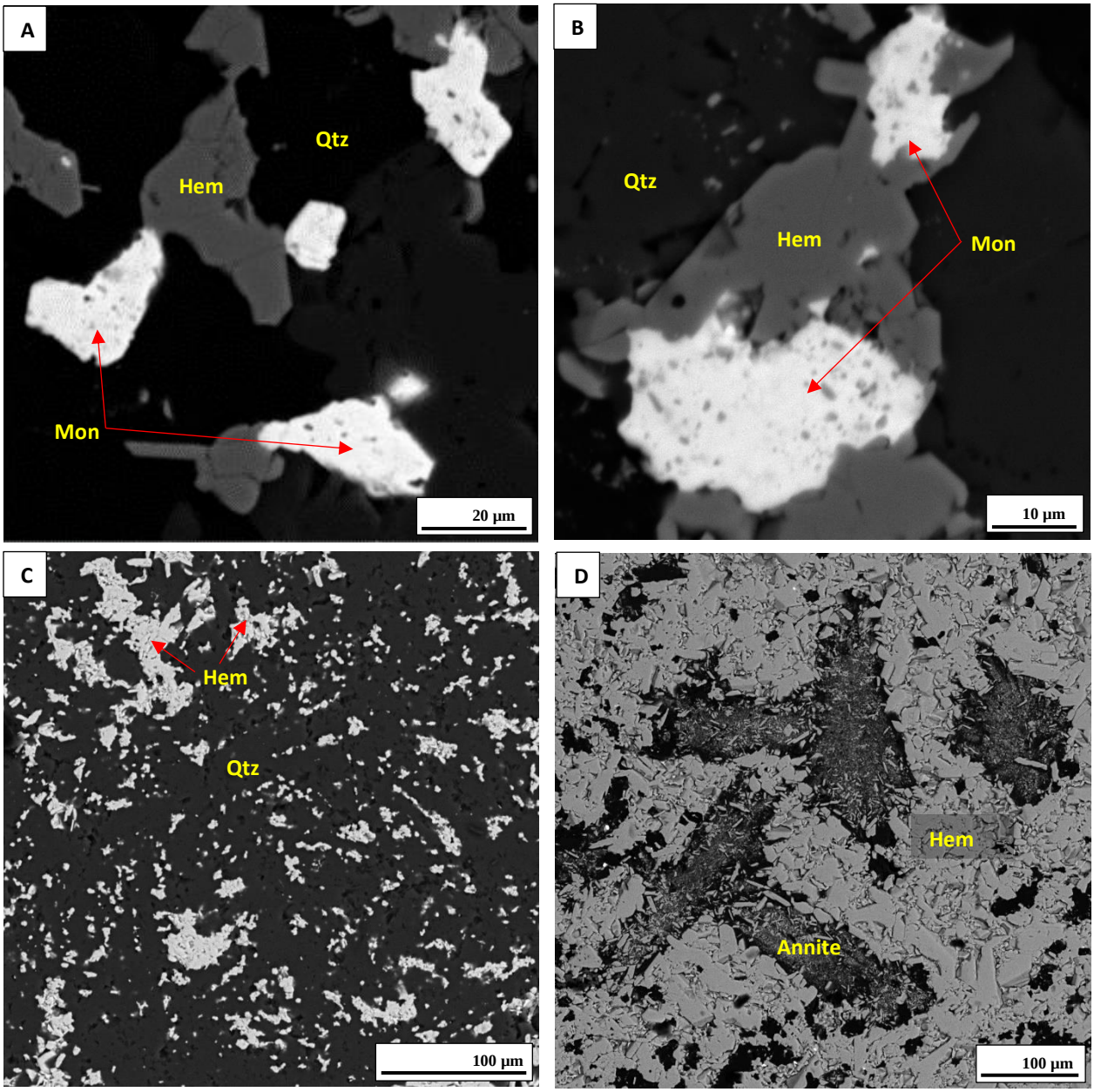

Figure 32. BSE images of rhyolitic breccia (NK4B). a) Mon among hem, flu and qtz. b) Mon in Hem amongst qtz. c) Qtz needles after tridymite with interstitial hem. d) chlorite pseudomorphs after fs among hem. Abbr.: flu-fluorite; hem-hematite; mon-monazite; qtz-quartz; fs-feldspar.

Chapter 7: Discussion

This section of the study aims to discuss the geology found at the Nokeng Fluorite Mine's Plattekop deposit. The results gathered from microscopy, TIMA, SEM, ICP-MS and XRF in chapter 4, 5 and 6 will be analysed and compared to the findings of Fourie (2000) and Crocker (1985), who briefly touched on the character of Nokeng rocks. This will be followed by a comparative analysis of the Plattekop deposit versus the Vergenoeg deposit. This comparison aims to decipher whether the Plattekop deposit is the distal facies of the Vergenoeg volcanic pipe.

REEs form the basis of this research, and their distribution and host mineral phases (e.g., monazite, bastnasite, and xenotime) will be discussed in depth. The REE occurrences in the Plattekop, quantity, size, mineral association, mineral locking, and elemental deportment will be explored. This will then be followed by a comparative analysis of the REEs found in Nokeng and those reported within the Vergenoeg pipe by various researchers (e.g., Brandt et al., 2019 and Graupner et al., 2015). Lastly, preliminary estimations will be conducted to deduce if the REE mineralization found in Nokeng and Vergenoeg is economically significant.

7.1 Geological setting of the Plattekop deposit

7.1.1 Main lithologies and ore types of Nokeng's Plattekop deposit

The upper portion of the Plattekop deposit comprises the hematite-fluorite unit, which is characterised by a predominance of iron oxides (55 mod.%) along with fluorite (30 mod.%) and quartz (15 mod.%). The iron oxides within this unit are mainly composed of hematite and goethite, with no primary magnetite being found in the samples. The petrographic study shows two varieties/generations of fluorite in the ore. The first variety is coarse-grained, well-defined subhedral crystals of fluorite with distinct growth patterns (Figure 10e) and sizes of around 1000 µm and bigger. Conversely, there is a second generation of fluorite grains with anhedral shapes and texture. The second generation possesses variable grain sizes from crystals that are >500 µm to smaller grains (<500 µm), which form the matrix together with hematite in Figure 10c. This suggests that there are both primary and secondary fluorite grains within the unit, with the primary crystals forming under near-magmatic temperatures and pressures, whereas the secondary fluorite grains likely formed from hydrothermal fluids, partly due to alteration, dissolution and reprecipitation of pre-existing fluorite-bearing rocks. This secondary fluorite is related to

mineralisation of REEs (e.g., monazite is found between secondary fluorite grains in figure 31a). Quartz also occurs interstitially between the fluorite grains (Figure 10c); its crystals lack well-defined faces, which suggests that they formed later in the mineral assemblage. Furthermore, the quartz grain sizes of <100 µm are remarkably small, alluding to rapid crystallisation. Hematite mostly encloses fluorite and quartz; however, it also occurs as an inclusion within fluorite (figure 10d). There are three varieties of iron oxides and hydroxides found within the hematite-fluorite unit, which include: 1) hematite pseudomorphs after magnetite, displayed in Figure 10d; 2) specularitic elongated needles; massive hematite replacing rock fragments, silicates, and filling cavities (Figure 10e); 3) hydrohematite and goethite are late low-temperature products of hematite hydration and alteration (Figure C.1 to C.4, Appendix C). Although NK1A, NK2A, and NK3C possess similar mineralogy, the texture and degree of alteration occurring within these splits varies. NK1A and NK3C display a porphyritic texture, whereas NK2A shows a more phaneritic texture. NK2A shows a replacement of silicates by hematite in Figure 10e, and in contrast NK3A displays the replacement of magnetite by hematite. Moreover, NK2A has sedimentary structures (bedding) and flow banding, which is not observed in the other two samples. This is indicative of heterogeneity within the unit.

Crocker (1985) refers to this unit as the fluorite-hematite froth-flow channel lag ore deposit that forms a part of the concordant intrapyroclastic orebodies within the Vergenoeg Rock Suite. These sub-concordant orebodies are delineated as spillover remnants of pyroclastics and lava (Fourie, 2000). Similarly to our study, Fourie (2000) alluded to iron oxides (50 %), fluorite (40 %) and quartz (10 %) being the dominant minerals within Plattekop.The Nokeng breccia belongs to the ignimbrite unit, which constitutes the lower portion of the Plattekop deposit and underlies the hematite-fluorite unit. In hand specimens (Figures 11a, b), the clast-supported breccia is dominated by rhyolitic lava and tuff material (60 mod.%), specularitic and massive hematite (30 mod.%) and fluorite (10 mod.%). The rhyolitic lava fragments are more than 5 cm in size, whereas tuffaceous fragments are about 1 cm, and they both have a reddish brownish colour due to dispersed iron oxides. Crocker (1985) categorised the basal ignimbrites within the Vergenoeg Pyroclastic Rock Suite into four units including 1) fines-depleted lag agglomerate, 2) fines-enriched ash-fall tuff; 3) froth-flow channel lag deposit, 4) fines-enriched black glass tuff (Table 5). The Nokeng breccia (NK4) belongs to fines-depleted lag agglomerate or breccia, which may form a basal layer of the ignimbritic flow. The fines-depleted eruptive breccia is distinguished by

the large size of the rhyolite fragments (Figure 11b), minor proportion of tuffaceous material, limited occurrence of flow textures, absence of ash-fall vitric lapilli and vitric fiamme textured particles. This evidences the similarities between NK4 and the agglomerate described by Crocker (1985), which also lacks pronounced density stratification or bedding textures. The volcanic nature of the rhyolitic fragments (Figures 11a-f) is supported by the occurrence of quartz, volcanic glass textures, spherulitic aggregates as well as the relics of feldspar phenocrysts. These volcanic textures are significantly replaced or obliterated by hematite replacement in the tuffaceous matrix and smaller fragments of the breccia. Conversely, these textures are more preserved in the internal parts of the larger fragments within the breccia.

Table 5. Rock units of the Vergenoeg Volcanogenic Province, Crocker (1985)

Vergenoeg Volcanogenic Province
Vergenoeg Pyroclastic rock suite
(7) Banded iron-formation
(6) Placer outwash fan delta conglomerate
(5) Breccia agglomerate
Basal ignimbrites
(4) Fines-enriched black grass tuff
(3) Froth-flow channel lag deposit
(2) Fines-enriched ash-fall tuff
(1) Fines-depleted lag agglomerate
Vergenoeg discordant breccia pipe
Oxidised fluorite-hematite-goethite gossan
Unoxidized fluorite-magnetite-siderite-grunerite breccia pipe ore

Although Crocker (1985) grouped the Plattekop and the lag agglomerate or breccia into basal ignimbrites (Table 5), for this study, they are analysed as separate units. The fluorite grades and the economic values of the two units vary greatly, which warrants an individual analysis of the rock units. According to Giordano and Cas (2021), ignimbrites are rocks composed of pumice

and ash through to scoria that precipitate from ash-rich pyroclastic density currents, irrespective of their composition (from rhyolite to basaltic) and crystal content (aphyric to more than 50 % by volume). It is evident that the fluorite-hematite unit is not dominated by pumice, ash, scoria, or any ash-rich pyroclasts, which is contrary to the definition of Giordano and Cas (2021). In contrast, the Nokeng breccia is a basal lithofacies of a stratified ignimbrite flow. Moreover, these two studied Nokeng rock types greatly contrast in texture and mineralogy. The eruptive breccia (Figure 32a) shows needle-like quartz, porphyritic and spherulitic textures which, are absent in the hematite-fluorite unit. Furthermore, the Nokeng breccia (Figure 32d) possesses minerals such as chlorite pseudomorphs after feldspar, which are absent in the hematite-fluorite. Likewise, the hematite-fluorite unit possesses minerals such as sericite (Figure 31d) and aegirine, which are not found in the basal breccias.

7.1.2 Geochemical character of Nokeng's Plattekop deposit

Ores of the hematite-fluorite unit, including NK1, NK2 and NK3, reveal a significant disparity in SiO_2 content, with NK2 revealing the highest average SiO_2 content (32.9 wt.%), followed by NK1 with a value of 11.7 wt.% and, lastly, NK3A showed negligible concentrations of SiO_2 with an average 0.32 wt.%. The geochemical results also show that ores depleted in SiO_2 (e.g., NK3A) possess higher CaO and FeO^t, and in contrast, rocks with higher concentrations of SiO_2 (e.g., NK2A) possess lower CaO and FeO^t (Figure 35). This is also supported by the negative relationship between SiO_2 and CaO depicted by the plot in Figure 13a. Crocker (1985) suggested that the Plattekop marks an abrupt change from silicic to iron-rich carbonate volcanism, assuming that the rocks with the higher silica content were formed during the initial stages of rhyolitic volcanism, whereas those with higher CaO and F content formed at the late stages. This is partly consistent with the model by Hou et al. (2013) who showed that Si-rich and Fe-rich lithologies formed by crystallization of two immiscible liquids although the composition of the experimental liquids did not match the natural compositions exactly. Another theory envisages that the high CaO content is attributed to hydrothermal activities within the deposit, where fluorite (CaF_2) was precipitated from Ca and Fe-rich rocks depleted in SiO_2. Furthermore, Scherhag (1990) suggested that hydrothermal processes at the final stages of volcanism could have resulted in the mobilisation of fluorite and subsequent precipitation in the hanging wall regions of the volcanic pipe and the

associated flow deposits. This, therefore, supports an idea that, the variation in CaO content could also be due to hydrothermal circulation, given its prominence within the Vergenoeg Rock Suite.

HFSEs such as Nb and Ta are generally immobile and resistant to hydrothermal influence due to their tendency to form strong ionic bonds with oxygen (Li et al., 2022). However, the distribution of the HFSEs are susceptible to the influence of F-rich hydrothermal fluids (Li et al., 2022). It is evident from figures 33a - c that the Nb/Ta ratios for the Vergenoeg magnetite fluorite and Nokeng breccia is relatively low compared to the Nokeng hematite-fluorite ore. According to Ballouard et al. (2016), a decrease in the Nb/Ta ratio is indicative of hydrothermal alteration. This is due to the higher mobility of Ta compared to Nb in F-rich hydrothermal fluids (Ballouard et al., 2016), which leads to an enrichment in Nb (Chevychelov et al. (2005). This is supported by Figure 33c and d which show a high enrichment of Nb and reduced concentrations of Ta in all studied samples. Figure 33a and b display a negative shallow dipping trend for the Nokeng hematite fluorite samples. This negative trend coupled with the relatively elevated Nb/Ta ratio is indicative of minimal hydrothermal alteration in the unit. Furthermore, the use of highly immobile elements such as Zr/Hf and Sr in Figures 33a and b respectively, aided in testing for the hydrothermal influence. These elements similarly to Nb and Ta are generally stable in most geological settings, therefore any variation in their concentrations is often indicative of hydrothermal alteration. However, these theories are largely feasible for conventional magmatic rock types (e.g., peraluminous granites studied by Ballouard et al. (2016)). Therefore, for unconventional rock types such as the Plattekop stratified pyroclastic deposit; they must not be used Sensu Stricto.

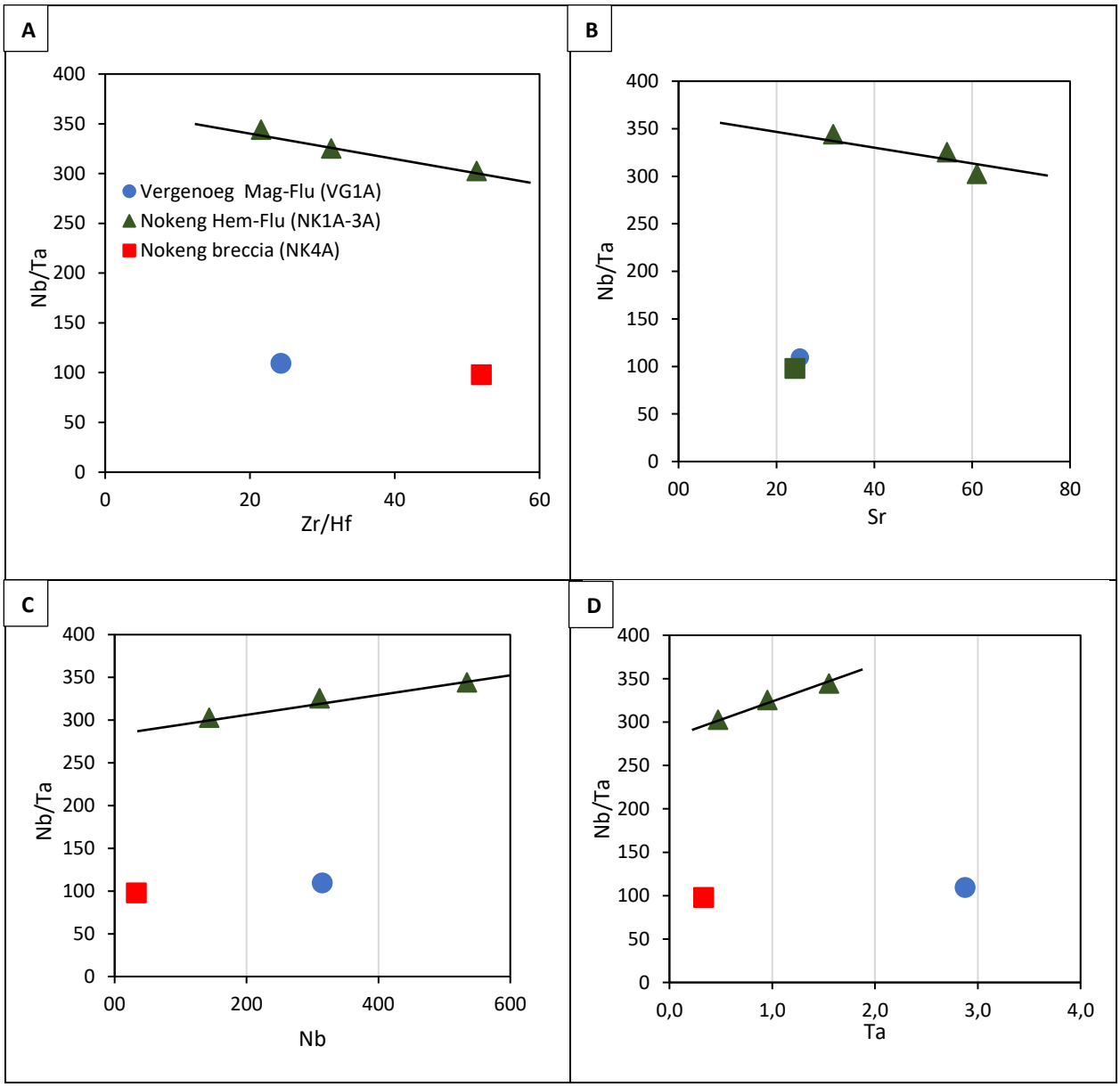

Figure 33. Binary plots of Nb/Ta vs Zr/Hf, Sr, Nb, and Ta. These plots represent the Nokeng and Vergenoeg rocks. The back lines show trends in the data.

The Nokeng ignimbrite unit is represented by NK4 (lithic clast-supported breccia), which was cut/subdivided into NK4A-D. The four splits (NK4A, NK4B, NK4C and NK4D) show significant variations in SiO_2 content, where NK4C and NK4D reveal concentrations of 26 wt % and 56 wt.% SiO_2 respectively. The uneven distribution of SiO_2 in these samples reflects the coarse-clastic texture of the rock. The elevated SiO_2 content in certain splits can be attributed to rhyolitic fragments, whereas the Si-poorer splits contain a higher proportion of the tuffaceous

matrix replaced by hematite. The CaO content in the breccia ranges from 6.7 to 17.0 wt.%, which is significantly lower than the hematite-fluorite ore (21.6 to 45.2 wt.%). This is consistent with the hypothesis by Crocker (1985) which suggested that the early-stage magmas were characterised by high Si and low Ca content. Notably, the breccia has elevated FeO^t concentrations ranging from 28.6 wt.% in NK4A to 44.9 wt.% in NK4B. The observed variability in FeO^t is attributed to varying degree of hematite precipitation and replacement within the Plattekop deposit. Furthermore, the geochemical data reveals a negative relationship between SiO_2 and FeO^t (Figure 13b).

Graupner et al. (2015), states that the occurrence of minerals with rims, veinlets and cavity fillings in rocks alludes to the presence of hydrothermal fluids. Evidently, Figure 12c and 12d display veinlets of hematite traversing fluorite grains and Figure 31a shows monazite along with cassiterite forming veinlets cross-cutting quartz and fluorite. Silicate minerals are also recorded filling cavities between the fluorite grains in Figure 10c and Figure 10e. Therefore, the apparent character of Plattekop rocks, in association with Graupner et al. (2015)'s statement, evidences the possible influence of hydrothermal fluids within the deposit. Moreover, the anhedral fluorite grains in NK3A (Figure 10d) indicate possible fluorite precipitation from hydrothermal fluids in fractures/cavities of rocks. These cavities represent gas voids or microchannels, which are common in pyroclastic rocks. Conversely, NK2A, depicted in Figure 10e displays subhedral to euhedral fluorite grain that displays perfect octahedral cleavage planes that intersect at roughly ± 120 degrees. This texture argues for fluorite crystallization from magmas with adequate space for crystals to fully form, prior to hematite and silica precipitation. Therefore, the observed textures of Plattekop rocks along with the observations reported by Graupner et al. (2015) support a significant degree of precipitation from hydrothermal fluids, however. the proportions of primary magmatic and fluid-derived material are difficult to estimate. The Nokeng rhyolitic breccia samples also display veinlets of specularitic hematite that traverse a large rhyolitic tuff fragment (Figure 11a). There are also interstitial anhedral fluorite and hematite grains found between quartz grains in Figure 11d. Moreover, there is widespread hematite replacement and chlorite pseudomorphs after feldspar in the Nokeng breccias. This supports the idea, that the ignimbrite unit and its basal breccia were also affected by hydrothermal activities

7.2 Comparative analysis between the rocks found at Nokeng Vs Vergenoeg, implications for facies association.

7.2.1 Tectonic and geological setting of the Plattekop and Vergenoeg deposits

The Plattekop and Vergenoeg deposits are both encompassed within the Kaapvaal Craton of South Africa. These two deposits are hosted within the Paleoproterozoic Bushveld Igneous Complex's Rooiberg Group, which was deposited in a subaerial environment in an intra-cratonic setting (Chiya, 2020). It is evident that, regionally the Plattekop and Vergenoeg deposits were subjected to a similar tectonically quiet environment away from dynamic conditions associated with plate tectonic boundaries. This similarity in the tectonic setting is attributed to the proximity of the deposits (± 1 000 m apart) in Figure 1. However, locally there is a disparity in the two deposits' general setting, lithostratigraphy, deposition and mineralogy. The Vergenoeg Mine pit lies directly within a (540 000 m^2) discordant volcanic pipe, whereas the Plattekop lies on the peripheries of this pipe. The Vergenoeg discordant pipe is about 650 m deep and it is composed of hematite-fluorite, magnetite-fluorite, magnetite-fayalite and fayalite. Conversely, the Plattekop deposit has an areal extent of about 800m^2 and a thickness of 20m, which is much smaller than the Vergenoeg pipe. The Plattekop deposit is characterised by hematite tuff beds, the froth-flow channel lag deposit and the fines-depleted lag agglomerates. This deposit constitutes eroded remnants of the Vergence pipe and it represents a sedimentary depositional environment. This is supported by Figure 34, which shows the sedimentary textures and flow banding. Mineral endowment within the Vergenoeg and Plattekop deposits is directly and indirectly linked to the intrusion of the Lebowa Granite Suite, which induced exogranitic polymetallic Sn-Fe-F-REE mineralisation in the Rooiberg Group (Robb et al., 2000; Crocker et al., 2001).

7.2.2 Lithological and Petrographic comparison between the Nokeng vs Vergenoeg rocks

According to Crocker (1985), the upper gossan (Zone 1) at the Vergenoeg pipe is composed completely of fluorite, hematite, and goethite ore. The formation of hematite in this gossan is attributed to the alteration of magnetite, siderite and grunerite (Crocker, 1985). Notably, this upper gossan (Zone 1) resembles the petrographic characteristics of the Plattekop hematite-fluorite unit, however, the proportion of goethite is lower in the Plattekop hematite-fluorite unit. In terms of the general stratigraphy (Table 5), the Plattekop ores do not belong to the discordant pipe or the nearest surroundings within the volcanic edifice but are confined to the roughly stratified pyroclastic

sequence. The petrographic observations support clastic origin of or at least some part of fluorite in ores. The complete absence of primary magmatic magnetite and other silicates suggests that the original environments of ore deposition were highly oxidised and corresponded to hematite stability. This is consistent with the model by Fourie (2000), which suggests that the Plattekop deposit is a mineralized pyroclastic flow of a violent explosion. Moreover, this study reveals the presence of fluorite in eruptive breccia, which also supports the opinion by Fourie (2004) that breccia predates most of fluorite-rich units and occurs at the base of the stratified sequence. Lastly, the influence of hydrothermal fluids throughout the Vergenoeg Rock Suite is evident from the petrographic descriptions, however, the scale of remobilization of the ore components is difficult to estimate based on available data.

Although, the hematite-fluorite gossan shows some petrographic similarities to the Plattekop hematite-fluorite unit. There are apparent variations between the two unit, firstly the fluorite grains found within the gossan, are generally large and well defined, whereas the Plattekop displays occurrences of small fluorite grains forming a matrix in Figure 10c. These smaller grain sizes, together with the elevated occurrence of transportation resistant components such as quartz is typical of distal facies. Moreover, sedimentary bedding structures were found within the hematite-fluorite unit, which, alludes to transportation and subsequent deposition of the grains (Crocker, 1985 and Graupner et al., 2015). Transportation of the hematite fluorite ores is supported by flow bands in Figure 34. The red line in Figure 34 separates the rock into a phaneritic and porphyritic section. This is typical of pyroclastic flows, which often possess a basal flow band with coarser fragments and an upper component made up of finer less dense material (USGS, 2024). Transportation and bedding structures were not recorded within the Vergenoeg gossan, which, suggests that it crystallized in situ, in proximity to the Vergenoeg volcanic pipe. Lastly, the Vergenoeg gossan has a 3-5 m thick portion (Zone 2) that rests below Zone 1, this portion is partially oxidised and contains sulphides, including pyrite, pyrrhotite, chalcopyrite and sphalerite (Crocker, 1985). Notably, sulphide minerals such as pyrite, pyrrhotite, etc., were not found during the petrographic analysis of the hematite-fluorite unit.

The Nokeng basal breccia shows low resemblance to rocks of the Vergenoeg pipe. These coarse-clastic lithic breccia comprise lenses within the stratified ignimbritic sequence. Due to superimposed hematisation, it is difficult to estimate the initial proportion of ferruginous tuff, which makes up the matrix of the breccia.

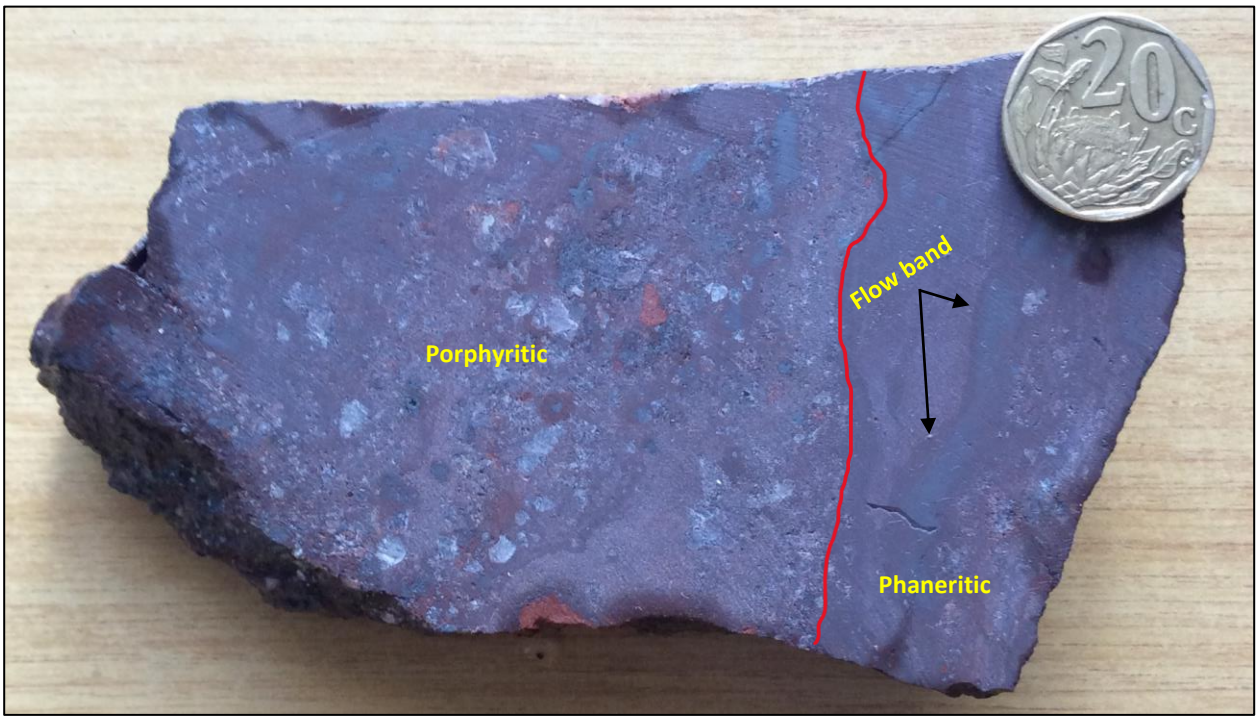

Figure 34. Hematite fluorite sample (NK2), sourced from the Nokeng open pit mine, displaying a brecciated texture that comprises fragments of rhyolite in fluorspar-hematite matrix. The black arrows show flow bands, and the red line separates the porphyritic and phaneritic sections of the rock.

7.2.3 Geochemical comparison between Nokeng and Vergenoeg rocks

Results from Graupner et al. (2015)'s research show that the magnetite-fluorite unit possesses low silica dioxide content at 1.77 wt.%, similarly to VG1, which has the SiO_2 content that ranges between 1.24 and 1.91 wt.%. This is expected as these two rocks belong to the same ore type. There are also similarities in their FeO^t, CaO, MgO, and TiO_2 contents (Figure 29a to d). The CaO content is a proxy for high fluorite content and results show that the ore content in the Nokeng distal facies (21.6-41.7 wt.% CaO) is comparably high with respect to that in the more proximal facies (27.4-43.2 wt.% CaO) at Vergenoeg.

The Vergenoeg hematite-fluorite gossan, similarly to the Nokeng hematite-fluorite unit, reveals high concentrations of CaO with a value of 39.91 wt.%, and a modest concentration of SiO_2 (29.41wt.%). However, it is important to note that there are some critical geochemical disparities observed between the Nokeng hematite-fluorite unit and the Vergenoeg hematite-fluorite gossan. The Plattekop hematite-fluorite unit is variably enriched in silica depending on the varying proportions of the Si-rich rhyolitic material and Ca-rich fluorite (Figure 13a), whereas the Vergenoeg gossan possesses 29.4 wt.% SiO_2. The Vergenoeg gossan (SA09-106) (Figure 35a to d) shows conspicuously low FeO^t content with a value of 13.5 wt.%, whereas the Nokeng hematite-fluorite has an average value of 32.7 wt.% FeO^t. This variation in SiO_2 content and FeO^t between the two units reflects their highly heterogeneous nature with varying enrichments in fluorite.

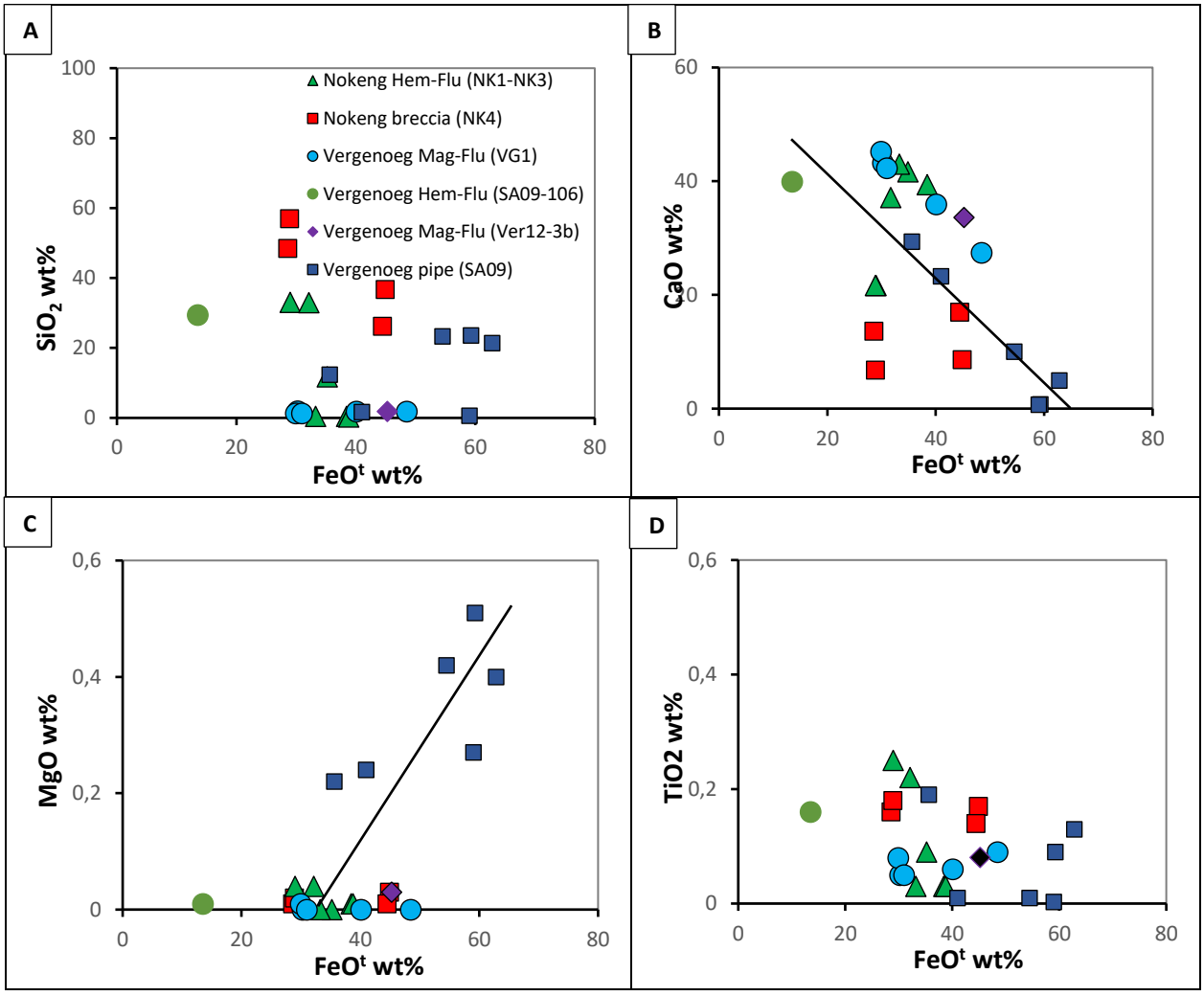

Figure 35. Comparison between the compositions of Vergenoeg and Nokeng ores and associated units based on the data from this study and 8 Vergenoeg whole rock analyses available from Graupner et al. (2015). The binary plots include FeO^t vs SiO_2, CaO, MgO and TiO_2.

The geochemical plot in Figure 36 reveals that all the Plattekop hematite-fluorite rocks (NK1, NK2, NK3), as well as the Vergenoeg magnetite-fluorite ore (VG1) plot in the calc-alkaline series field. In contrast, the rhyolitic breccia has two samples (NK4A and NK4D) plotting in the tholeiitic series field. This emphasises the disparity between the rhyolitic breccia and other units within the Vergenoeg Rock Suite. Conversely, the lower MgO and TiO_2 values (Figure 35c and Figure 35d) suggest that there are similarities in the composition of magma that formed the hematite-fluorite unit, magnetite-fluorite unit and rhyolitic breccia whereas magnetite-fayalite rocks from the deeper part of the pipe are composed of earlier cumulates with contrasting compositions that are not analogous to the Plattekop ore field.

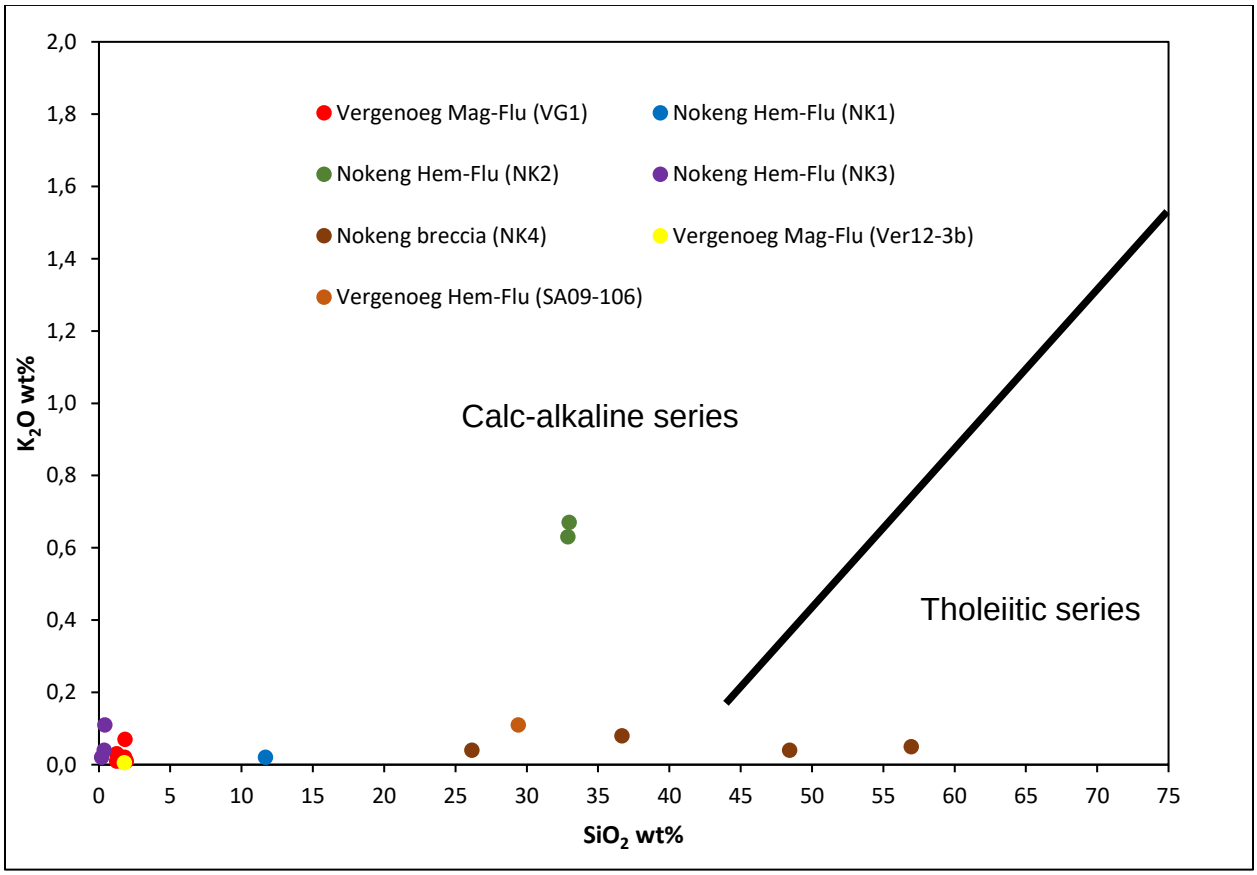

Figure 36. Discriminant plot of SiO_2 vs K_2O for volcanic rocks, showing specific fields including a calc-alkaline magma series and a tholeiitic magma series (Peccerillo and Taylor, 1976). The diagram also shows where the different rocks from Nokeng and Vergenoeg plot. Major element values for Ver12-3b (Vergenoeg magnetite-fluorite) and SA09-106 (Vergenoeg gossan) were sourced from Graupner et al. (2015)

A discrimination plot of Ta/Yb against Th/Yb (Figure 37) reveals that the magnetite-fluorite ore (VG1 and Ver12-3b) plots in the within plate volcanic zones, whereas the Nokeng hematite-fluorite ore (NK1A, NK2A and NK3A), Nokeng ignimbrite units (NK4) and the Vergenoeg hematite-fluorite gossan (SA09-106) plot in the active continental margin. This an unexpected result and it indicates that the discrimination diagrams should not be used for volcanic rocks *sensu stricto*.

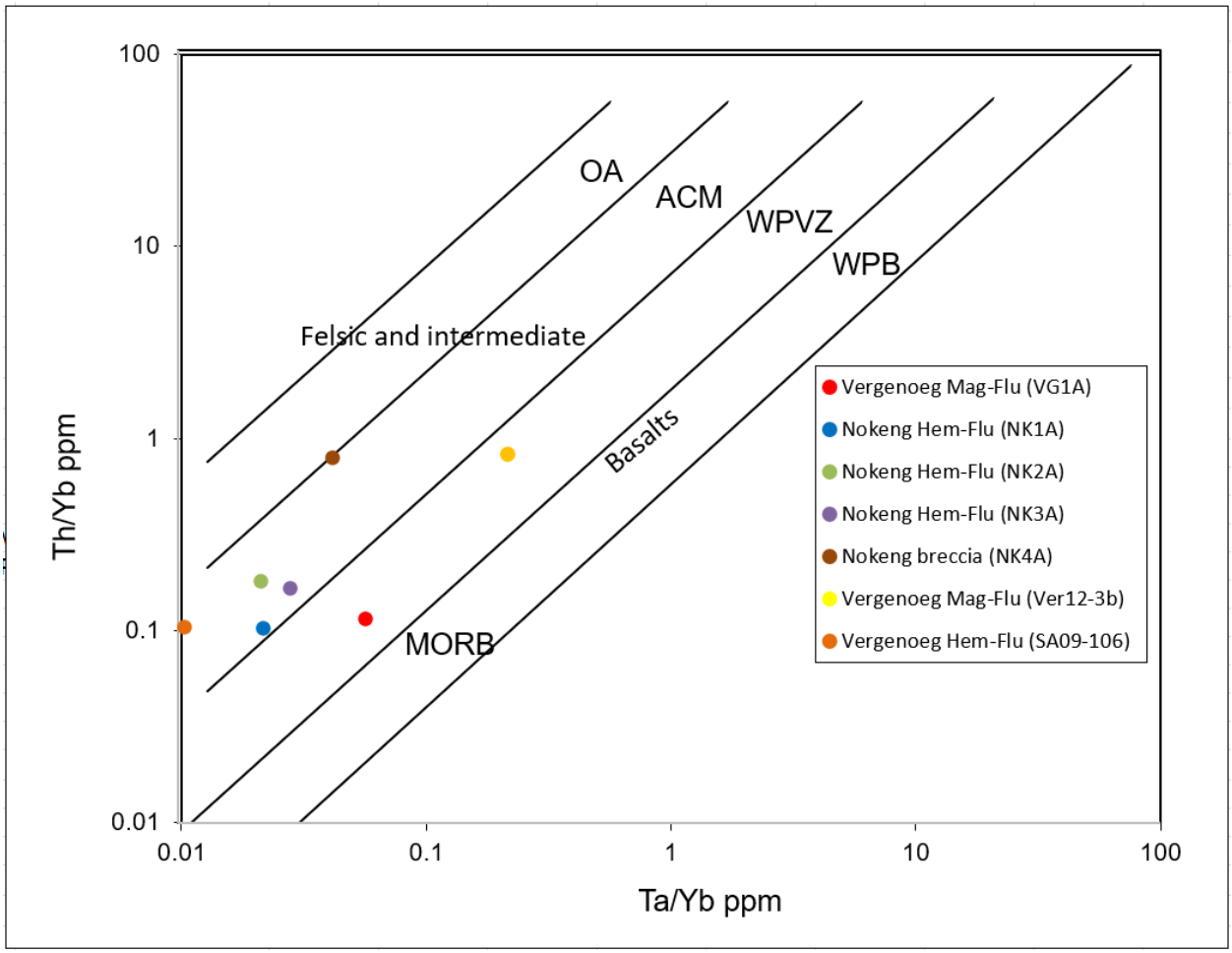

Figure 37. Discriminant plot of Ta/Yb plotted against Th/Yb. This diagram shows where the different rocks from the Nokeng and Vergenoeg Mine plot in relation to the outlined tectonic field. Oceanic arcs = OA; Active continental margins = ACM; Within-plate volcanic zones = WPVZ; Within plate basalts = WPB; Mid-ocean ridge basalt = MORB. Gorton and Schandl, 2000. Major element values for Ver12-3b (Vergenoeg magnetite-fluorite) and SA09-106 (Vergenoeg gossan) were sourced from Graupner et al. (2015).

Lastly, the Nb/Y vs Zr/Ti plot (Figure 38) was used to classify the Nokeng and Vergenoeg rocks based on the suggested fields for volcanic rocks. Notably, NK4A, which has been described as rhyolitic breccia, plots in the rhyolite field whereas the other samples (NK3A, NK1A and VG1A) plot within the andesite field with NK2 falling in the intermediate rhyodacite/dacite field. Again, the anomalous enrichment in fluorite, coupled with the high Y content (510-2900 ppm according to the LA ICPMS data by Graupner et a., 2015), may result in the disturbance of the primary characteristics of the melt. This is further exacerbated by hydrothermal re-working, which alters the rocks' original makeup.

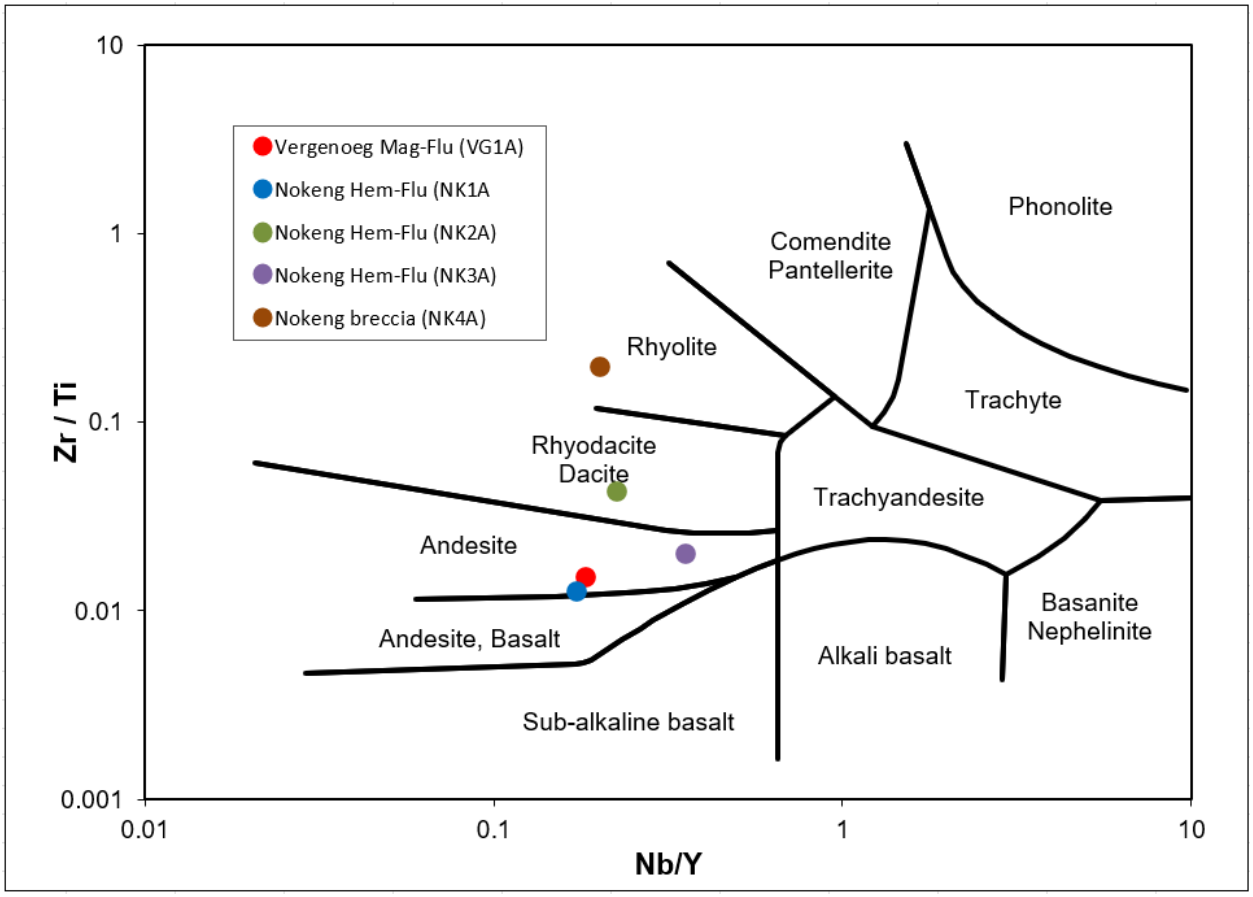

Figure 38. Discriminant plot of Nb/Y vs Zr/Ti for rocks from the Nokeng and Vergenoeg mines. This plot categorised the rocks into different fields, including alkali basalt, trachyandesite, basanite nephelinite, sub-alkaline basalt, trachyte, phonolite, comendite, andesite-basalt, andesite rhyodacite and lastly the rhyolite field (Winchester and Floyd, 1977).

7.3 REE Mineralization within the Nokeng and Vergenoeg mines

7.3.1 REE mineralization in Nokeng

The mineral maps and BSE images generated by the TIMA and SEM revealed the presence of REE minerals such as bastnasite, monazite and xenotime within the Plattekop deposit. Additionally, the ICPMS analysis revealed significant REE+Y concentrations in Plattekop rocks, with the hematite-fluorite unit showing the highest concentration of REE + Y. The total REE+Y concentrations vary within the deposit, with NK1A revealing a value of 5890 ppm, NK3A - 3408 ppm, and lastly, NK2B – 3089 ppm (Table 4). All samples display an enrichment in light rare earth elements (LREEs) compared to heavy rare earth elements (HREEs) based on the PM-normalised REE plot in Figure 15. The hematite-fluorite unit rocks also display a 'seagull pattern', with a negative europium anomaly. According to Winter (2014), the negative Eu indicates that the liquid was at one point in equilibrium with plagioclase.. Plagioclase incorporates Eu^{2+}, which substitutes for Ca, and subsequently depletes the Eu content in the (Winter, 2014), which, is reflected by the negative peak in the PM-normalised REE pattern in Figure 15.

The TIMA analysis conducted on NK1A reveals that the dominant REE rich mineral phase within the sample is bastnasite. It makes up 0.72 % in Section A and accounts for 0.18 % of the total mineral mass percentage in Section B (Figures 17a and b). The second most abundant REE-rich mineral is monazite, which is found in both Section A and Section B, with total mineral mass percentages of 0.05 % and 0.26 % respectively. Evidently, monazite is less abundant compared to bastnasite in section A but surpasses the bastnasite content in Section B. The estimates of the mineral proportions are biased due to the specific area on the thin section that was deliberately chosen for the analysis (Figures 16a and b). However, it is valid that bastnasite is the dominant mineral throughout the entire thin section (NK1A). Lastly, xenotime is found in the reduced concentrations in section A and Section B, with the recorded phase percentages of 0.02 % and 0.03 % respectively. Bastnasite generally occurs as disseminated grains (Figure 22a) that reach maximum sizes of about 200 µm (Figure C.5, Appendix C). Monazite and xenotime display reduced grain sizes compared to the bastnasite with maximum sizes of about ~100 µm (Figure C.6, Appendix C) and ~80 µm (Figure C.7, Appendix C) respectively. Similarly to bastnasite, monazite and xenotime appear disseminated or aggregated into veinlets (Figure 22c-f). Bastnasite is variably locked in goethite-hematite, fluorite, and quartz in Section A.

According to the ICPMS analysis, Ce contributes the highest concentration of 1842 ppm among the REEs in the Plattekop hematite-fluorite unit. The elemental deportment analysis suggests that 94 % of the element is contained within bastnasite $(La,Ce,Y)CO_3F$, with the balance (6 %) encompassed within monazite $(Ce,La,Nd,Th)(PO_4SiO_4)$. This is expected, given that bastnasite is more abundant than monazite although both are rich in Ce. Yttrium also displays an elevated concentration of 1805.4 ppm in Section A. Evidently 100 % of Y is contained within xenotime YPO_4. Lanthanum is contained within bastnasite (97 %) and monazite (3 %), whereas Nd is hosted within monazite (100 %). Notably, out of the three REE minerals, only monazite possesses significant Nd concentrations.

Rhyolitic breccia of the ignimbrite unit displays a reduced REE+Y concentration of about 1107 ppm (Figure 39a-f), which differs greatly from the recorded concentrations in the hematite-fluorite unit. This depletion could be attributed to the reduced concentration of CaO in the rhyolitic breccia. The general positive correlation between REE+Y and CaO (Figure 39a) and the absence of any correlation between REE+Y and FeO^t or SiO_2 (Figure 39a and 39b) suggests that higher grade fluorite ores are richer in REE+Y and P. Fluorite contributes a significant proportion of Y to the total REE + Y according to the LA ICP-MS data by Graupner et al. (2015) whereas phosphates and carbonates provide the REEs. Decoupling of monazite and fluorite in rhyolitic breccias is supported by the SEM images of NK4B (Figures 32a, b), where monazite is only surrounded by hematite and quartz, with no fluorite. Therefore, the paucity of fluorite mineralization, which is associated with REE enrichment, is the likely cause of the low REE+Y in the Plattekop ignimbrite unit.

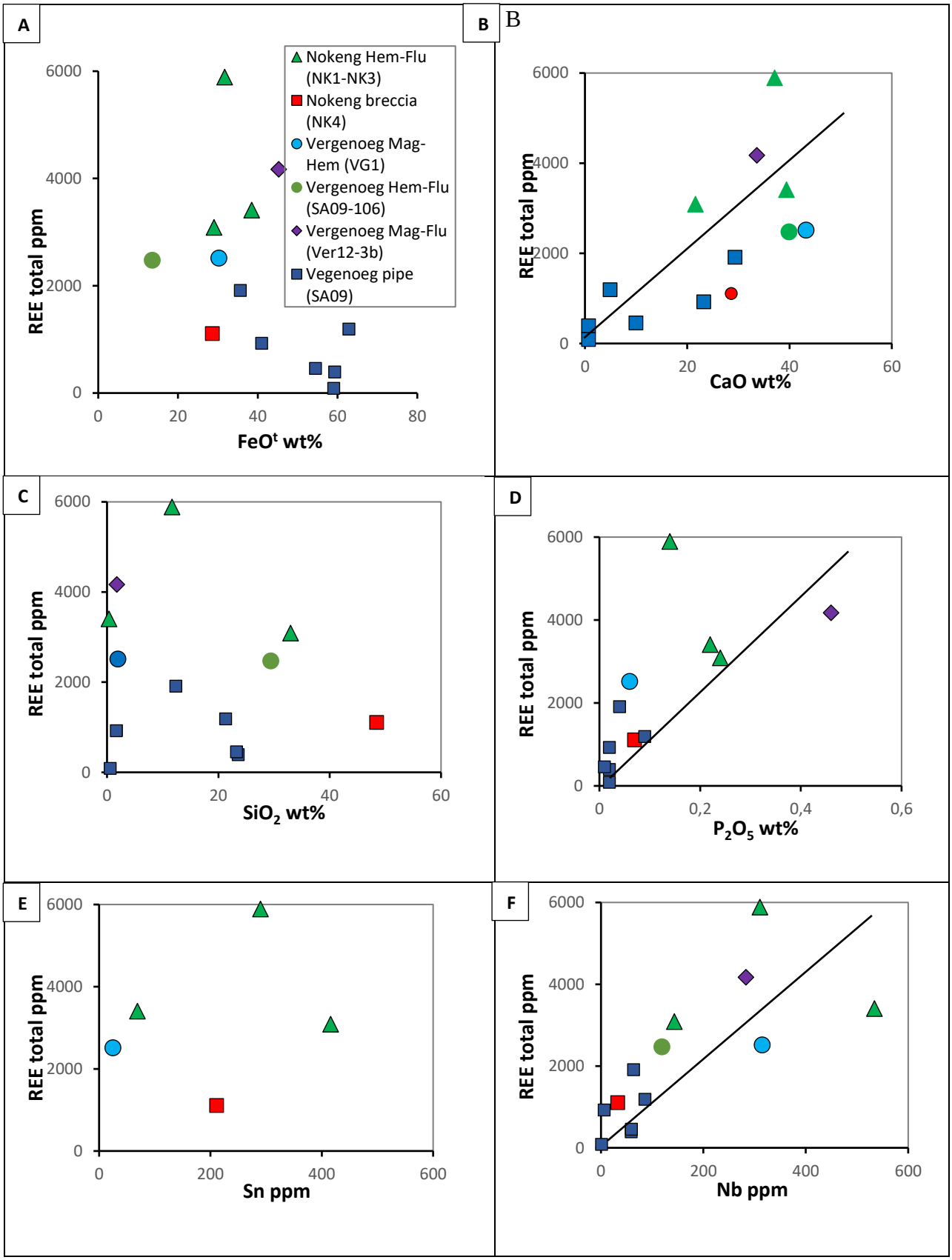

Figure 39. Binary plots of REE+Y vs FeO^t, SiO_2, CaO, P_2O_5, Nb and Sn for the different units of the Nokeng and Vergenoeg deposits based on the data from this study (Table B.1, Appendix B) and Graupner et al. (2015).

7.3.2 Comparative analysis between REE mineralization found in Nokeng versus Vergenoeg

According to the geochemical data of Graupner et al. (2015), the Vergenoeg magnetite-fluorite ore (Ver12-3b) has an REE + Y concentration of 4 171 ppm, whereas the hematite-fluorite gossan (SA09-106) reveals a value of 2 475 ppm (Table C.4 in Appendix C; Figure 39a-f). Notably, the magnetite-fluorite ore sample (VG1) analysed in this study contains a REE+Y concentration of 2 519 ppm. The observed variations are justifiable as it is common for REEs to be unevenly distributed in rocks of the same unit (e.g., NK2A and NK1A display variable REE + Y concentrations). Crocker (1985) argued that the apical portions of the Vergenoeg gossan are completely leached, with fluorite being remobilized to lower depths of about a few centimetres, where it can only be seen when the rock is broken. Moreover, Crocker (1985) suggested that REE minerals such as xenotime, monazite, fluocerite and bastnasite found within the pipe are associated with fluorite. Therefore, the slightly lower REE + Y content in the Vergenoeg gossan could be caused by leaching of REE-rich fluorite, however, it is not consistent with the high CaO content of over 39 wt.% in the hematite-fluorite gossan analysed by Graupner et al. (2015). Therefore, it is suggested that the slightly lower REE+Y content in the Vergenoeg samples with respect to that in the Nokeng samples is caused by natural heterogeneity of REE mineral distribution. This is supported by the extremely high REE+Y concentrations exceeding 1 wt.% reported by Goff et al. (2004) for Vergenoeg magnetite-fluorite ores.

The geochemical results also reveal that the REE + Y concentrations decrease with decreasing Ca and P content (Figures 39b and 39d) throughout all the units within the Vergenoeg ore field, including the fayalite, magnetite-fayalite, siderite lenses and ‘metspar’ plugs (Graupner et al., 2015). The highest concentration of REE + Y is found in the hematite-fluorite unit of the Plattekop deposit, followed by the Vergenoeg magnetite-fluorite unit; the ‘metspar’ plugs, hematite-fluorite gossan, the fayalite unit, the Nokeng ignimbrite unit, the Vergenoeg magnetite-fayalite unit and, lasty, the Vergenoeg siderite lenses (Table 4 and Table C.4 in Appendix C; and Figure 39a-f). Notably, no correlation exists between the REE+Y concentrations and Fe-oxide or silica content for the whole set of the available data. The content of selected incompatible elements, such as Ta, Nb, W and Sn, positively correlates with Ca, P and REE+Y (Figures 39e and 39f). This is consistent with mineralogical observations, which outline the presence of cassiterite (SnO_2) in association with REE phosphates (Figure 39e).

The binary plots of Y vs CaO, P_2O_5 and La vs CaO, P_2O_5 were created to deduce the preferential hosts of LREE and HREE (Figures 40a-d). There is a positive correlation between Y and CaO in Figure 40c. This suggests that the elevated concentration of Y in the Vergenoeg magnetite-fluorite unit and the Nokeng hematite-fluorite unit is directly related to the higher CaO content in these units. Figure 40a displays a decreasing trend, which means that LREEs such as La are not preferentially hosted in minerals with high CaO content. However, sample NK1A deviates from this generally negative trend, displaying relatively high concentrations of La and CaO; this sample is considered as an outlier. Figures 40a and b don't show a clear correlation of P_2O_5 against La and Y.

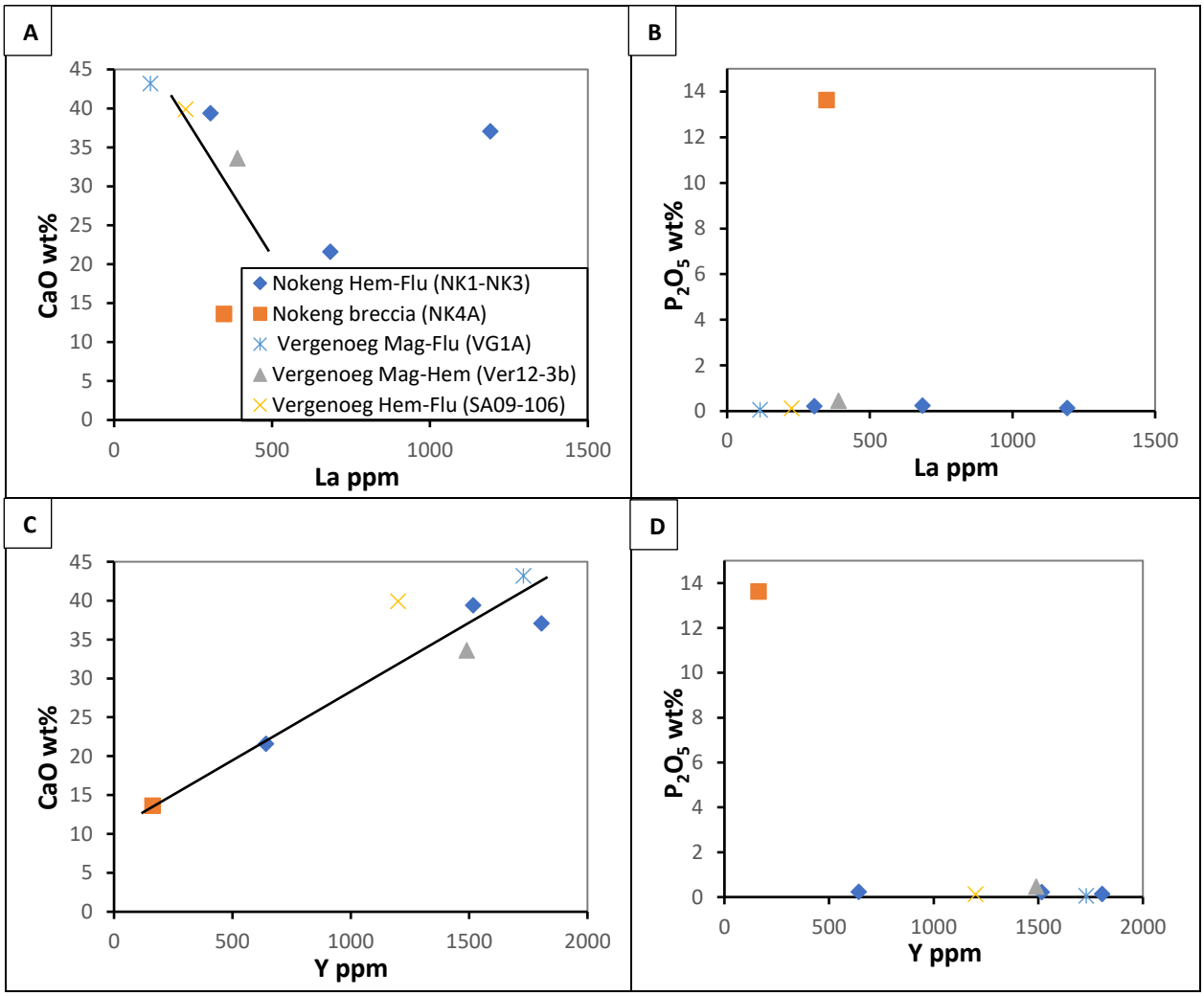

Figure 40. Binary plots of Y vs CaO, P_2O_5 and La vs CaO, P_2O_5. These plots represent the Nokeng and Vergenoeg rocks. Major and minor element values for Ver12-3b (Vergenoeg magnetite-fluorite) and SA09-106 (Vergenoeg gossan) were sourced from Graupner et al. (2015). The back line shows the trend in the data.

The REE PM-normalised plot in Figure 41 shows a general seagull-like shape for Vergenoeg fluorite ores, which is similar to the patterns for Nokeng ores. However, Vergenoeg ores display slightly lower degrees of LREE fractionation and relatively flattened HREE distributions. Magnetite-fayalite rocks from the Vergenoeg pipe yield different V-shaped distributions with a sharp enrichment in HREEs. This differs from the pattern for Plattekop breccia, which shows an enrichment in LREEs compared to HREEs. All rocks display a similar scale negative Eu anomaly except for rhyolitic breccia. This can also be attributed to the removal of Eu^{2+} with cumulus plagioclase stored at depth and, therefore, creating the deficit.

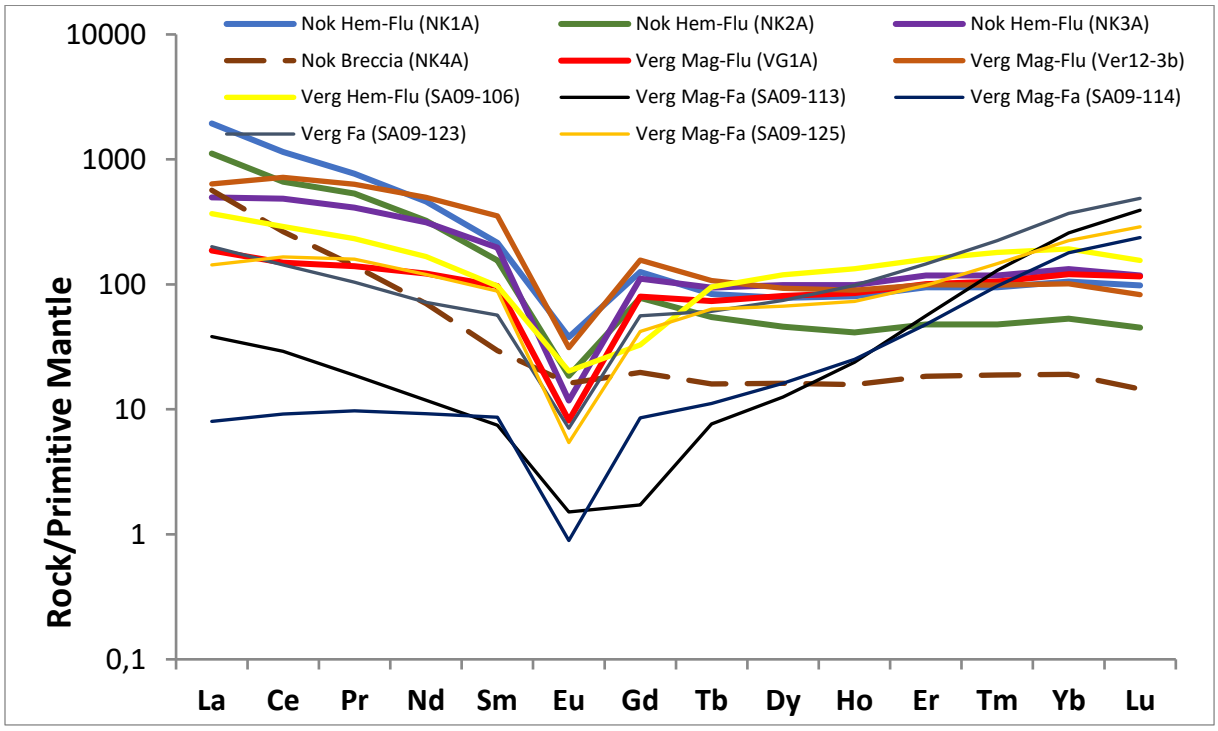

Figure 41. Primitive Mantle normalized REE distribution patterns for the whole-rock samples of the Nokeng ores and rhyolitic breccia in comparison with the whole-rock data from various ores and rocks of the Vergenoeg deposit (taken from Graupner et al. 2015 and sample VG1A from this study). The data were normalized using the values of Hoffman (1988).

The Vergenoeg magnetite-fluorite ore (VG1) was analysed for REE-rich mineral distribution. Section A of VG1A in Figure 25 shows that there is only 0.09 % xenotime in the sample, whereas Section B reveals only 0.02 %. The xenotime found in VG1 is dominantly locked in hematite/magnetite, goethite, and fluorite. Notably, the high yttrium (1729.4 ppm) content recorded within VG1A, is 100 % associated with xenotime. This is like NK1A where yttrium is

also hosted 100 % in xenotime. The high resolution phase maps (Figure 25) also confirmed the presences of minor bastnasite along with monazite in VG1A. The second most abundant REE in VG1A is cerium with a concentration of 239 ppm and 51 % of the element is contained within bastnasite, whereas 49 % is hosted in monazite. Evidently, Ce in NK1A is also accommodated by monazite and bastnasite, which, further advocates for shared similarities between the two deposits. Moreover, the Vergenoeg hematite-fluorite ore clearly displays the presence of all REE minerals recorded for the Plattekop deposit, including bastnasite, monazite and xenotime.

Crocker (1985), Goff et al. (2004) and Graupner et al. (2015) employed whole rock geochemistry to deduce the concentration of REEs within the Vergenoeg Rock Suite, whereas the other studies by Borrok et al. (1988) and Brandt et al. (2019, 2020) used micro methods such as electron probe microanalysis (EPMA) and laser ablation ICP-MS (LA-ICPMS) on individual mineral grains. It is noteworthy that analysis conducted on individual mineral grains using EPMA and LA-ICPMS revealed extremely high concentrations of REEs in the accessory minerals. Brandt et al. (2015) conducted research on fayalite-bearing rocks and reported a total REE content of about 200 000 ppm for the allanite. Moreover, apatite shows equally high REE+Y concentrations ranging between 143000 – 177000 ppm for Si-rich cumulus apatite. These REE + Y concentrations in the minerals differ greatly from the whole rock REE+Y concentrations. However, the abundances of these REE + Y rich accessory minerals (allanite and apatite) is very low, and they were not found in the studied Plattekop rocks. Both Graupner et al. (2015) and Brandt et al. (2019) reported very modest REE content in fluorite (of about 181-5057 ppm REE+Y).

7.4 Analysis of the Plattekop and Vergenoeg pipe REEs with implications for mining the deposits

7.4.1 Feasibility of REE extraction within the Plattekop and Vergenoeg deposits.

The availability of REEs with significant grades is the most imperative factor in deducing whether REEs in the Plattekop and Vergenoeg pipe deposits can be mined economically. An elevated concentration of REE + Y within the deposits would increase the probability of a successful operation. Evidently, almost all units within the Plattekop and Vergenoeg area record the occurrence of REEs. The Plattekop hematite-fluorite unit reported concentrations up to ~6000 ppm REE + Y whereas the Vergenoeg magnetite-fluorite unit revealed concentrations of over 1 wt.% (Goff et al., 2004). According to Witley et al. (2021), Lofdal, which is a carbonatite hosted exploration target in Namibia, has an estimated 42.57 million tonnes of 0.17 wt.% TREO, which is above the 0.1 wt.% cut-off grade as per the measured and indicated resources. Evidently, fluorite ores of Nokeng and Vergenoeg surpass the 1000 ppm (0.1 wt.%) cut-off by a margin. Moreover, Nehoya (2023) states that mineralized rocks from the Karingarab carbonatite deposit (Namibia) that possesses a grade under 3000 ppm TREO were still economic. However, no boreholes data was analysed in this study to effectively estimate the extent of the ore body. This, therefore, inhibits the ability to do any tonnage calculations. Moreover, the boreholes would aid in delineating areas with higher concentrations (ore shoots), which is important for mineral resource estimation (MRE) purposes. Regarding mining and processing ores for REEs, it is an advantage that the high-grade ore is located at the apical portions of the Plattekop deposit. The magnetite-fluorite ore, which is rich in REEs, is also located relatively higher up in the Vergenoeg stratigraphy. This means that, a relatively inexpensive opencast mining operation could be used in exploiting this ore and affect the final cost. The open pits already exist for both the Plattekop and Vergenoeg fluorite deposits where high grade fluorite is currently being mined so the extracted REE could be a by-product.

The extraction of REEs is also an important factor, and this is controlled by their mineral association and elemental deportment. This determines the ease, in which the elements can be extracted from host minerals. An example is monazite, which usually contains thorium and uranium, thus, giving it radioactive properties (Witharana et al. 2021). This means the extraction of elements, such as cerium and neodymium from monazite would require advanced methods to mitigate any radioactive spills. However, the REEs within the Plattekop deposit are mostly hosted within bastnasite and xenotime, except for Nd which occurs 100 % in monazite. The processing

of REE minerals such as bastnasite still requires advanced technological methods. Around 90 % of the world total REE production is attributed to China (Witharana et al. 2021), largely because they have the capacity to process these mineralogically complex REE-rich phases. Therefore, the economic potential of the Plattekop and Vergenoeg deposits also rests on the availability of a processing plants to extract the REEs.

The positive geometallurgical estimate of efficient REE processing as a by-product from the Vergenoeg ore and tailings (Kern, 2013; Birtel et al., 2014) suggests that similar conclusions could be applicable to the Nokeng orebody. These studies found that Vergenoeg tailings are strongly enriched in well liberated monazite and xenotime that could be extracted as a future by-product by flotation through modification of the current flow sheet. According to Kern (2013) and Birtel et al. (2014), REE minerals make up 1-4 wt.% of the vergenoeg tailings and approximately 54 wt.% of xenotime and monazite grains found in the tailings stream are liberated. However, the exact quantity of the REE mineral grains that are liberated in the Plattekop deposit has not been efficiently deduced. The shallow setting of the Nokeng orebody and the high proportion of the most expensive HREE and Y are favourable factors.

7.5. Limitations of the study

There was no access to drillholes, which could aid in defining how the Plattekop deposit varies with depth. Moreover, access to equally spaced-out drillholes, like the ones analysed by Crocker (1985), could help elucidate the lateral variations occurring within the pipe. The borehole data would also aid in deducing whether the Plattekop deposit is indeed the distal facies of the Vergenoeg pipe. This project was based on 4 large samples from the Nokeng Fluorite Mine and 1 from the Vergenoeg volcanic pipe, collection of more samples from both open pit mines could increase the validity of this study. Given the heterogeneous nature of the Vergenoeg Rock Suite it would be ideal to have analysed all the 15 rock splits from the 5 initial samples using ICPMS. Moreover, TIMA was only done on 2 samples (NK1A and VG1A). It would have been beneficial to analyse all the splits for the REE deportment, including NK1A, NK2A, NK3A, NK4A and VG1A. A comparison with the Vergenoeg hematite-fluorite gossan that shows some similarities to the Plattekop hematite-fluorite unit is also required for the reliable facies' association implications. The absence of LA-ICPMS and EPMA results inhibited comparison between this

study's results and those gathered by Borrok et al. (1998), Graupner et al. (2015) and Brandt et al. (2019, 2020) who used those analytical methods.

Conclusions

The Nokeng Fluorite Mine's Plattekop deposit is characterized by an upper hematite-fluorite unit and a basal ignimbrite unit. The hematite-fluorite unit is dominated by iron oxides and hydroxides (hematite and minor goethite), and fluorite with subordinate quartz, whereas lithic breccia from the ignimbrite unit is manly composed of large rhyolitic fragments, massive and specularitic hematite and minor fluorite. There is a great petrographic and geochemical disparity between these two units, supported by their varying mineralogy, textures and stratigraphic position. It is suggested that the basal breccia formed at the initial stage of felsic volcanism, as a result of stratified pyroclastic flowage, whereas the hematite-fluorite unit formed in the later stage, which was dominated by explosion of Ca-F rich magma. This is evidenced by the reduced concentration of CaO in the ignimbrite unit compared to the hematite-fluorite unit, which show high concentrations of CaO. The variations in geochemical signatures of the studied splits (e.g. NK2A and NK2B) of the same rock (e.g., NK2) are attributed to the coarse-grained texture of the fluorite aggregates as well as the varying degrees of hydrothermal alteration and hematite replacement, which gives the rock a heterogeneous character.

The Nokeng hematite-fluorite unit resembles the Vergenoeg pipe's upper hematite-fluorite ore. Mineralogically this is the same ore type, primarily composed of hematite and fluorite with subordinate quartz and goethite. It is suggested that most of the hematite contained within the Plattekop and Vergenoeg hematite-fluorite units was formed through the alteration of magnetite. The magnetite replacement is evident in the Vergenoeg magnetite-fluorite unit, which displays hematite progressively replacing the magnetite upwards. Given the apparent similarities between the Nokeng and Vergenoeg rocks, it is postulated that the Nokeng hematite-fluorite unit is a distal extension of hematite-fluorite stratum of the Vergenoeg ore field. Breccia of the ignimbrite unit is attributed to rhyolitic lava and ash material violently ejected from the Vergenoeg volcano forming the basal layer of the pyroclastic flow.

The Plattekop deposit is enriched with REE minerals including bastnasite, monazite and xenotime. Similarly, the Vergenoeg deposit reveals an abundance of REE-bearing minerals, which include allanite, apatite, bastnasite, monazite and xenotime (Borrok et al., 1998, Fourie, 2004; Goff

et al., 2004; Brandt et al., 2019, 2020; Graupner et al., 2015). This study reveals that the Plattekop hematite-fluorite unit possesses the same high level REE concentrations compared to the ore units within the Vergenoeg Suite. This is supported by the elevated total REE + Y of up to 5890 ppm in the Plattekop hematite-fluorite unit, however, rhyolitic breccia of the ignimbrite unit shows reduced REE concentrations of 1107 ppm. Both Nokeng and Vergenoeg fluorite ores are characterised by the significant enrichment in LREEs compared to unfractionated HREEs, whereas poorly mineralized rocks show less disparity between the LREEs and the HREEs.

There is a high global demand for REEs because of their importance in green energy technologies such as wind turbines and electric vehicles. This high demand for REEs is further exacerbated by geopolitical factors, where China, which produces more than 70 % of the worlds' REEs, threatens the global supply by stockpiling the commodity. This high demand for REEs coupled with the geopolitical factors has greatly increased the price for these commodities. Although the Plattekop and Vergenoeg deposit reveal an enrichment in REEs and the earlier metallurgical studies confirmed the feasibility of REE processing as a by-product (Kern, 2013; Birtel et al., 2015), there are no information on economic exploitation of these resources. Around 90 % of all REEs are processed in China, because of the country's historical investment in the mining and processing REEs. Therefore, it is important to attract attention to more complete exploitation and utilisation of the natural resources in South Africa.

References

- Ballouard, C., Poujol, M., and Boulvais. 2016. Nb-Ta fractionation in peraluminous granites: A marker of the magmatic-hydrothermal transition: Reply, Geology, 44-7.
- Barton, E. S. and Hallbauer, D. K. 1996. Trace-element and U-Pb isotope compositions of pyrite types in the Proterozoic Black Reef, Transvaal Sequence, South Africa: Implications on genesis and age. Chemical Geology, 133, 173 – 199
- Birtel, S., Kern, M., Höfig, T.W., Krause, J. and Gutzmer, J. 2015. Geometallurgical Assessment: Beneficiation of Rare Earth Minerals as a Possible By-Product from the Vergenoeg Fluorite Mine, South Africa. In: Proceedings of the 13th Biennial SGA Meeting (mineral resources in a sustainable world), Nancy, France, 1383– 1386.
- Borrok, D. M., Kelser, S. E., Boer, R. H. and Essene, E. J. 1998. The Vergenoeg magnetite–fluorite deposit, South Africa; support for a hydrothermal model for massive Fe-oxide deposits. Economic Geology 93, 564–586.
- Brandt, S., Klemd, R., Haase, K.M., Fassbender, M.L. and Vennemann, T. 2019. 'Formation of the vergenoeg F–fe–ree deposit (South Africa) by accumulation from a ferroan silicic magma', Journal of Petrology, 60-12, 2339–2368.
- Bryan, S.E. and Ernst, R.E. 2008. Revised definition of Large Igneous Provinces LIPs. Earth Science Reviews 86, 175–202.
- Buchanan, P.C., Reimold, W.U., Koeberl, C. and Kruger, F.J. 2004. Rb-Sr and Sm-Nd isotopic compositions of the Rooiberg Group, South Africa: early Bushveld-related volcanism. Lithos 29, 373-388.
- Buchanan, P.C. 2006. The Rooiberg Group, in: Johnson, M.R., Anhaeusser, C.R., Thomas, R.J. (Eds.), The Geology of South Africa. Geological Society of South Africa, Johannesburg and Council for Geoscience, Pretoria, 283-289.
- Bumby, A.J., Eriksson, P.G., Catuneanu, O., Nelson, D.R. and Rigby, M.J. 2012. Meso-Archaean and Palaeo-Proterozoic sedimentary sequence stratigraphy of the Kaapvaal Craton. Marine and Petroleum Geology. 33-1,92–116.
- Button, A. 1986. The Transvaal sub-basin of the Transvaal Sequence. In: Anhaeusser, C. R., Maske, S. (Eds), Mineral Deposits in Southern Africa. Geological Society of South Africa, Johannesburg. 1, 811 – 817.
- Cawthorn, R.G. 2013. The residual or roof zone of the Bushveld Complex, South Africa. J Petrol 54-9, 875–1900.
- Chakmouradian, A.R. and Wall, F. 2012. Rare Earth Elements: Minerals, Mines, Magnets (and more). Elements, 8, 333-340.
- Chiya, L. 2023. Petrography and geochemistry of hydrothermal breccias hosted in the Schrikkloof Formation (Rooiberg Group), north of Modimolle, South Africa. Unpublished thesis. University of Pretoria.

- Coffin, M.F. and Eldholm, O. 1994. Large igneous provinces: crustal structure, dimensions and external consequences. Reviews of Geophysics, 32, 1-36.
- Connelly, N. G. 2005. 'Nomenclature of inorganic chemistry - IUPAC recommendations 2005', Chemistry. De Gruyter, 16-6, 561–568.
- Cheney, E. S. 1996. Sequence stratigraphy and plate tectonic significance of the Transvaal succession of southern Africa and its equivalent in Western Australia. Precambrian Research, 79, 3-24.
- Chevychelov, V.Y., Zaraisky, G.P., Borisovskii, S.E., Borkov, D.A. 2005. Effect of melt composition and temperature on the partitioning of Ta, Nb, Mn, and F between granitic (alkaline) melt and fluorine-bearing aqueous fluid: fractionation of Ta and Nb and conditions of ore formation in rare-metal granites. Translated from Petrologiya 13-4, 339-357. Petrology 13, 305-321.
- Crocker, I. T.1985. Volcanogenic fluorite–hematite deposits and associated pyroclastic rock suite at Vergenoeg, Bushveld Complex. Economic Geology 80, 1181–1200.
- De Kock, M.O., Beukes, N.J. and Armstrong, R.A. 2012. New SHRIMP U–Pb zircon ages from the Hartswater Group, South Africa: Implications for correlations of the Neoarchean Ventersdorp Supergroup on the Kaapvaal Craton and with the Fortescue Group on the Pilbara craton. Precambrian Research 204–205, 66–74.
- De Wit, M.J. and Kruger, F.J. 1990. The economoic potential of the Dufel Complex. In: Splettstoesser, J.F. & Dreschoff, G.A.M. (Eds.) Mineral Resources Potential of Antartica. American Geophysical Union Antartic Research Series 5, 33-52.
- De Wit, J. M., Roering, C., Hart, R. J., Armstrong, R. A., De Ronde, C. E. J., Green, R. W. E., Tredoux, M., Peberdy, E. and Hart, R. A. 1992. Formation of an Archean continent. Nature, 357, 553-562.
- Els, B. G., van den Berg, W. A. and Mayer, J. J. 1995. The Black Reef Quartzite Formation in the western Transvaal: sedimentological and economic aspects, and significance for basin evolution. Mineralium Deposita, 30, 112 – 123.
- Eriksson P. G., Hattingh P. J. and Altermann W. 1995. An overview of the geology of the Transvaal Sequence and Bushveld Complex, South Africa. Mineralium Deposita 30 :98–11
- Eriksson, P.G., Altermann, W., Hartzer, F.J. 2006. The Transvaal Supergroup and its precursors, In: Johnson, M.R., Anhaeusser, C.R., and Thomas, R.J. (eds.). The Geology of South Africa, Johannesburg, Geological Society of South Africa, Pretoria, Council for Geoscience, 237–260.
- Eterigho-Ikelegbe, O., Yoro, K.O. and Bada, S. 2021. 'Coal as a filler in polymer composites: A Review', Resources, Conservation and Recycling, 174, 105756.
- EURARE. 2022. What are rare earth elements. Available at:
- https://www.eurare.org/RareEarthElements.html. [Accessed: 26 February 2024].

- European Commission. 2010. Critical raw materials for the EU: Report of the Ad-hoc Working Group on defining critical raw materials. European Commission (Enterprise and Industry).
- Frimmel, H. E. and Minter, W. E. L. 2002. Recent developments concerning the geological history and genesis of the Witwatersrand gold deposits, South Africa. Society of Economic Geologists Special Publication, 9, 17 – 45
- Fourie, P. J. 2000. The Vergenoeg fayalite iron oxide fluorite deposit, South Africa: some new aspects. In: Porter, T.M. (ed.) Hydrothermal Iron Oxide Copper–Gold and Related Deposits a Global Perspective. Adelaide, SA: Australian Mineral Foundation, 309–320.
- Gast, P. W. 1972. The chemical composition and structure of the moon. The Moon, 5, 121-148.
- Gholz, E. 2014. Rare Earth Elements and National Security. Council on Foreign Relations, New York.
- Giordano, G. and Cas, R.A.F. 2021. 'Classification of ignimbrites and their eruptions', Earth-Science Reviews, 220, 103697.
- Goff, B. H., Weinberg, R., Groves, D. I., Vielreicher, N. M. & & Fourie, P. J. 2004. The giant Vergenoeg fluorite deposit in a magnetite–fluorite–fayalite REE pipe: A hydrothermal-altered carbonatite-related pegmatoid? Mineralogy and Petrology 80,
- Gorton, M.P. and Schandl, E.S. 2000. From continents to island arcs: a geochemical index of tectonic setting for arc-related and within-plate felsic to intermediate volcanic rocks. Canadian Mineralogist, 38, 1065-1073.
- Graupner, T., Muhlbach, C., Schwarz-Schampera, U., HenjesKunst, F., Melcher, F. and Terblanche, H .2015. Mineralogy of high-field-strength elements (Y, Nb, REE) in the world-class Vergenoeg fluorite deposit, South Africa. Ore Geology Reviews 64, 583–601.
- Groenewald, G and Groenewald, D. 2014. SAHRA Palaeotechnical Report. Palaeontological Heritage of the Mpumalanga Province, 24.
- Gupta, C.K. and Krishnamurthy, N. 2005. Extractive Metallurgy of Rare Earths. CRC Press, Boca Raton.
- Harmer, R.E. and Armstrong, R.A. 2000. New precise dates on the acid phase of the Bushveld and their implications. In Workshop on the Bushveld Complex, University of the Witwatersrand, Johannesburg, South Africa, 11, 12.
- Harmer, R.E. and Sharpe, MR. 1985. Field relations and Sr isotope systematics of the marginal rock of the Eastern Bushveld Complex. Econ Geol 80, 813–837.
- Hatton, C. J. and Schweitzer, J. K. 1995. Evidence for synchronous extrusive and intrusive Bushveld magmatism. Journal of African Earth Sciences 21, 579–594.
- Hatch, G. P. 2012. Dynamics in the global market for rare earths. Elements, 8.
- Hofmann AW. 1988. Chemical differentiation of the earth. The relationship between mantle, continental crust, and oceanic crust. Earth Planet Sci Lett 90, 297-314.

- Hou, T., Charlier, B., Namur, O., Schu¨ tte, P., SchwarzSchampera, U., Zhang, Z. C. &and Holtz, F. 2017. Experimental study of liquid immiscibility in the Kiruna-type Vergenoeg iron–fluorine deposit, South Africa. Geochimica et Cosmochimica Acta 203, 303–322.
- Kern, M. 2013. Geometallurgical assessment of the rare earth mineralogy and processing characteristics at the Vergenoeg Fluorite Mine, South Africa. Unpublished thesis. Technische Universitat Bergakademie Freiberg.
- Kinnaird, J.A. 2005. The Bushveld Large Igneous Province. Review Paper, the University of the Witwatersrand, Johannesburg, 39.
- Kinnaird, J.A., Kruger, P.A.M., Nex, P.A.M. and Cawthorn, R.G. 2002. 'Chromitite Formation—a key to understanding processes of platinum enrichment', Applied Earth Science, 111-1, 23–35.
- Kinnaird, J.A., Hutchinson, D., Schürmann, L.W., Nex, P., and de Lange, R. 2004. Petrology and mineralization of the southern Platreef: northern limb of the Bushveld Complex, South Africa. Mineralium Deposita, in press.
- Kinnaird, J.A., Yudovskaya, M.A., McCreesh, M., Huthmann, F., and Botha, T.J. 2017. The Waterberg platinum group element deposit: Atypical mineralization in mafic-ultramafic rocks of the Bushveld Complex: Economic Geology, 112, 1367–1394.
- Kruger, F. J. 1989. The geochronology and Sr-isotope geochemistry of the Molopo Farms Complex, Bushveld Magmatic Province: a preliminary report. Molopo Botswana (Pty) Ltd. Final Report for Prospecting Licences 14/85 and 38/90. Open File Report, Geological Survey Botswana.
- Kurnio, H., 2019. Geochemical Characteristics of Sunda Volcanic Arc in Sumatra and Andaman. Indonesian Journal on Geoscience, 6-1, 1-16.
- Mapeo, R.B.M., Kampuznu, A.B., Ramokate, L.V., Corfu, F. and Key, R.M. 2004. Bushveld-age magmatism in southeastern botswana: evidence from U-Pb zircon and titanite geochronology of the Moshaneng Complex. South African Journal of Geology 107, 219-232
- Lenhardt, N. and Eriksson, P.G. 2012. 'Volcanism of the Palaeoproterozoic Bushveld Large Igneous Province: The Rooiberg Group, Kaapvaal Craton, South Africa', Precambrian Research, 214–215, 82–94.
- Li, Z., Zhang, S., Zheng, Y., Wu, S., Li, W., Sun, F., Liang, T. 2022. Mobilization and fractionation of HFSE and REE by high fluorine fluid of magmatic origin during the alteration of amphibolite, Lithos,420–421,106701.
- Mariano, A.N. and Mariano Jr., A. 2012. Rare Earth Mining and Exploration in North America. Elements, 8, 369-376.
- Massari, S. and Ruberti, M. 2013. Rare Earth Elements as Critical Raw Materials: Focus on International Markets and Future Strategies. Resources Policy, 38, 36-43.
- Morrison, W.M. and Tang, R. 2012. China's Rare Earth Industry and Export Regime. Economic and Trade Implications for the United States. Congressional Research Service.

- Mutele, L. and Hunt, J.p. 2022. Investigation of hydrothermally altered “Mantos" zones in granites of the southwestern Bushveld complex, South Africa: Insight into their mode of formation and F-REE mineralization. Journal of African Earth Sciences. 194.
- Nehoya, J.N. 2023. A review of mineral exploration at the Karingarab carbonatite, southern Namibia. Unpublished MSc research report, University of the Witwatersrand.
- Nokeng Fluorspar Mine (Pty) LTD. 2019. Fact sheet. Available from: https://www.sepfluor.co.za/images/downloads/nokeng-fact-sheet-WS9-25092019.pdf [Accessed 15 May 2022].
- Ozturk, N. 2018. Fluid interaction in carbonatite and alkaline composite intrusions and implications for rare earth element mineralization. Unpublished thesis, University of the Witwatersrand.
- Pearce, J., Harris, N. and Tindle, A. G. 1984. Trace Element Discrimination Diagrams for the Tectonic Interpretation of Granitic Rocks. Journal of Petrology. 25, 956-983
- Peccerillo, A. and Taylor, S.R. 1976. Geochemistry of eocene calc-alkaline volcanic rocks from the Kastamonu area, northern Turkey. Contributions to Mineralogy and Petrology, 58, 63-81.
- Pingitore Jr., N.E., Clague, J.W. and Gorski, D. 2018. Re- markably Consistent Rare Earth Element Grades at Round Top Yttrofluorite Deposit. Advances in Materials Physics and Chemi- stry, 8, 1-14.
- Pires, K. de, Mendes, J. J., Figueiredo, V. C., Silva, F. L., Krüger, F. L., Vieira, C. B., and Araújo, F. G. 2019. Mineralogical characterization of iron ore tailings from the Quadrilatero Ferrifero, Brazil, by Eletronic Quantitative Mineralogy. Materials Research, 22-1.
- Robb, L.J. 1983. Trace element trends in granites and the distinction between partial melting and crystal fractionation processes. Case studies from two granites in Southern Africa. In: S.S. Augustithis {Editor), The Significance of Trace Elements in Solving Petrogenetic Problems and Controversies. Theophrastus Publications, Athens, 279-294.
- Rudnick R.L. 1998. Elements: Large-ion lithophile. In: Geochemistry. Encyclopedia of Earth Science. Springer, Dordrecht.
- Saunders, A. D., Tarney, J. and Weaver, S. D. 1980. Transverse geochemical variations across the Antarctic peninsula: implications for the genesis of calc-alkaline magmas. Earth and Planetary Science Letters, 46, 344–360
- Scherhag, C., 1990. Flußspat-Lagerstätten in Südafrika - ein Überblick. Erzmetall 43, 28–33.
- Schröder, S.N., Beukes, J., Armstrong, R.A. 2016. Detrital zircon constraints on the tectonostratigraphy of the Paleoproterozoic Pretoria Group, South Africa. Precambr. Res. 278, 362–393.
- Schweitzer, J.K., 1987. The transition from the Dullstroom Basalt Formation to the Rooiberg Felsite Group, Transvaal Supergroup: a volcanological, geochemical and petrological investigation. Ph.D. thesis, University of Pretoria.

- Schweitzer, J.K., Hatton, C.J., de Waal, S.A., 1995. Regional lithochemical stratigraphy of the Rooiberg Group, upper Transvaal Supergroup: a proposed new subdivision. S. Afr. J. Geol. 98, 245-255.
- Schutte, P.2005. Investigations on the genesis of the Vergenoeg Fe–F deposit, RSA. Diploma thesis, University of Hannover.
- Scoates, J. S., Wall, C. J., Friedman, R. M., Weis, D., Mathez, E. A., and VanTongeren, J. A. 2021. Dating the Bushveld complex: Timing of crystallization, duration of magmatism, and cooling of the world's largest layered intrusion and related rocks. Journal of Petrology, 62-2.
- Skursch, O., Corfu, F. and Tegner, C., Lesher, E., Anderson, R., Hagen-Peter, A., Vorvoort and J.D. 2022. Zircon U–Pb chronology and Hf isotopes of the Lebowa Granite Suite and petrogenesis of the Bushveld Complex, South Africa. Contrib Mineral Petrol 177, 26
- Spandler, C., Slezak, P., Nazari-Dehkordi, T. 2020. Tectonic significance of Australian rare earth element deposits, Earth-Science Reviews, 207, 103219.
- Srinivasan, H. 2023. Critical earth minerals are more in demand than ever-here are the ones to know, Investopedia. Available at: https://www.investopedia.com/critical-earth-minerals-7568912 [Accessed: 26 February 2024].
- Statista. 2022. Rare earth element facts[online]. Distribution of rare earths production worldwide as of 2022, by country [online]. Availble from: [Accessed 14 May 2023].
- Steenkampskraal Holdings LTD. 2018. Steenkampskraal rare earth and thorium project, western cape, South Africa. Information Memorandum. 1-2
- Sun, S.S. and McDonough, W. F. 1989. Chemical and isotopic systematics of oceanic basalts: implications for mantle com- position and processes. In: Saunders, A. D. & & Norry, M. J. (eds) Magmatism in the Ocean Basins. Geological Society, London, Special Publications 42, 313–345.
- Taylor, C.D., Schulz, K.J., Doebrich, J.L., Orris, G.J., Denning, P.D., and Kirschbaum, M.J. 2005. Geology and nonfuel mineral deposits of Africa and the Middle East, USGS Open-File Report, 294-E
- USGS. 2024. Pyroclastic flows move fast and destroy everything in their path [Online]. Available from: Pyroclastic flows move fast and destroy everything in their path | U.S. Geological Survey (usgs.gov). [Accessed 19 July 2024].
- Van Tongeren, J.A., Mathez, E.A. and Kelemen, P.B. 2010. A felsic end to Bushveld Differentiation. J. Petrol. 51, 1891-1912.
- VanTongeren, J. A. & & Mathez, E. A. 2015. On the relationships between the Bushveld Complex and its felsic roof rocks, part 2: The immediate roof. Contributions to Mineralogy and Petrology 170, 56.
- VanTongeren, J. A., Zirakparvar, N. A. and Mathez, E. A. 2016. Hf isotopic evidence for a cogenetic magma source for the Bushveld Complex and associated felsic magmas. Lithos 248, 469–477.

- Viljoen, M.1. and Schiirmann, L.W. 1998. Platinum group metals. In: Wilson, M.G.C and Anhaeusser, CR. (Eds.), The Mineral Resources I~(South A.ti·ica. Coun. Geosci., S. Afr., Pretoria, S. Afr. 532-568.
- Walraven F. 1997. Geochronology of the Rooiberg Group, Transvaal Supergroup, South Africa. EGRI Information Circular 316, University of the Witwatersrand, 21.
- Weng, Z.H., Jowitt, S.M., Mudd, G.M., and Haque, N. 2013a. Assessing rare earth element mineral deposit types and links to environmental impacts. Applied Earth Science, 122-2, 83–96.
- White, W. M. 2001. Geochemistry. 1st Edition. John Wiley and Sons Inc. New York, United States. Published 2013.
- Winchester, J.A., and Floyd, P.A. 1977. Geochemical discrimination of different magma series and their differentiation products using immobile elements: Chemical Geology, 20, 325-343.
- Winter, J.D. 2014. Pearson New International Edition: Principles of igneous and Metamorphic Petrology. Harlow: Pearson.
- Witharana, W.P.W.S., Prabath, D.H.L., Madushanka, R.S., Rohitha, L.P.S., Dissanayake, D.M.D.O.K. 2021. Extraction of rare earths from monazite in Pulmoddai deposit. In D.M.D.O.K. Dissanayake & C.L. Jayawardena (Eds.), Proceedings of International Symposium on Earth Resources Management & Environment. 135-142.
- Witley, J.C., Swinden, S., and Aghamrian, M. 2021. Namibia Critical Metals Inc. Lofdal Heavy Rare Earths Project Namibia. NI 43-101 Technical Report – 20 May 2021 Mineral Resource Estimate. Khorixas District, Republic of Namibia, MSA Project No.: J4327. The MSA group.
- Yang, X.S., Heino, N. and Pakkanen, L. 2019. Beneficiation Studies of a Rare Earth Ore from the Olserum Deposit. Natural Resources, 10, 346- 357.
- Yudovskaya, M., Masunte, T., Kinnaird, J. A., Mwenze, T., Ueckermann, H., Iaccheri, L. and Bolhar, R. 2023. An extension of the Rooiberg Group and Upper Zone of the Bushveld complex in the northernmost Waterberg segment. Precambrian Research, 399, 107228.
- Zegers, T. E., de Wit, M. J., Dann, J. and White, S. H. 1998. Vaalbarra, Earth's oldest assembled continent? A combined structural, geochronical, and paleomagnetic test. Terra Nova, 10, 250-259.
- Zeh, A., Wilson, A., H. and Gerdes, A. 2020. Zircon U-Pb-Hf isotope systematics of the Transvaal Supergroup – Constraints for the geodynamic evolution of the Kaapvaal Craton and its hinterland between 2.65 and 2.06 Ga. Precambrian Research, 345, 1 – 20.

Appndix A – Petrographic Descriptions

1. Nokeng Hematite-Fluorite Unit

Sample name: NK1.

Modal Mineralogy: hematite (55 %), fluorite (35 %), quartz (10 %)

Sample	Thin-Section	Description
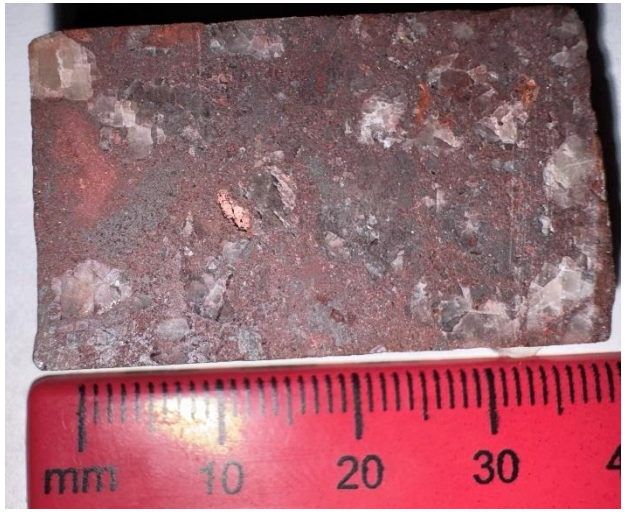	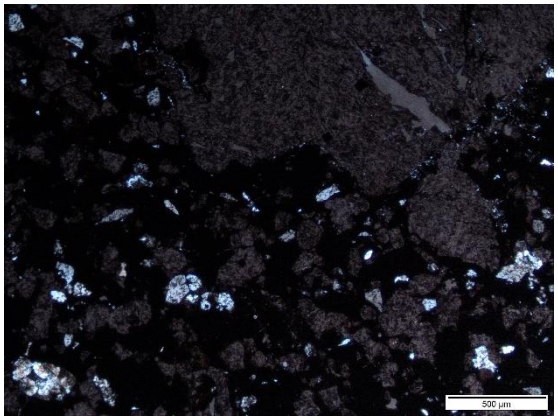	**NK1A breccia-like hematite-fluorite ore.** **Modal proportions:** Hematite (55 %), Fluorite (35 %), Quartz (10 %). The hand specimen shows fluorite coarse grains or clasts surrounded by a matrix of reddish hematite and blackish specularitic hematite. In the thin section the sample shows fluorite grains surrounded by a matrix of hematite, smaller fluorite grains and quartz. The image is in XPL.

Sample name: NK2.

Modal Mineralogy: hematite (50 %), fluorite (30 %), quartz (15 %)

Sample	Thin-Section	Description
	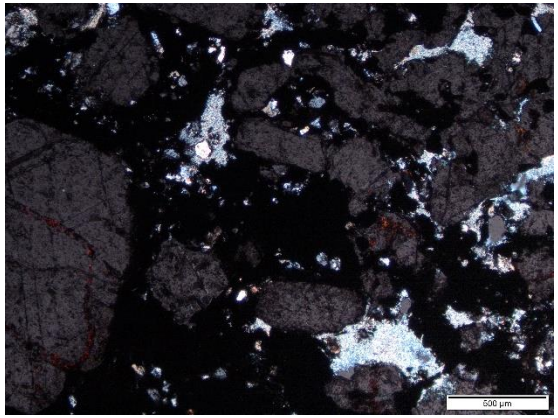	**NK2A stratified hematite-fluorite ore** The hand specimen shows fine grained interstitial fluorite grains and reddish rhyolite clasts in a matrix of, massive hematite and minor specularitic greyish hematite. On the left – a lense of rhyolitic tuff coloured by dispersed hematite. In the thin section the sample shows fine interstitial fluorite grains gilling the space between hematite and rock clastes. There are also inclusions of reddish hematite in fluorite grains. Image is in XPL.
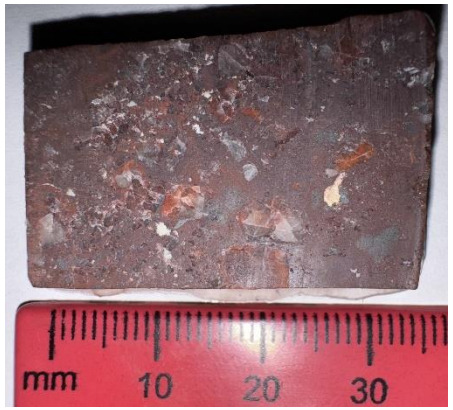	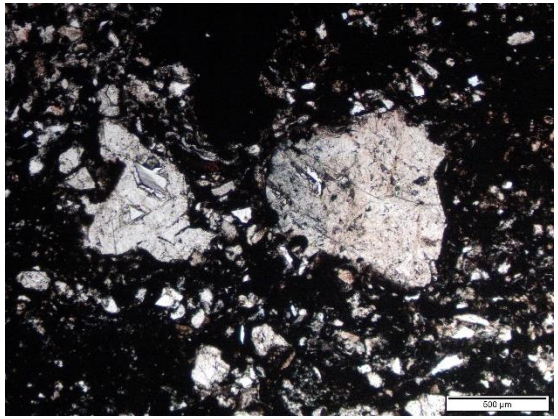	**NK2B breccia-like hematite-fluorite ore** The hand specimen shows coarser grained fluorite crystals in a matrix of reddish hematite and minor specularitic greyish hematite. In the thin section the sample shows fluorite grains surrounded by a matrix of black hematite and silicate minerals. Image is in PPL.

Sample name: NK3.

Modal Mineralogy: hematite (53 %), fluorite (46 %), quartz (1 %)

Sample	Thin-Section	Description
	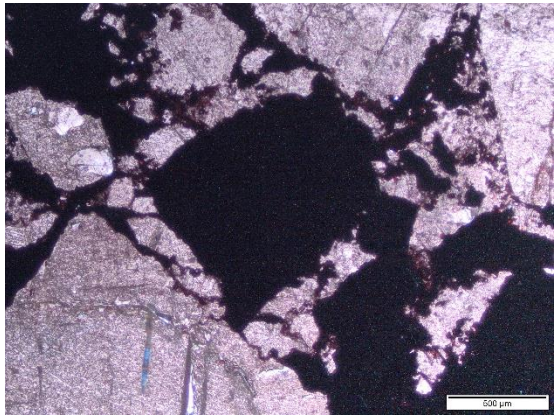	**This is NK3A** The hand specimen shows coarse grained fluorite, with a distinct purple colour that is set in a matrix of reddish hematite and minor specularitic greyish hematite. In the thin section the sample shows coarse fluorite grains surrounded by a matrix of black hematite. Image is in XPL.
	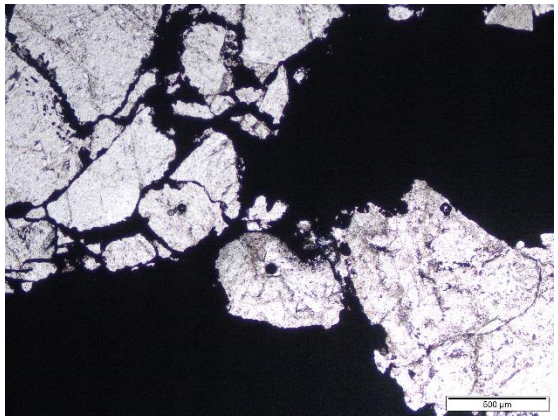	**This is NK3B** The hand specimen shows coarse grained fluorite, with a distinct purple colour that is set in a matrix of reddish hematite and minor specularitic greyish hematite. In the thin section the sample shows coarse fluorite grains surrounded by a matrix of black hematite. Image is in PPL.

	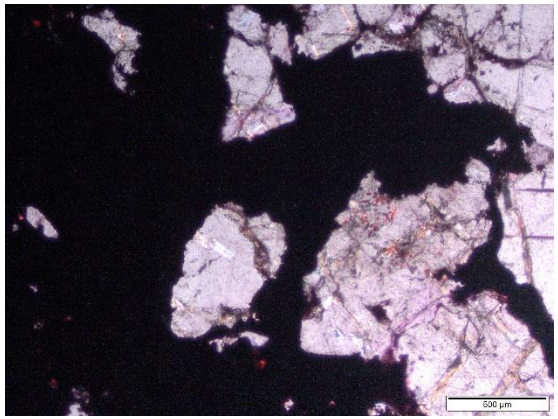	**This is NK3C** The hand specimen shows coarse grained fluorite, with a distinct purple colour that is set in a matrix of reddish hematite and minor specularitic greyish hematite. In the thin section the sample shows coarse fluorite grains that have hematite veins moving through them. The fluorite grains are surrounded by a matrix of black hematite. Image is in XPL.

2. Breccia agglomerate Unit

Sample name: NK4.

Modal Mineralogy: hematite (40 %), magnetite (10 %), rhyolitic clasts containing quartz after tridymite (50 %)

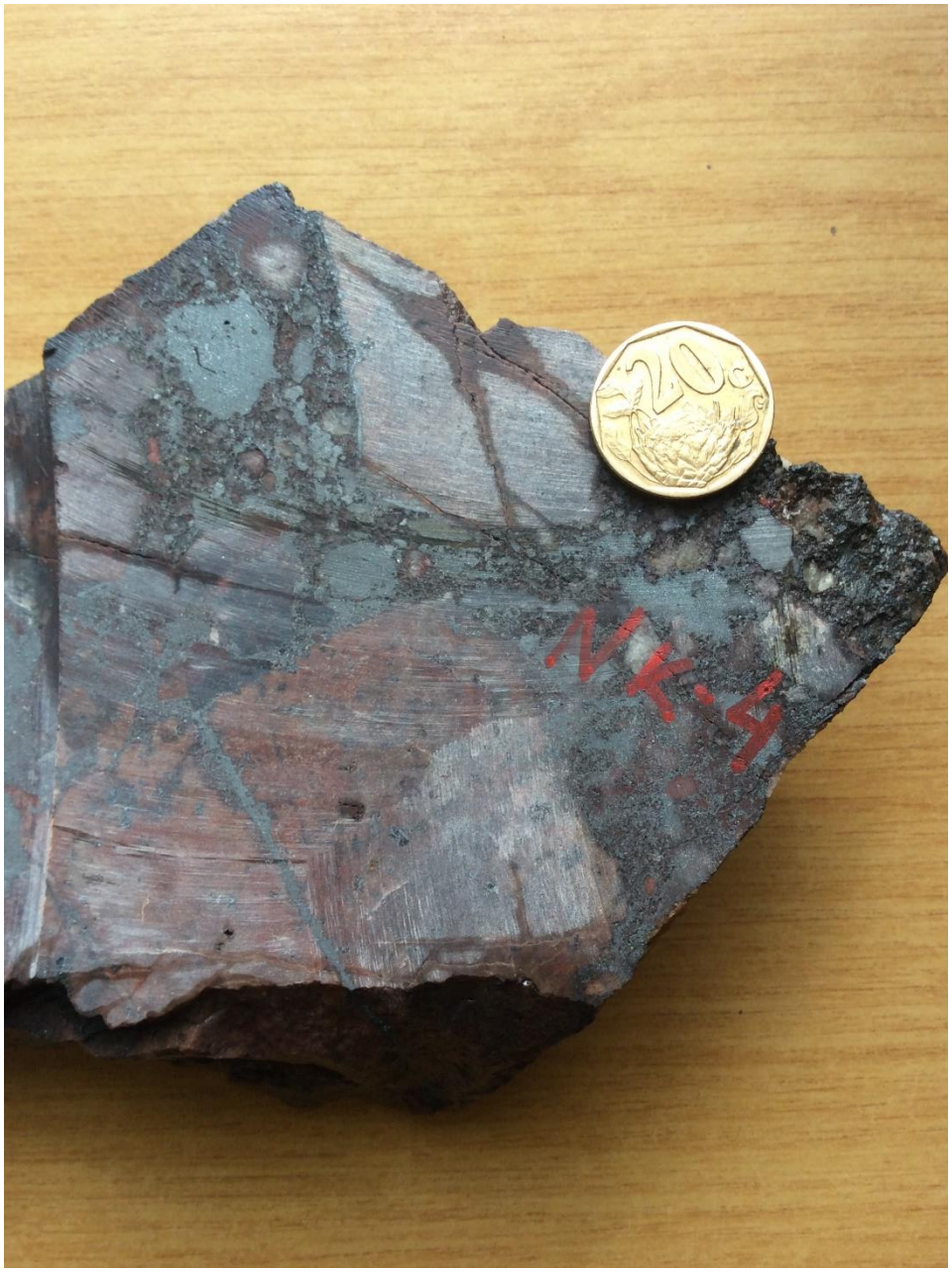

Sample	Thin-Section	Description
	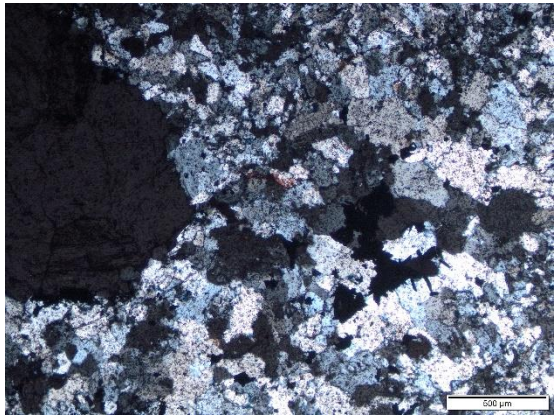	**NK4A clast-supported eruptive breccia** In the hand specimen it shows large rhyolite clasts and smaller hematite clasts surrounded by a matrix of reddish hematite, blackish specularitic hematite and fluorite. There is also magnetite. In the thin section the sample show fluorite grain surrounded by recrystallized quartz grains, that have hematite inclusions. Image is in XPL
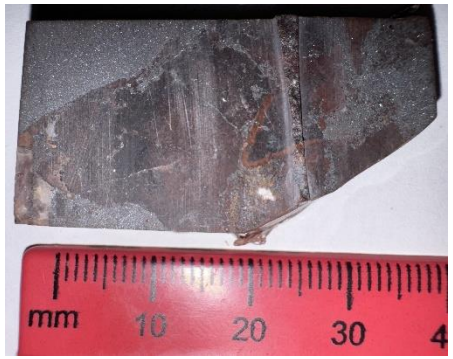	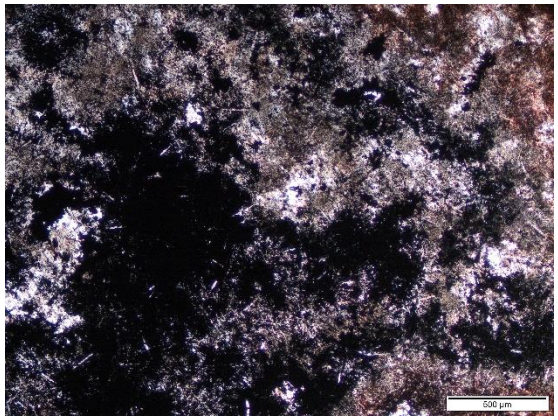	**NK4B clast-supported eruptive breccia** In the hand specimen it shows a rhyolitic clast surrounded by a matrix of dominantly greyish specularitic hematite. There is evidence of reddish hematite replacing primary magnetite. In the thin section the sample show quartz after tridymite with interstitial hematite. Image is in PPL.

	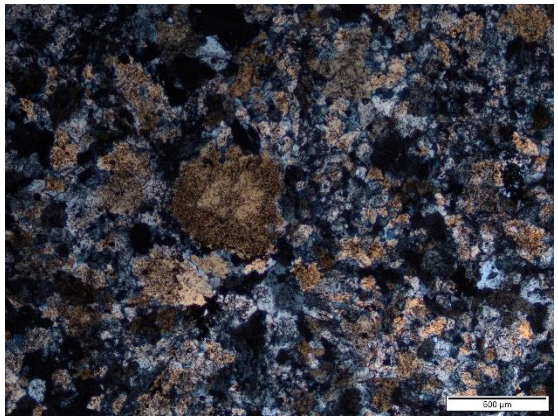	**NK4A** In the hand specimen it shows large rhyolitic clast surrounded by a matrix of blackish specularitic hematite and fluorite. There is also magnetite. In the thin section the sample shows recrystallized quartz grains with high birefringence, that have hematite inclusions. Image is in XPL
		**This is NK4B** In the hand specimen it shows rhyolitic tuff clasts surrounded by a matrix of blackish specularitic hematite. There is evidence of reddish hematite replacing magnetite. In the thin section the sample shows areas completely covered by hematite with minor silicate minerals. Image is in XPL

3.Vergenoeg Magnetite-Fluorite Unit

Sample name: VG1.

Modal Mineralogy: magnetite (56 %), fluorite (34 %), hematite (8 %) and quartz (2 %)

Sample	Thin-Section	Description
	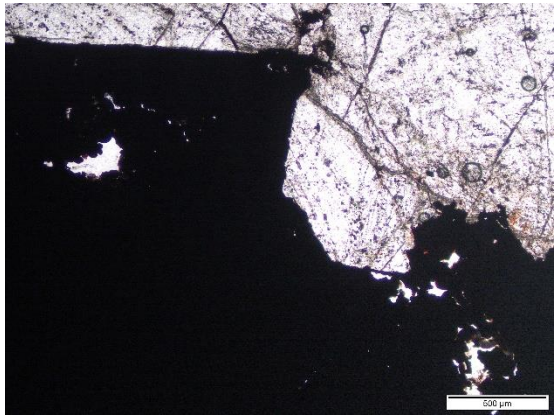	**VG1A massive fluorite-hematite-magnetite ore** In the hand specimen it shows a large fluorite grain in contact with massive magnetite that has vuggs. In the thin section the sample shows a larger fluorite grain surrounded by magnetite. Image is in XPL.
	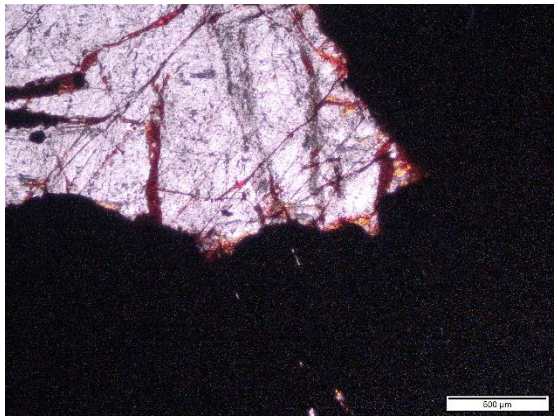	**This is VG1B** In the hand specimen it shows massive slightly vuggy hematite surrounding fine grained fluorite. There is also a reddish hematite indicative colour on the magnetite. In the thin section the sample shows a larger fluorite grain surrounded by magnetite. There are hematite veins cutting across the fluorite. Image is in XPL.

	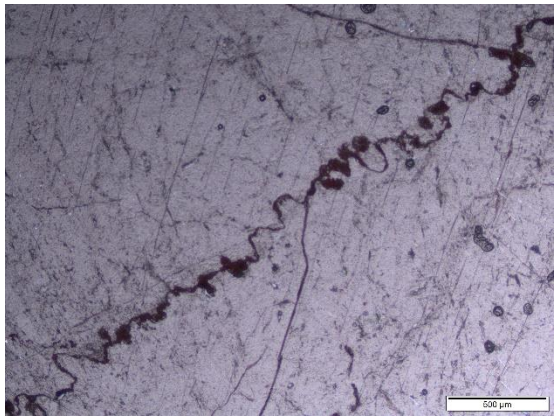	**This is VG1C** In the hand specimen it shows fluorite grains surrounded by a matrix of black magnetite. This shows a porphyritic texture. In the thin section the sample show massive fluorite with a vein of hematite cutting across it. Image is in XPL.
	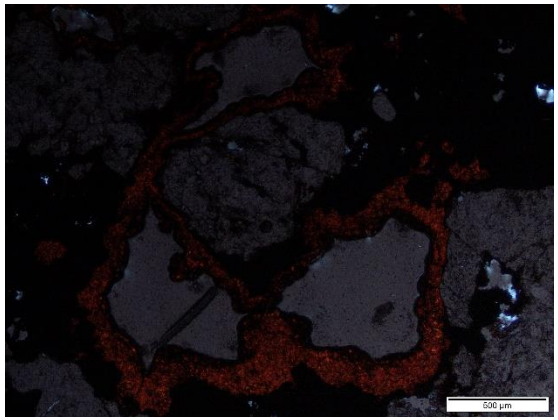	**This is VG1D** In the hand specimen it shows fluorite grains surrounded by blackish magnetite. In the thin section the sample show fluorite surrounded by magnetite that is being replaced by reddish hematite. Image in XPL

	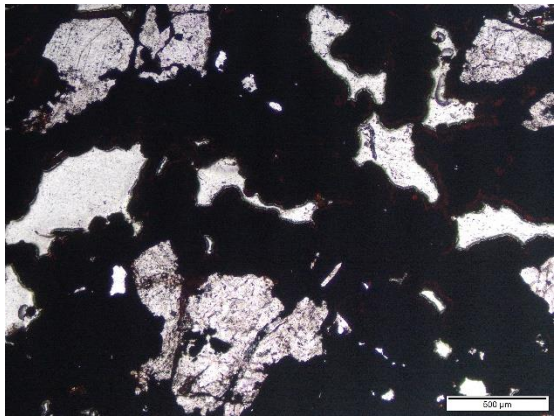	**VG1E massive fluorite ore** In the hand specimen it shows fluorite grains surrounded by blackish magnetite. In the thin section the sample show fluorite surrounded by magnetite, that is being replaced by reddish hematite. Image in PPL

Appendix B – Whole Rock Geochemical Analyses

Table B.1: Whole rock major oxide compositions (wt.%) of the studied Nokeng and Vergenoeg rocks. Analysis was conducted using X-ray fluorescence (XRF).

Sample Name	SiO_2	Al_2O_3	FeO^t	MnO	MgO	CaO	Na_2O	K_2O	TiO_2	P_2O_5	Cr_2O_3	NiO	LOI	Total
VG1A	1.91	1.07	30.2	0.11	bdl	43.2	bdl	0.01	0.05	0.06	0.02	0.01	3.38	83.3
VG1B	1.81	0.67	48.5	0.10	0.00	27.4	bdl	0.02	0.09	0.48	0.03	0.01	2.98	87.3
VG1C	1.24	0.45	29.9	0.12	bdl	45.2	bdl	0.01	0.08	0.07	0.02	bdl	2.25	82.6
VG1D	1.24	1.10	31.0	0.08	bdl	42.3	0.18	0.03	0.05	0.06	0.02	bdl	3.73	83.2
VG1E	1.83	0.65	40.1	0.10	bdl	35.9	0.57	0.07	0.06	0.10	0.03	0.01	2.63	86.5
NK1A	11.7	0.10	31.7	0.02	bdl	37.1	0.04	0.02	0.09	0.14	0.02	0.01	1.41	85.8
NK2A	33.0	2.33	29.0	0.03	0.04	21.6	bdl	0.67	0.25	0.24	0.02	bdl	1.20	91.5
NK2B	32.9	2.26	28.9	0.03	0.04	21.6	bdl	0.63	0.22	0.34	0.03	bdl	1.32	91.4
NK3A	0.36	0.17	38.5	0.07	bdl	39.4	0.40	0.04	0.03	0.22	0.02	bdl	2.85	86.3
NK3B	0.18	0.22	34.9	0.05	bdl	41.7	0.08	0.02	0.03	0.37	0.02	0.01	3.25	84.6
NK3C	0.42	0.24	33.3	0.05	bdl	43.0	1.58	0.11	0.03	0.43	0.03	bdl	3.13	86.0
NK4A	48.4	0.26	28.6	0.03	0.01	13.6	0.06	0.04	0.16	0.07	0.02	bdl	1.48	96.0
NK4B	36.7	0.64	44.9	0.05	0.03	8.57	bdl	0.08	0.17	0.07	0.02	bdl	0.85	97.0
NK4C	26.1	0.34	44.5	0.04	0.01	17.0	bdl	0.04	0.14	0.09	0.02	bdl	1.40	94.5
NK4D	57.0	0.38	28.9	0.05	0.02	6.74	bdl	0.05	0.18	0.08	0.01	bdl	2.56	99.1

Bdl : bellow detection limit

Table B.2: Whole rock trace element composition (ppm) of Nokeng and Vergenoeg rocks by ICP-MS.

Element	VG1A (Magnetite-fluorite)	NK1A (Hematite-fluorite)	NK2A (Hematite-fluorite)	NK3A (Hematite-fluorite)	NK4A (Breccia agglomerate)
Li	3.82	8.18	4.60	2.07	4.74
P	182	829	787	804	276
Sc	2.46	1.38	3.61	1.12	1.84
Ti	515	1109	2172	370	1256
V	2.21	12.4	30.6	2.40	15.6
Cr	2.96	25.8	70.0	4.81	9.92
Co	3.28	0.898	1.28	2.73	1.11
Ni	18.7	3.33	3.70	4.07	3.94
Cu	488	11.5	15.5	25.0	4.33
Zn	51.3	18.1	15.8	21.2	8.94
Ga	43.0	153	103	80.5	32.3
As	146	87.7	73.2	62.8	20.9
Rb	1.30	2.45	77.3	2.83	3.55
Sr	24.8	54.9	61.0	31.6	23.8
Y	1729	1805	641	1516	162
Zr	7.68	13.9	92.6	7.41	242
Nb	314	310	143	534	32.6
Sn	24.5	290	416	68.7	210
Sb	4.72	66.7	36.7	21.3	21.4
Cs	0.084	0.399	1.69	1.96	0.865
Ba	37.1	30.5	130	38.5	40.0
La	114	1191	684	305	348
Ce	239	1842	1059	775.6	423
Pr	33.8	185	129	99.3	34.0
Nd	145	547	383	371	83.4
Sm	37.5	83.2	60.2	76.1	11.4
Eu	1.19	5.51	2.70	1.71	2.35
Gd	41.0	64.4	40.0	57.1	10.1
Tb	6.91	7.86	5.13	8.88	1.51
Dy	51.7	49.8	29.3	62.9	10.3
Ho	12.1	11.4	5.88	14.0	2.24
Er	42.0	39.5	20.0	49.1	7.68
Tm	6.79	6.10	3.10	7.59	1.21
Yb	50.0	43.6	22.0	54.9	7.90
Lu	7.37	6.24	2.87	7.51	0.926
Hf	0.317	0.444	1.81	0.344	4.67
Ta	2.88	0.954	0.473	1.55	0.333
W	16.5	181	90.2	52.0	85.2
Tl	0.252	0.036	0.350	0.036	0.064
Pb	40.7	35.7	42.7	32.9	20.3
Th	5.77	4.45	3.93	9.10	6.15
U	21.2	11.4	14.0	36.7	5.39

Appendix C – TIMA Analysis

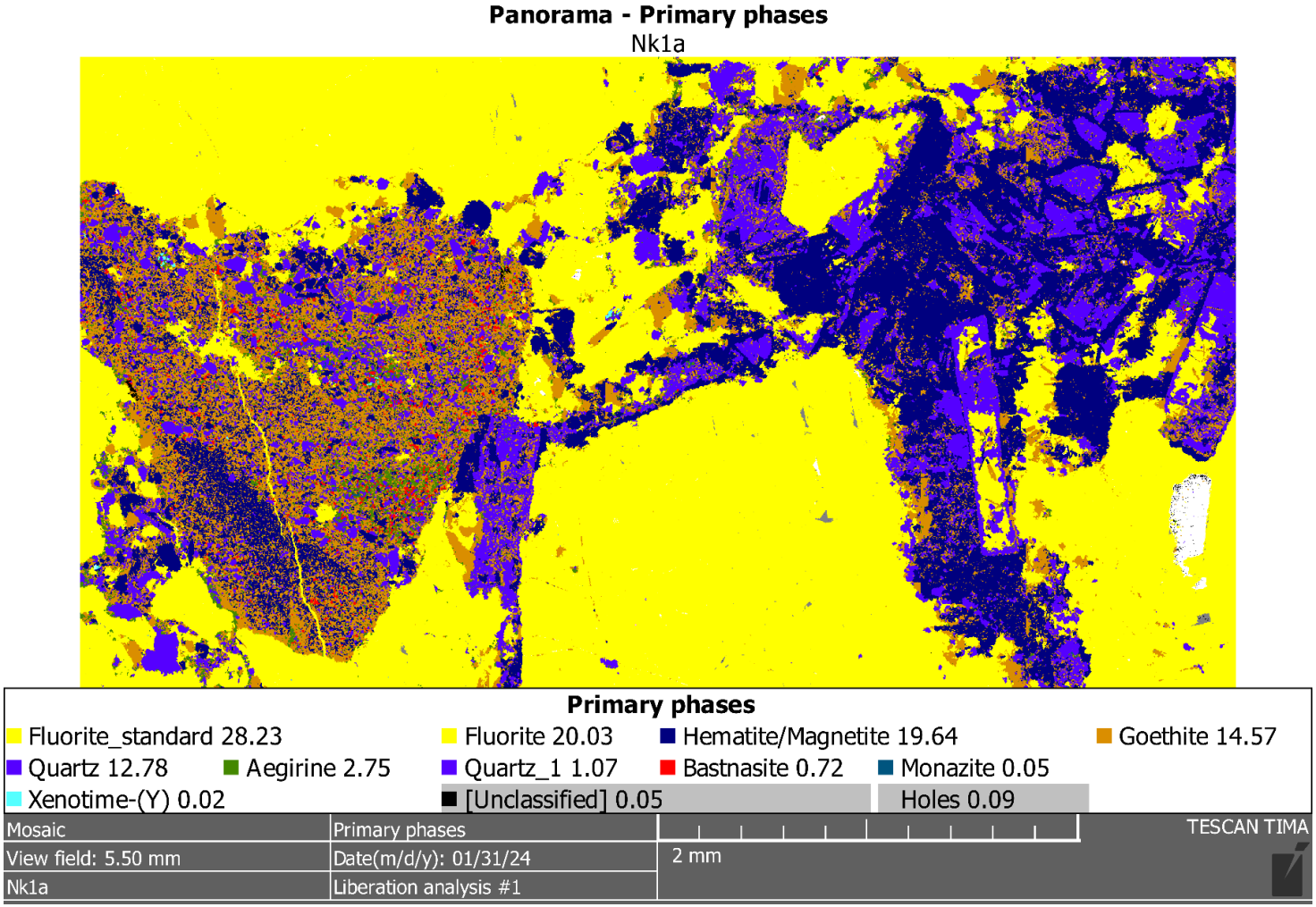

Figure C.1. Mineral map according to the TIMA liberation analysis, showing all the minerals before grouping in Section A.

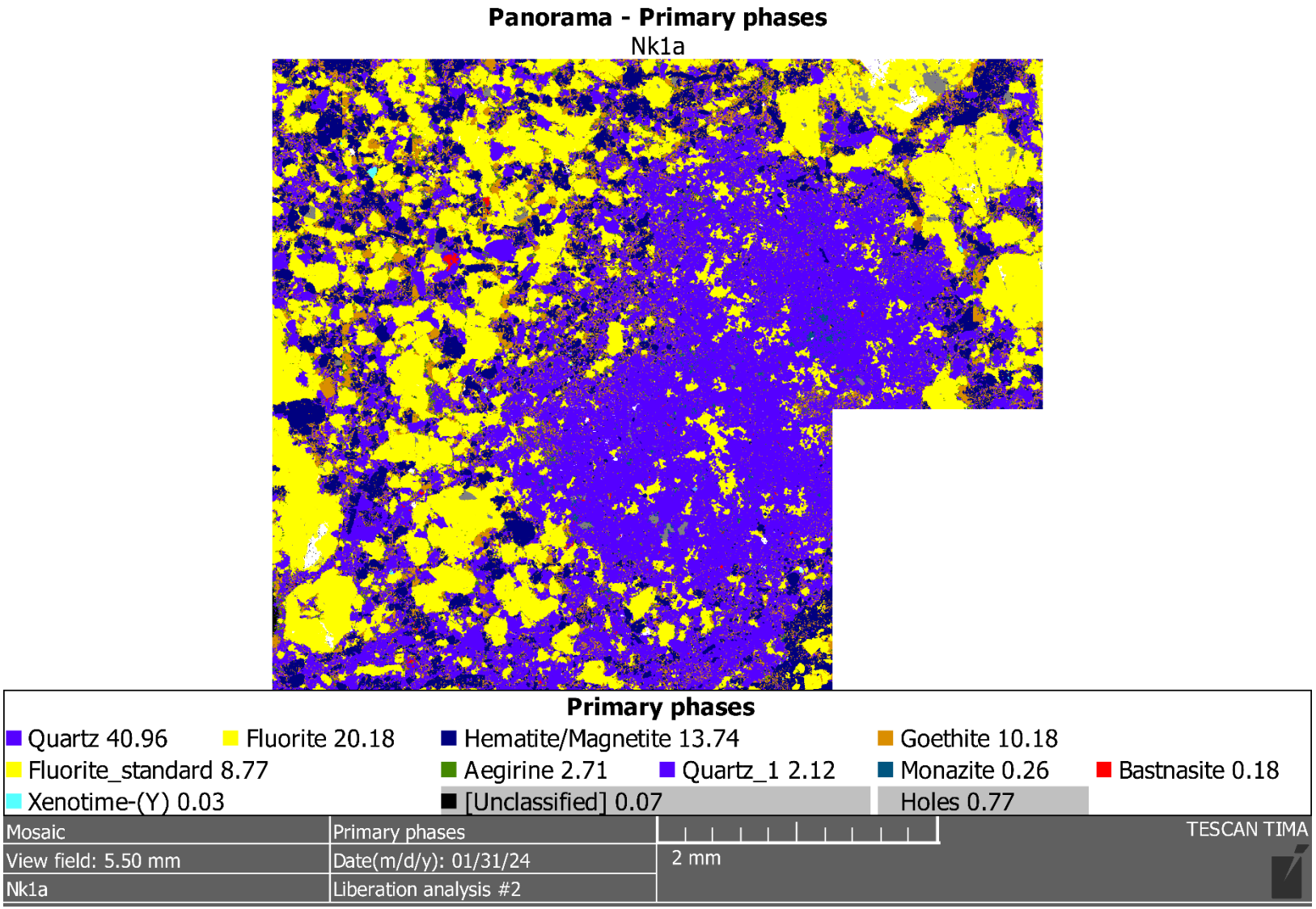

Figure C.2. Mineral map according to the TIMA liberation analysis results showing all the minerals before grouping in the Section B.

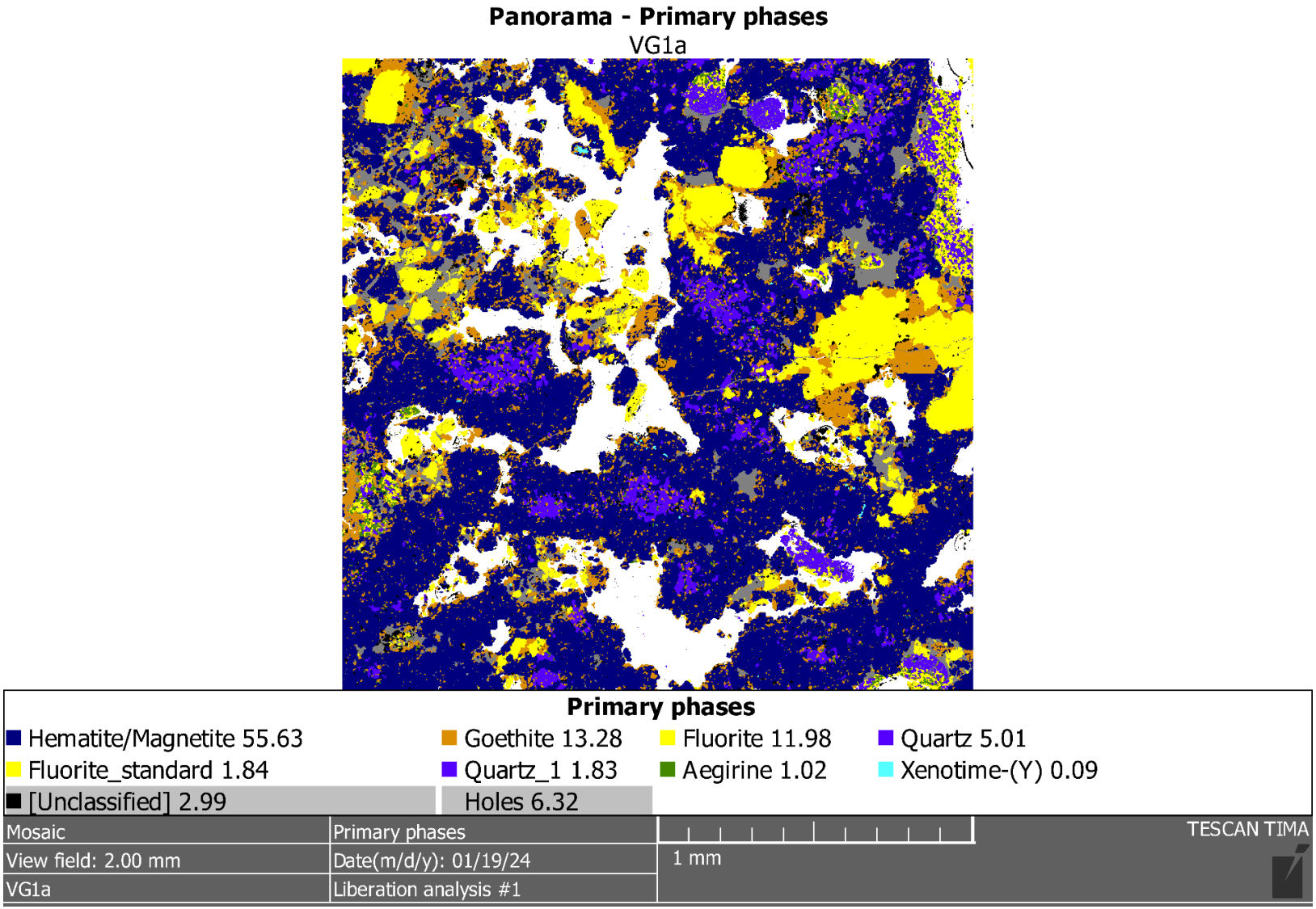

Figure C.3. Mineral map according to the TIMA liberation analysis, showing all the minerals before grouping in VG1A (1).

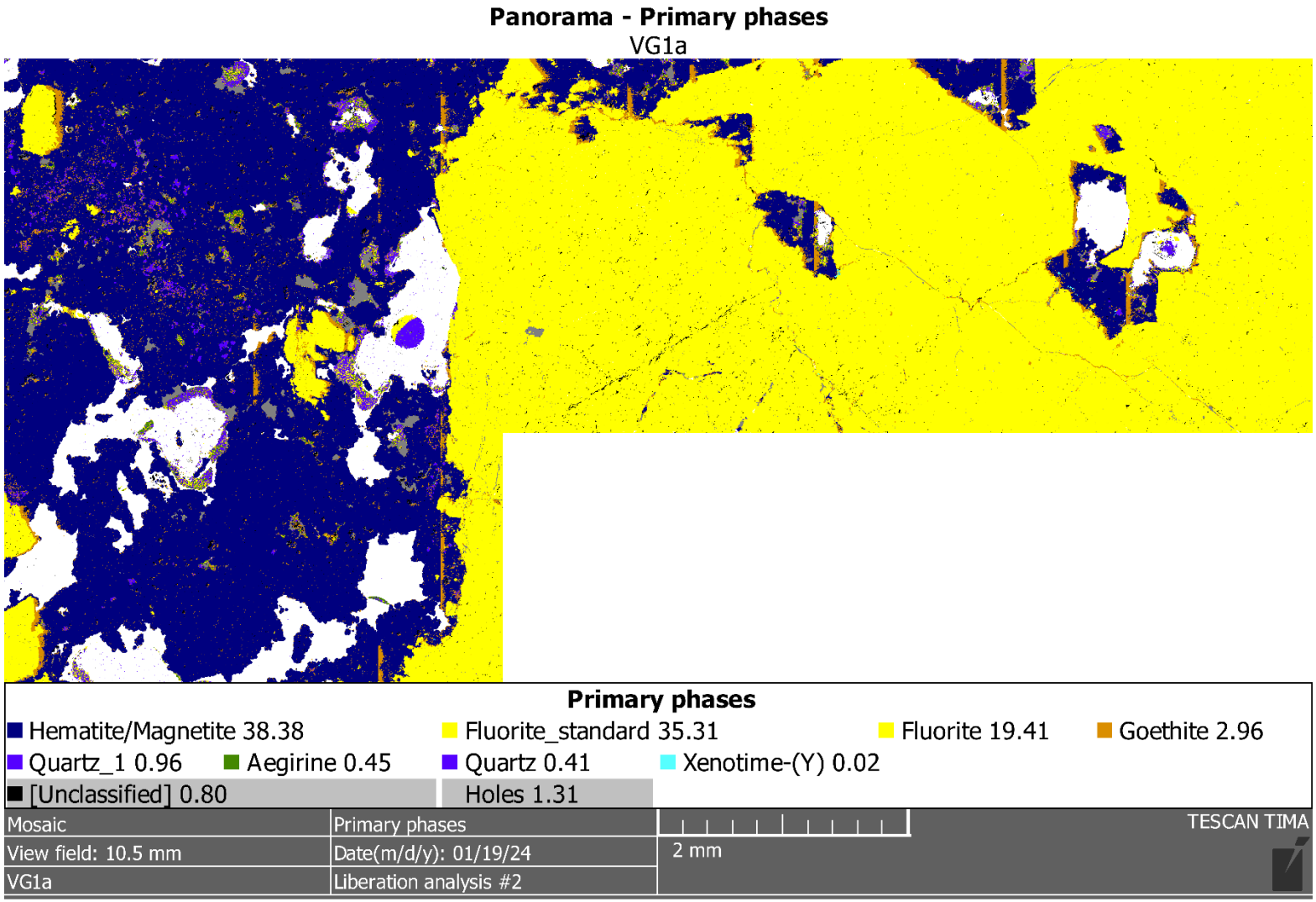

Figure C.4. Mineral map according to the TIMA liberation analysis, showing all the minerals before grouping in VG1A (2).

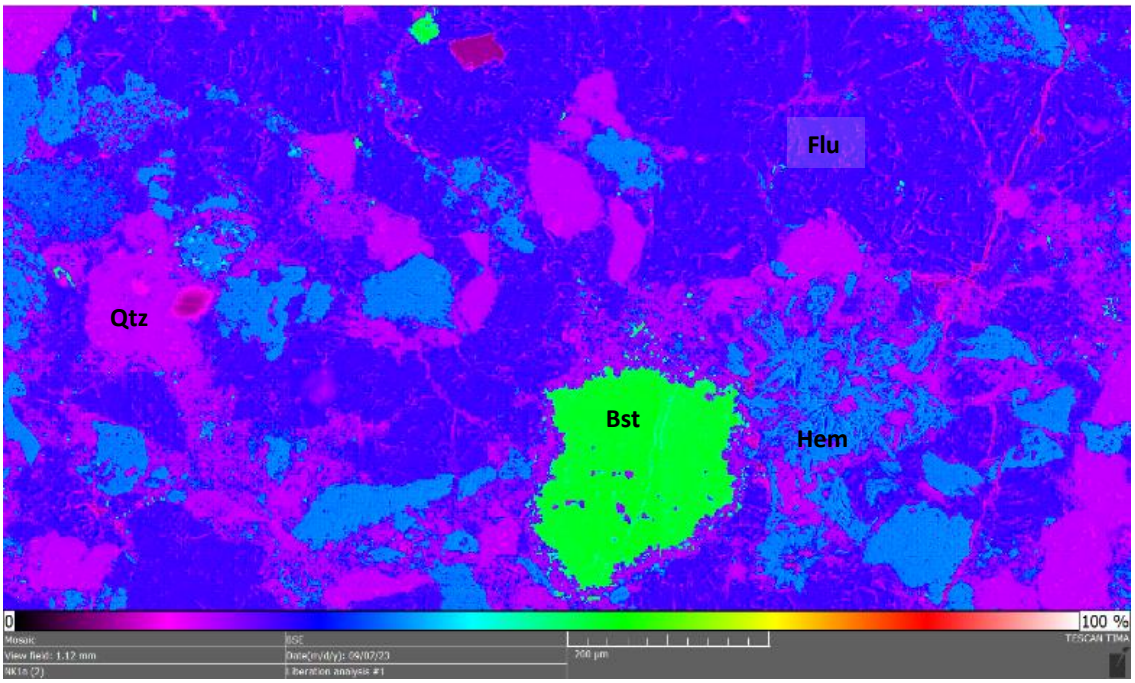

Figure C.5. Coloured BSE image showing bastnasite (bst) surrounded by quartz (qtz), hematite (hem), and fluorite (flu) in sample NK1A. Abbr.: flu-fluorite; hem-hematite; bst-bastnasite; qtz-quartz

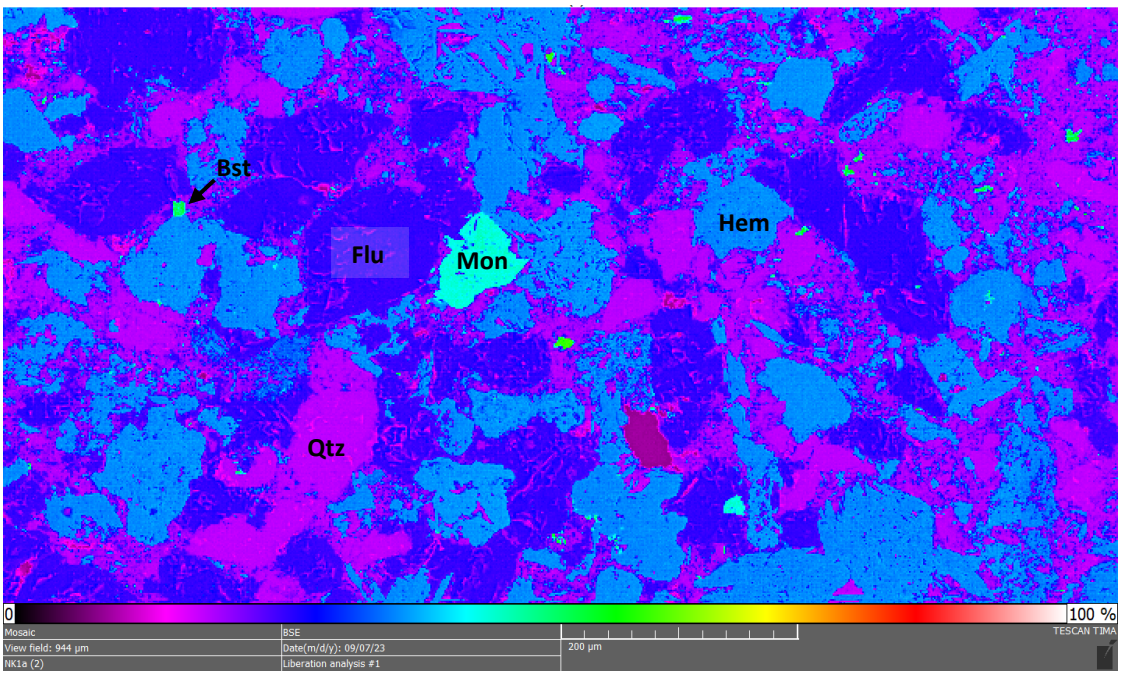

Figure C.6. Coloured BSE image showing bastnasite (bst) and monazite (mon) surrounded by quartz (qzt), hematite (hem), and fluorite (flu) in NK1A. Abbr.:flu-fluorite; hem-hematite; mon-monazite; bst-bastnasite; qtz-quartz

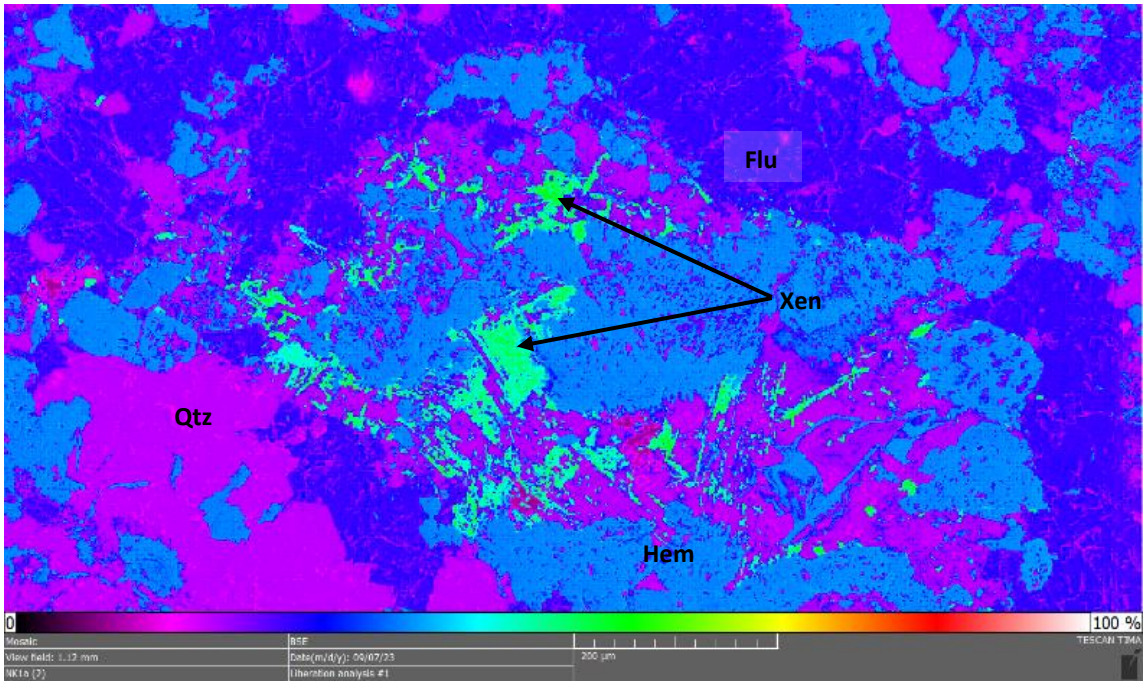

Figure C.7. Coloured BSE image showing xenotime (xen) surrounded by quartz (qzt), hematite (hem), and fluorite (flu) in NK1A. Abbr.: flu-fluorite; hem-hematite; xen-xenotime; qtz-quartz

Tabe C.1: Mineral locking of bastnasite (mass) according to TIMA in various primary phases. The table also shows the mass of the REE that occurs on a free surface, or in primary phases not listed.

Mass of Bastnasite				
Primary phases / Dataset	**VG1A - Liberation analysis #1**	**VG1A - Liberation analysis #2**	**NK1A - Liberation analysis #1**	**NK1A - Liberation analysis #2**
Aegirine	0.00	0.00	0.10	0.01
Goethite	0.00	0.00	0.37	0.03
Hematite/Magnetite	0.00	0.00	0.18	0.03
Quartz	0.00	0.00	0.20	0.11
Fluorite_standard	0.00	0.00	0.06	0.02
Fluorite	0.00	0.00	0.12	0.06
Free surface	**0.00**	**0.00**	**0.03**	**0.00**
The rest	**0.00**	**0.00**	**0.01**	**0.01**
Total	**0.01**	**0.00**	**1.07**	**0.28**

Tabe C.2: Mineral locking of monazite (mass) according to TIMA in various primary phases. The table also shows the mass of the REE that occurs on a free surface, or in primary phases not listed.

Mass of Monazite				
Primary phases / Dataset	**VG1A - Liberation analysis #1**	**VG1A - Liberation analysis #2**	**NK1A - Liberation analysis #1**	**NK1A - Liberation analysis #2**
Goethite	0.00	0.00	0.02	0.02
Hematite/Magnetite	0.00	0.00	0.01	0.01
Quartz	0.00	0.00	0.02	0.32
Fluorite	0.00	0.00	0.01	0.05
Quartz_1	0.00	0.00	0.00	0.01
Free surface	**0.00**	**0.00**	**0.00**	**0.01**
The rest	**0.00**	**0.00**	**0.01**	**0.01**
Total	**0.01**	**0.00**	**0.08**	**0.44**

Tabe C.3: Mineral locking of bastnasite (mass) according to TIMA in various primary phases. The table also shows the mass of the REE that occurs on a free surface, or in primary phases not listed.

Mass of Xenotime-(Y)				
Primary phases / Dataset	**VG1A - Liberation analysis #1**	**VG1A - Liberation analysis #2**	**NK1A - Liberation analysis #1**	**NK1A - Liberation analysis #2**
Goethite	0.03	0.00	0.01	0.01
Hematite/Magnetite	0.05	0.01	0.00	0.01
Quartz	0.00	0.00	0.00	0.01
Fluorite	0.01	0.01	0.01	0.01
The rest	**0.00**	**0.01**	**0.01**	**0.01**
Total	**0.10**	**0.02**	**0.03**	**0.05**

Tabe C.4: Mineral association of bastnasite, monazite and xenotime within the Vergenoeg and Plattekop deposits. This data is reported by mass and is sourced from the TIMA liberation analysis 1 and 2 performed on samples VG1A and NK1A.

Mass of phase			
Dataset / Primary phases	Bastnasite	Monazite	Xenotime-(Y)
VG1A - Liberation analysis #1			
Goethite	0.00	0.00	0.04
Hematite/Magnetite	0.00	0.01	0.06
Total	0.00	0.01	0.10
VG1A - Liberation analysis #2			
Goethite	0.00	0.00	0.01
Hematite/Magnetite	0.00	0.00	0.01
Total	0.00	0.00	0.02
NK1A - Liberation analysis #1			
Bastnasite		0.01	0.00
Monazite	0.01		0.00
di	0.24	0.02	0.01
Goethite	0.51	0.02	0.01
Hematite/Magnetite	0.12	0.01	0.00
Quartz	0.16	0.02	0.01
Total	1.04	0.08	0.03
NK1A - Liberation analysis #2			
Bastnasite		0.01	0.00
Monazite	0.01		0.00
Aegirine	0.03	0.02	0.01
Goethite	0.03	0.02	0.02
Hematite/Magnetite	0.01	0.01	0.01
Quartz	0.17	0.32	0.01
Fluorite	0.01	0.01	0.01
Quartz_1	0.03	0.04	0.00
Total	0.29	0.43	0.06

Table C.5: Total REE + Y concentrations within the Vergenoeg units (Graupner et al., 2015).

Samples	REE + Y (ppm)
SA09-120 (‘Metspar’ plugs)	2 966
SA09-121 (‘Metspar’ plugs)	2237
SA09-106 (hematite-fluorite gossan)	2 475
SA09-111 (siderite lenses)	925
SA09-118 (siderite lenses)	86.5
Ver12-3b (Magnetite-fluorite unit)	4 171
SA09-113 (magnetite-fayalite unit)	393
SA09-114 (magnetite-fayalite unit)	457
SA09-123 (fayalite unit)	1 911
SA09-125 (fayalite unit)	1 189